SKB

Probabilistic model for the pitting of copper canisters during the early aerobic, unsaturated transient period of the repository evolution

Scott Briggs

Christina Lilja

Fraser King

SVENSK KÄRNBRÄNSLEHANTERING

Probabilistic model for the pitting of copper canisters during the early aerobic, unsaturated transient period of the repository evolution

Scott Briggs, Nuclear Waste Management Organization

Christina Lilja, Svensk Kärnbränslehantering AB

Fraser King, Integrity Corrosion Consulting Ltd

Summary

A probabilistic model is described for assessing the duration and extent of localised corrosion of copper canisters under aerobic, unsaturated conditions. The model is referred to as the Probabilistic Unsaturated Pitting (PUP) model. The underlying conceptual model is based on the Evans droplet mechanism for atmospheric corrosion, in which non-uniform wetting of the surface occurs as a result of the deliquescence of surface salts or other contaminants. A natural consequence of droplet formation is the spatial separation of the anodic and cathodic reactions, resulting in the possible initiation and propagation of localised corrosion. Pit stifling may occur as a result of a number of mechanisms related either to the evolution of the near-field environment or associated with the pitting process itself. The limited depth of localised corrosion observed under relevant conditions in large-scale *in situ* tests indicates that pits tend to stifle readily under repository conditions.

The structure of the PUP model is based on three modules; the control, environment, and pit growth modules. In addition to initialising the code by selecting a unique temperature and relative humidity (RH) profile for each realisation (or run), the control module controls execution of the code by determining whether the surface is non-uniformly wetted or not and by incrementing the time. If the surface is wet then pit initiation is deemed to have occurred, following which the environment module is used to assess whether an environmentally related stifling mechanism is operative. If the pit has not stifled, then the pit growth module is used to determine whether stifling occurs for one of a number of additional stifling mechanisms not related to the environmental conditions. If pit stifling still does not occur then the increment of pit growth is calculated and the code returns to the control module and the time is incremented. The entire process is then repeated until such time that the canister wall is penetrated or a user-specified maximum time is reached.

Monte Carlo methods are used to account for variability and uncertainty in the system. These sources of variability and uncertainty include the variability in environmental conditions, such as the temperature and RH at the canister surface, and the uncertainty in corrosion mechanisms, such as the threshold O_2 concentration below which a pit stifles. Probability distribution functions are used to describe a number of parameters, with a specific value sampled for each realisation. The basic output of a single realisation is the pit age and depth for a canister in a deposition hole. By performing multiple realisations (typically, up to one million), the effects of uncertainty and variability of the entire system can be assessed.

Results are presented of preliminary simulations of the evolution of the near-field conditions for the Forsmark repository and the resulting distributions of pit ages and pit depths. Only environmental-related stifling mechanisms associated with the time dependent O_2 concentration and RH are considered here. Estimates of pit depths are based on two empirical pit growth expressions. It is found that the evolving near-field conditions in combination with the various environmental stifling mechanisms limit pit growth to a maximum of a few months in duration and < 200 µm in depth. Of the environmental stifling mechanisms considered, the consumption of the initially trapped O_2 and the drying of the surface during the thermal transient are most important.

Further development of the code and the implications of the results of these preliminary simulations on the need for additional supporting experimental information are also discussed.

Contents

1   Introduction

Evidence from both laboratory experiments and large-scale *in situ* tests indicate that copper canisters should undergo uniform, as opposed to localised, corrosion under repository conditions (King and Lilja 2014; King et al. 2010; SKB 2010, 2019, 2022a). However, the same experiments indicate that there will a certain degree of non-uniform corrosion or surface roughening. Localised corrosion, either in the form of discrete pitting or surface roughening, is most likely during the initial aerobic period because the presence of O_2 provides an opportunity for the spatial separation of anodic and cathodic reactions. In contrast, localised corrosion is unlikely if the corrosion rate is limited by the transport of reactants, as it is under the long-term anaerobic conditions in the repository due to the supply of sulfide (King et al. 2017). Under transport-limited conditions, the entire surface of the canister is, by definition, uniformly accessible and the spatial separation of anodic and cathodic reactions is not possible. Furthermore, even if localised corrosion did initiate, there is no driving force for the transport of sulfide ahead of the uniformly corroding front as the interfacial sulfide concentration is zero due to the rapid consumption of reactants under transport-limited conditions.

The nature of the near-surface environment during the initial thermal-saturation-redox transient will depend on the relative rates of buffer saturation and of O_2 consumption. The entire evolution of the repository environment can be described by four conditions (Figure 1-1(a)):
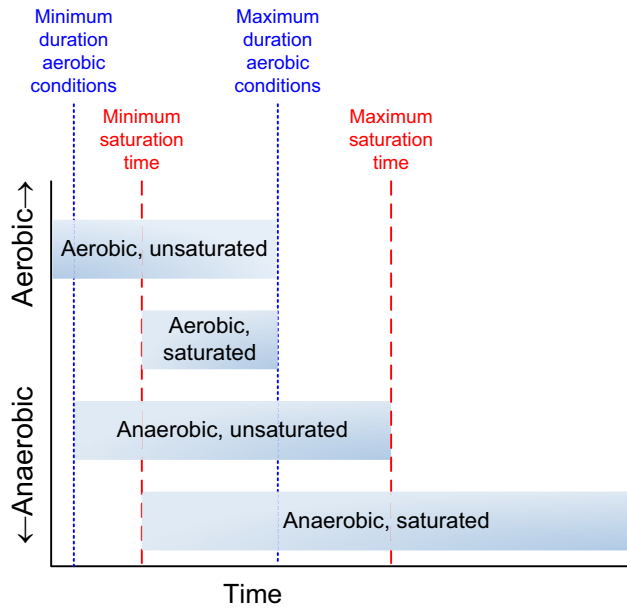
- Aerobic, unsaturated conditions.
- Aerobic, saturated conditions.
- Anaerobic, unsaturated conditions.
- Anaerobic, saturated conditions.

If the rate of O_2 consumption is fast compared to the rate of saturation, then aerobic, saturated conditions may never exist in the repository (Figure 1-1(b)). Instead, it is more likely that aerobic conditions will correspond to the unsaturated phase, prior to saturation of the near field by incoming groundwater.

Although the occurrence of aerobic, saturated conditions in the repository is considered unlikely, Briggs et al. (2020, 2021) investigated the likelihood and severity of pitting of copper under these conditions. Pit initiation was the consequence of the localised breakdown of a passive surface film, the formation of which was dependent on the buffer pore water composition (specifically the $[Cl^-]$, $[SO_4^{2-}]$, $[HCO_3^-]$, and pH) and the canister temperature. Film breakdown was conditional on the value of the corrosion potential E_{CORR} exceeding the film breakdown potential E_B, with E_{CORR} dependent on the time-dependent $[O_2]$ in the near field. Pit propagation was assumed to continue until E_{CORR} dropped below the repassivation potential E_{RP} as a result of O_2 consumption. The extent of pit propagation was determined from the duration of pitting using an empirical pit growth expression. An important aspect of the probabilistic model was the treatment of variability and uncertainty through the use of Monte Carlo methods and probability distributions for each of the input parameters.

In this report, the probabilistic approach to the assessment of the localised corrosion of copper canisters is also applied to the case of aerobic, unsaturated conditions. The conceptual pitting model, described in Chapter 2, is quite different from that for saturated conditions. Pit initiation is the consequence of the spatial separation of anodic and cathodic sites based on the Evans droplet model for atmospheric corrosion (Section 2.2), rather than the breakdown of a passive film. Pit propagation continues until growth is stifled by one or more stifling mechanisms. These mechanisms are divided into environmentally related stifling processes, such as the exhaustion of O_2 or an increase in relative humidity, and non-environmental mechanism, such as the coalescence of adjacent droplets or excessive iR drop associated with the anode or cathode (Section 2.3). The implementation of the code is described in Chapter 3. As with the saturated pitting model (Briggs et al. 2020, 2021), the unsaturated model is based on a series of flow charts that control execution of the code (Section 3.1). The input data are presented in Section 3.2, along with a discussion of the various sources of variability and uncertainty. At this stage in the model development, the focus has been on the assessment of the variability of the environmental conditions in the repository and under what conditions these may lead to pit stifling due to one or more of the environmentally related stifling mechanisms (Chapter 4). The implications of the results of these analyses for future experimental studies and further development of the model are discussed in Chapter 5.

For convenience, the model is referred to as the **P**robabilistic **U**nsaturated **P**itting (PUP) model.

(a) Unsaturated and saturated aerobic conditions
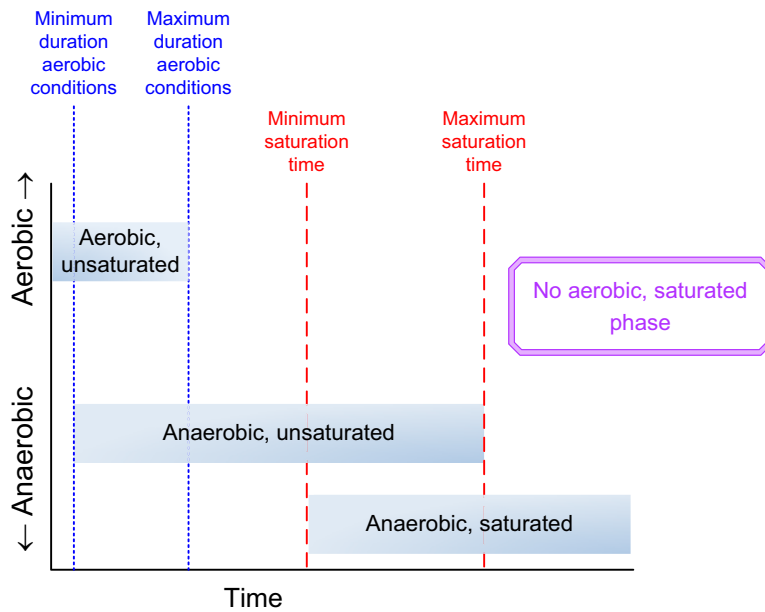
(b) No aerobic, saturated condition

Figure 1-1. *Schematic illustrations of the evolution of the near-field saturation and redox conditions.*

2 Conceptual model for the pitting of copper canisters under unsaturated conditions

2.1 Background

Although localised corrosion is possible under aerobic, unsaturated conditions, the evidence from large-scale *in situ* experiments is that the extent of propagation is limited. Table 2-1 summarises the environmental conditions and measured pit depths from a number of *in situ* experiments. In all cases, the copper coupons and/or canister were exposed to environmental conditions representative of the early thermal-saturation-redox transient expected in the repository. In particular, by the end of the tests, the buffer material was saturated (or close to saturated in the case of FEBEX) and all of the initially trapped O_2 had been consumed (although there was leakage through the plug in FEBEX). Thus, the corrosion damage observed can be considered to be representative of that which might be expected for a copper canister in the repository during the early thermal-saturation-redox transient.

As shown by the measurements in Table 2-1, the extent of pitting under unsaturated conditions is limited. The maximum pit depth reported is 100 μm observed on an electrolytic tough pitch Cu coupon from the FEBEX experiment (Figure 2-1). In other experiments, however, the observed maximum pit depths were significantly smaller and in many cases were no greater than the depth of surface features on similarly prepared, but unexposed, copper surfaces (Table 2-1).

In order to put these observed pit depths into context, consider the total amount of O_2 available to support corrosion in these tests. Each of these large-scale *in situ* experiments had an initial O_2 inventory typical of that for the repository, of the order of 1–10 mol O_2 per m^2 of canister surface. (In a number of the experiments, additional atmospheric O_2 may have entered the buffer during the test because of leaky seals and plugs). Assuming 100 % of this O_2 leads to corrosion distributed uniformly over the surface of the canister, the resulting depth of attack would be 30–300 μm. Thus, the observed pit depths are no greater than the expected average depth of corrosion estimated on the basis of a mass-balance calculation. Although a fraction of the initially trapped O_2 will have been consumed by processes other than canister (or coupon) corrosion, the relatively shallow depth of pits compared with the amount of available O_2 suggests that the tendency for localised corrosion under aerobic, unsaturated conditions is limited.

As noted in Chapter 1, a probabilistic model for pitting under aerobic, saturated conditions has been previously developed (Briggs et al. 2020, 2021). It is useful to compare and contrast the prerequisite conditions for pitting under saturated and unsaturated conditions, as well as the factors that determine pit initiation, growth, and stifling (Table 2-2). Whereas passivation of the canister surface is a prerequisite for pitting under saturated conditions, the only prerequisite for unsaturated buffer is that the canister surface should be non-uniformly wetted. Thus, whereas only a fraction of canisters will be passive, approximately 10 % based on the analysis of Briggs et al. (2020, 2021), it is likely that the majority will meet the requirement that the surface is non-uniformly wetted at some stage during the thermal-saturation-redox transient.

Even if the surface is passive, however, pit initiation in saturated buffer further requires that the E_{CORR} is sufficiently positive that it results in localised film breakdown. In contrast, pit initiation is considered to be inevitable under unsaturated conditions if the surface is non-uniformly wetted due to the geometry of the droplets, as discussed in more detail below. Propagation will continue in both cases until the pit stifles. Under saturated conditions, stifling is defined by the electrochemical condition that $E_{CORR} \leq E_{RP}$. Under unsaturated conditions, it is apparent from the limited depth of pits observed in large-scale *in situ* tests (Table 2-1) that pits also readily stifle and the conceptual model on which the PUP model is based includes a number of possible stifling mechanisms related both to the evolution of the environment and to the characteristics of pit propagation.

Table 2-1. Summary of pit depths observed in various large-scale in situ experiments.

Experiment	Maximum temperature (°C)	Experiment duration (years)	Estimated saturation time (years)	Experiment aerobic period (years)	Pit depths (µm)	Depth of surface features on unexposed material (µm)	Reference
FEBEX	100	18	Years	Few years, but leakage through plug	22–100	Unknown	Giroud 2014, Wersin and Kober 2017
Prototype	90	7.5	Few years	Few years	0.5–6.9	0–3	Taxén 2013, Taxén et al. 2012
LOT/A3	30 55 65	20	2–5	< 1	< 16, < 39 < 10, < 10 < 25	< 28	Johansson et al. 2020
LOT/S2	30 55 55	20	2–5	< 1	< 20, < 39 < 57, < 10 < 13	< 28	Johansson et al. 2020
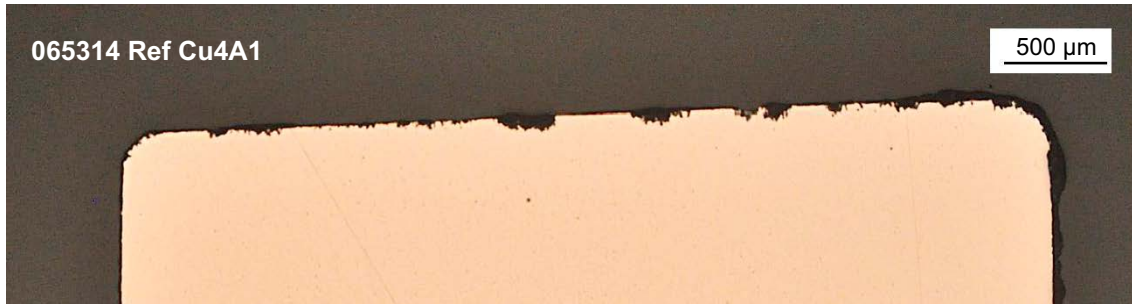
Figure 2-1. *Cross-section through copper sample 4A1 after 18 years exposure to evolving thermal-saturation-redox conditions in the FEBEX experiment (Wersin and Kober 2017).*

Table 2-2. Comparison of the prerequisite conditions for pitting under saturated and unsaturated conditions and factors determining pit initiation, growth, and stifling.

|	Saturated conditions	Unsaturated condition
Prerequisite condition	Canister surface is in passive condition (low [Cl$^-$], low temperature, high pH, high [HCO$_3^-$])	Non-uniform wetting of the canister surface
Initiation (birth)	Localised breakdown of passive film ($E_{CORR} \geq E_B$)	Spatial separation of anodic and cathodic sites due to droplet geometry
Propagation (growth)	Propagation provided $E_{CORR} > E_{RP}$	May be anodically or cathodically controlled
Stifling (death)	Repassivation of pit if $E_{CORR} \leq E_{RP}$	Various stifling mechanisms

2.2 Evans droplet model

The underlying conceptual model for the localised corrosion of copper canisters in unsaturated buffer material is based on the Evans droplet model for atmospheric corrosion (Evans 1925). In the conceptual model, droplet formation is assumed to be the result of the deliquescence of a hygroscopic surface deposit, such as a salt crystal or clay particle. Deliquescence is the process of the absorption of moisture from the atmosphere and occurs at a relative humidity (the deliquescence relative humidity DRH) that can be predicted thermodynamically. At the DRH, the activity of water in the resulting salt solution is equal to that in the atmosphere. The reverse process, efflorescence, occurs when the droplet dries out. Since efflorescence depends on the nucleation of crystals it tends to occur at a relative humidity (the efflorescence relative humidity ERH) that is higher than the DRH, resulting in hysteresis between the wetting and drying behaviour of the surface. In unsaturated soils, the canister surface may also be in contact with wet clay particles or dry air pockets at various stages during the evolution of the near-field environment. For the current conceptual model, it is assumed that non-uniform wetting occurs due to the deliquescence of surface salt contaminants.

Deliquescence of a salt particle or other type of surface contaminant leads to non-uniform wetting and the formation of a droplet of electrolyte (Figure 2-2(a)). Spatial separation of the anodic and cathodic reactions is a consequence of the higher rate of transport of atmospheric O$_2$ to the edge of the droplet, which in turn is a natural consequence of the droplet shape. For small droplets, however, O$_2$ depletion in the centre of the droplet may not occur so that spatial separation of anodic and cathodic reactions becomes less likely (Cole et al. 2011, Muster et al. 2011). You et al. (2023) have also considered the spatial separation of anodic and cathodic reactions on the surface of copper under an Evans droplet. For a droplet radius of 1 mm, the mechanistically based numerical model predicted relatively little spatial separation of anodic and cathodic reactions, with O$_2$ reduction predicted to occur across the entire droplet radius.

Subsequent development of the original droplet model takes into account a process referred to as secondary spreading, in which a thin water layer forms around the central droplet (Figure 2-2(b)) (Chen et al. 2005a,b; Cole et al. 2008, 2010; Schindelholz et al. 2018) or satellite microdroplets

form connected by a thin water layer to the central droplet (Zhang et al. 2005, Tsuru et al. 2004). The increase in pH in the region of secondary spreading due to the reduction of O_2 to OH^- ion causes the activation of the dissolution of copper as dissolved copper oxy(hydroxy) anions, such as CuO_2^{2-} (Schindelholz et al. 2018). As a consequence, the damage profile spreads from the centre of the droplet towards the periphery resulting in spreading of the corrosion damage across the surface rather than depth-wise penetration (Figure 2-2(c)).

There is also a significant effect of atmospheric CO_2 on the extent of secondary spreading and, hence, on the corrosion damage profile. Chen et al. (2005a) studied the extent of secondary spreading under both nominal atmospheric conditions (350 vppm CO_2) and low CO_2 (< 5 vppm) conditions. Absorption of CO_2 from the atmosphere reduces the extent of secondary spreading by reducing the pH in the cathodic region which, in turn, leads to an increase in surface tension (Chen et al. 2005a,b). With a smaller region of secondary spreading, the corrosion damage will tend to be more focussed within the central droplet. Such effects could be exacerbated in compacted bentonite as measurements of pore-gas composition show elevated CO_2 concentrations. For example, Birgersson and Goudarzi (2018) report approximately 1 vol.% (10 000 vppm) CO_2 in isothermal and thermal gradient experiments designed to study the consumption of O_2 in compacted buffer. Similar concentrations have been reported from full-scale *in situ* tests; Tomonaga et al. (2019) report up to 1 500 vppm in the FE-G experiment at Mont Terri in Opalinus clay host rock and up to 10–20 000 vppm has been found in the Engineered Barrier Behaviour in ONKALO® (EBBO) experiment (unpublished data).
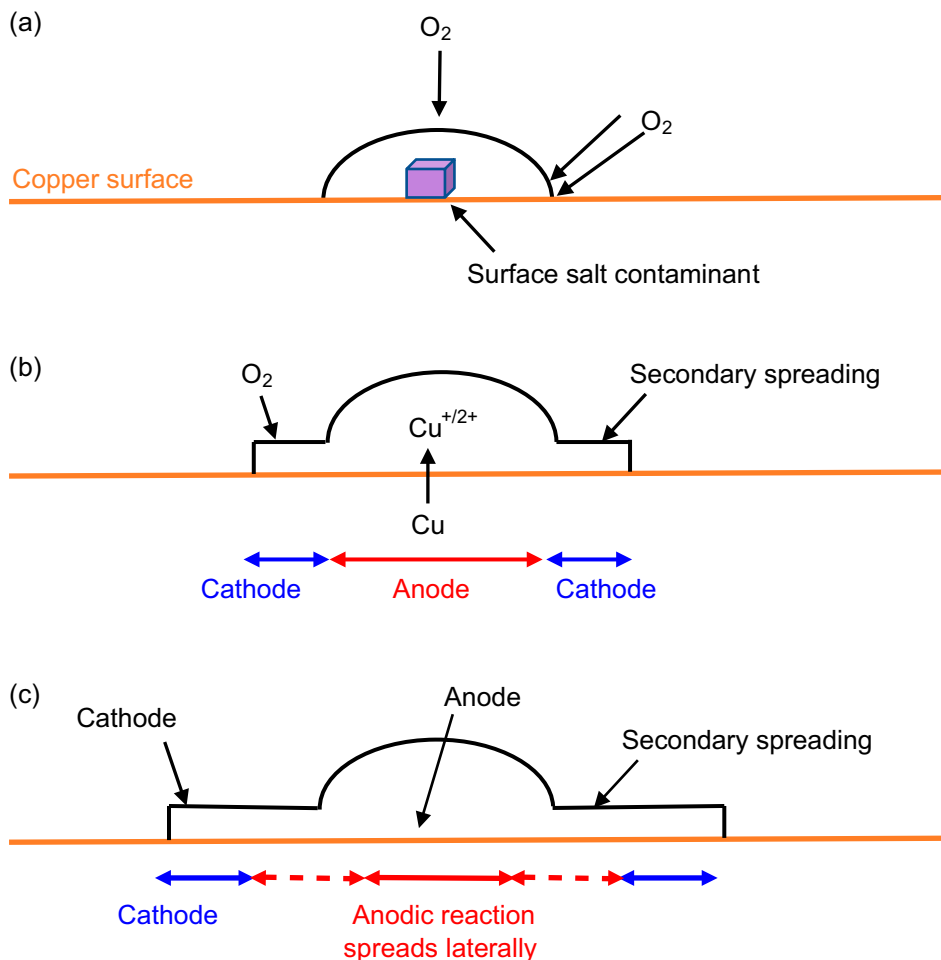
Figure 2-2. *Schematic representations of the Evans droplet mechanism for atmospheric corrosion. (a) Formation of initial droplet due to deliquescence of surface salt contaminant, with enhanced supply of O_2 to the periphery as a result of the shape of the droplet, (b) secondary spreading leading to a well-defined cathode around the periphery supporting anodic dissolution in the centre of the droplet, (c) lateral spreading of the anodic region as copper dissolution is promoted by the alkaline pH generated by O_2 reduction around the periphery.*

2.3   Application of Evans droplet model to pitting of copper canisters

The Evans droplet mechanism for atmospheric corrosion forms the basis for the pitting model for copper canisters under unsaturated, aerobic conditions. Here, the conceptual model is described in terms of the prerequisite conditions for localised corrosion and of the three stages of pitting (initiation, propagation, and stifling).

2.3.1   Prerequisite conditions

As noted in Table 2-2, the only prerequisite condition for localised corrosion under unsaturated conditions is that the surface is non-uniformly wetted. Non-uniform wetting under unsaturated conditions is assumed to be the consequence of the condensation of H_2O vapour due to one or both of the following conditions:

- Deliquescence of surface contaminants, such as salt crystals, areas of grease or organic matter, and montmorillonite particles.

- Capillary condensation in pores on the surface, such as may be present in porous oxides or surface asperities from canister fabrication.

Since the canister will be primarily exposed to atmospheric conditions in environmentally controlled buildings or transportation casks prior to disposal, it is assumed that the canister is not subject to direct deposition of moisture from the atmosphere (e.g., from precipitation or exposure to water droplets (clouds, mists)). Furthermore, the large-scale non-uniform wetting of the canister surface as might occur due to asymmetric wetting of the buffer is not considered to result in the small-scale droplet formation of interest here.

As described in Section 3.1.1, these wetting processes are combined and are treated using a single deliquescence relative humidity (DRH) for implementation in the model. Figure 2-3 shows the temperature dependence of the DRH of various single salts and one salt mixture of relevance for the corrosion of copper canisters. The DRH of NaCl, commonly used in studies of the atmospheric corrosion of alloys, is relatively insensitive to temperature and lies in the range 74–76 % RH over the entire temperature range of interest. Sodium nitrate exhibits a lower DRH and the mutual deliquescence relative humidity (MDRH) of a $NaCl + NaNO_3$ mixture lies between that of the two pure salts. Magnesium chloride, a component of evaporated seawater, and $CaCl_2 \cdot xH_2O$ exhibit significantly lower DRH values, in the range 17–34 % RH. Sodium hydroxide is highly deliquescent, a potentially relevant observation for the local chemical conditions close to the cathode within the region of secondary spreading.

In laboratory experiments, the onset of atmospheric corrosion is commonly observed at RH significantly below the thermodynamic DRH. For example, Schindelholz et al. (2014) found evidence for corrosion of carbon steel covered by NaCl at 33 % RH, approximately 40 % below the DRH. Corrosion was due to H_2O adsorbed on the NaCl crystals, possibly enhanced by capillary condensation at the interface between the NaCl particles and the steel surface. At 53 % RH, still 20 % below the DRH, the rate of corrosion was comparable to that at the thermodynamic DRH of 75 %.

In addition to these effects, it has been shown that montmorillonite particles, which will likely be the most abundant surface contaminant for the canister in contact with buffer material, can also lower the DRH of inorganic salts. Attwood and Greenslade (2012) found that the deliquescence of montmorillonite-NaCl contaminated surfaces occurred at 10–15 % RH below that of NaCl alone.

Drying of the canister surface is assumed to occur due to efflorescence of the surface moisture, as defined by the efflorescence relative humidity (ERH). The wetting and drying of surfaces exhibit hysteresis, with efflorescence occurring at lower RH than deliquescence. Figure 2-4 shows a comparison of the DRH and ERH for various pure salts and a $NaCl-NaNO_3$ salt mixture. However, the presence of clay minerals (illite or montmorillonite) has the opposite effect on efflorescence than on deliquescence, increasing the ERH in salt-clay mixtures compared with the value for the salt alone (Ushijima et al. 2018).
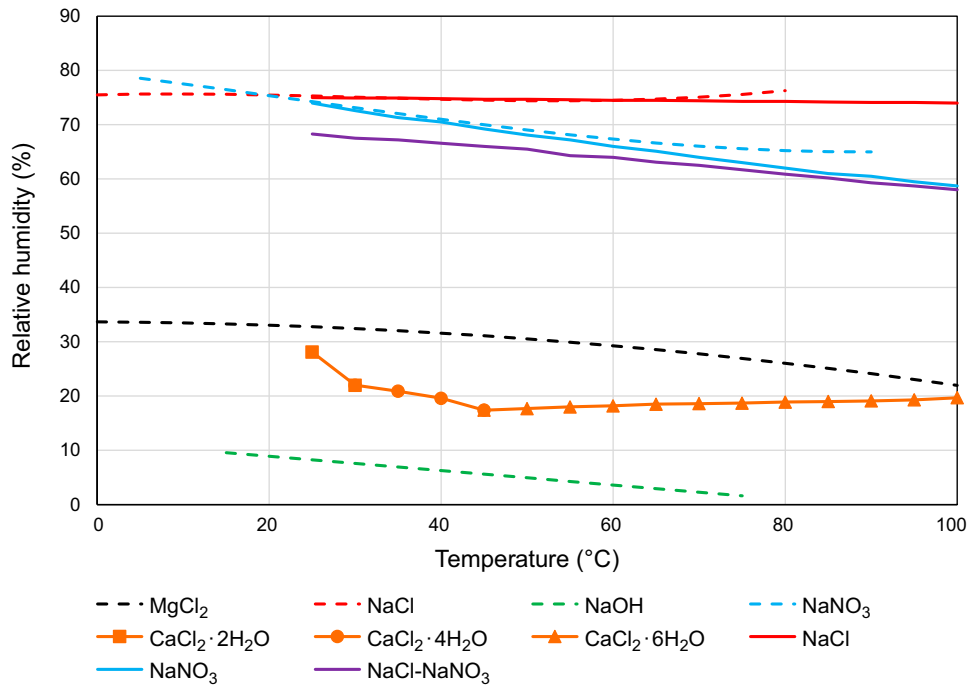
Figure 2-3. *Temperature dependence of the deliquescence relative humidity (DRH) of various salts and salt mixtures based on experimental measurements. Dashed curves from the compilation of Greenspan (1977) and solid curves taken from the review of King (2006).*
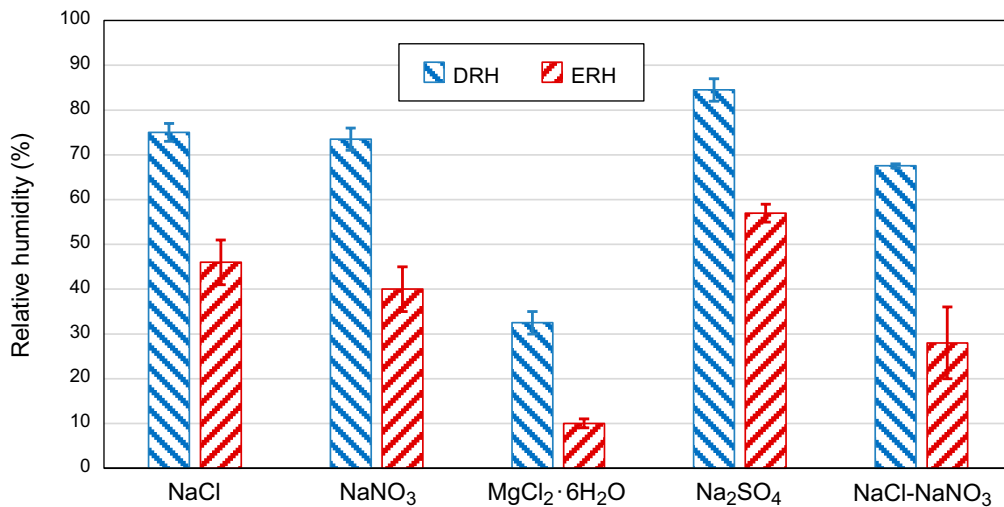
Figure 2-4. *Comparison of deliquescence and efflorescence relative humidities (DRH and ERH, respectively) for various salts and salt mixtures at ambient temperature. The values are the middle of the range of values cited with the error bars indicating the maximum and minimum values. Based on the compilation of data for single salts of Peng et al. (2022) and on Gupta et al. (2015) for the NaCl-NaNO₃ mixture (NaCl mole fraction ≤ 0.3).*

2.3.2 Initiation (birth)

Unlike the saturated pitting model where initiation is conditional on localised film breakdown (Table 2-2), initiation of a pit under unsaturated conditions is assumed to be an inevitable consequence of droplet formation. Spatial separation of anodic and cathodic reactions results from the greater access of O_2 to the underlying copper surface at the edge of the drop, with or without a region of secondary spreading (Figure 2-2(a) and Figure 2-2(b), respectively). Therefore, pits are assumed to initiate in 100 % of the cases in which the canister surface is non-uniformly wetted.

2.3.3 Propagation (growth)

Pits are assumed to propagate until such time that stifling occurs (Section 2.3.4). Pits may grow laterally across the surface or in a depth-wise direction through the corrosion barrier. From the perspective of the canister lifetime, it is the through-thickness penetration that is of most concern. However, lateral growth is also of interest as the tendency for the pit to spread across the surface will limit the depth-wise penetration because the amount of corrosion is ultimately limited by the initial inventory of trapped O_2.

Figure 2-5 illustrates different pit morphologies and their underlying mechanisms. Commonly observed in the pitting of copper potable water pipes (Figure 2-6), hemispherically shaped pits result in the deepest wall penetration of any of the morphologies illustrated (Figure 2-5(a)). Copper does not exhibit low aspect ratio (width < depth) pits sometimes observed on passive alloys. The hemispherical shape of the pit indicates that the growth of the pit is spatially constrained, in the case of Figure 2-6 by the cap of corrosion products.
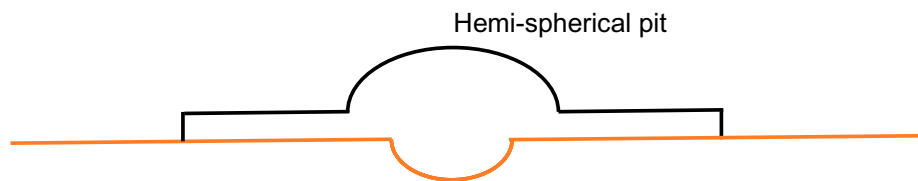
Hemi-spherical pit

(a) Hemispherical pit constrained within the diameter of the original droplet

Lateral growth due to spread of droplet as RH increases
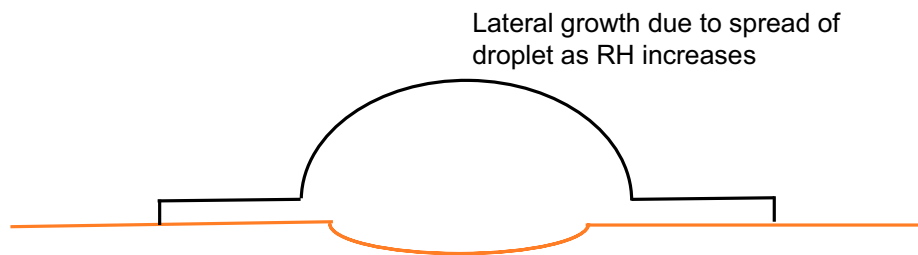
(b) Hemi-ellipsoidal pit constrained within the diameter of a growing droplet

Lateral growth due to joining of anodes
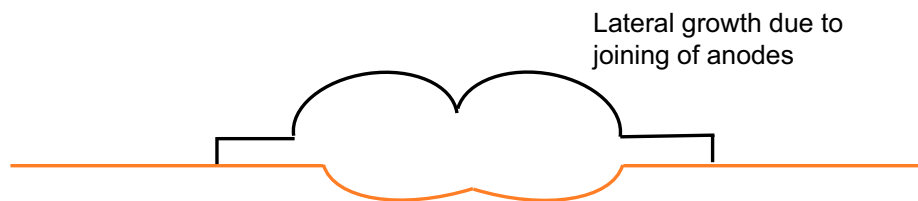
(c) Lateral growth due to coalescence of two or more hemispherical or hemi-ellipsoidal pits

Multiple initiation sites within and adjacent to main droplet
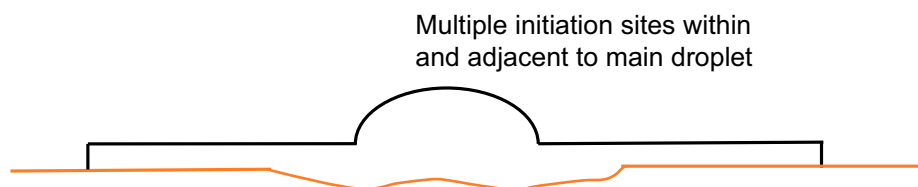
(d) Lateral growth of pit due to progressive initiation of pits due to increase in pH within the region of secondary spreading

Figure 2-5. Schematic illustration of different morphologies of pit propagation.
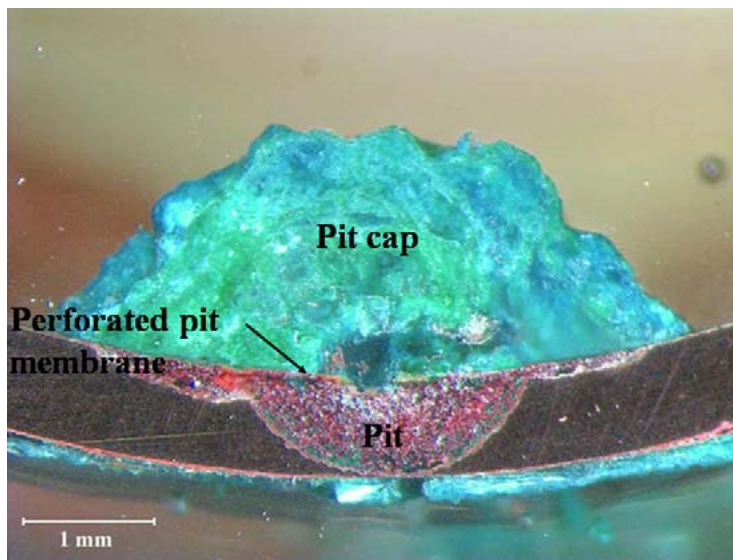
Figure 2-6. *Typical cross-section of a pit in copper potable water pipes (Lytle and Nadagouda 2010).*

If the droplet grows with time, possibly due to an increase in RH resulting in a dilution of the electrolyte, the location of the anodic reaction will also spread laterally and the pit will become hemi-ellipsoidal in shape (Figure 2-5(b)). Because of the iR drop between the internal anode and external cathode, the highest anodic current density will be away from the centre of the droplet closer to the location of the cathodic reaction. Even though the location of the anode is constrained by the cap of corrosion products in Figure 2-6, there is also evidence in the cross-section for the lateral spread of the anodic reaction.

Corrosion will also tend to spread laterally if two adjacent droplets coalesce (Figure 2-5(c)). As with the case of an expanding droplet above, the central region of the combined droplet will tend to corrode more slowly as it is located further away from the cathodic reaction, with the edges of the anodic area corroding preferentially.

The site of the anodic reaction may move away from the centre of the droplet not only to minimise the iR drop between anode and cathode, as above, but also because the nature of the corrosive environment changes (Figure 2-5(d)). As described by Schindelholz et al. (2018), the increase in pH at the cathode around the periphery of the droplet promotes the dissolution of Cu as dissolved $HCuO_2^-$ or CuO_2^{2-} depending on the pH, possibly accompanied by the precipitation of Cu_2O or CuO depending on the potential. As for the cases of growing or coalescing droplets, the shift of the anodic reaction to the periphery of the droplet will tend to isolate the central anodic region from the cathodic current, resulting in a lateral spread of corrosion rather than continued depth-wise penetration.

Comparison of these schematic morphologies with the corroded surface in Figure 2-1 suggests a range of different pit growth behaviours. In keeping with the general observations for copper, all of the pit-like penetrations exhibit aspect ratios (width:depth) $\geq$ 1. There are pit-like features which, in cross-section, are consistent with a hemispherical pit, but there are also cases where pits have, or are about to, coalesce.

The general tendency for the corrosion to spread laterally rather than to penetrate deeply was also observed by Ibrahim et al. (2018), who exposed copper coupons to humid air at 75 °C. Distinct pits were not observed and instead patches of corrosion were found to be associated with the location of water droplets on the surface, as well as areas of more general corrosion (Figure 2-7). The copper coupons were not deliberately contaminated by salts or other potentially deliquescent species prior to exposure, and it is possible that had they been then the corrosion might have been more focussed. In addition, it is important to remember that the coupons were exposed to unlimited atmospheric O_2, unlike the limited O_2 inventory in the repository. Based on the assumption of a constant rate, the maximum rate of depthwise penetration of the copper substrate is approximately 5 µm/yr (assuming a ratio of the volumes of the corrosion product and copper metal of 2).
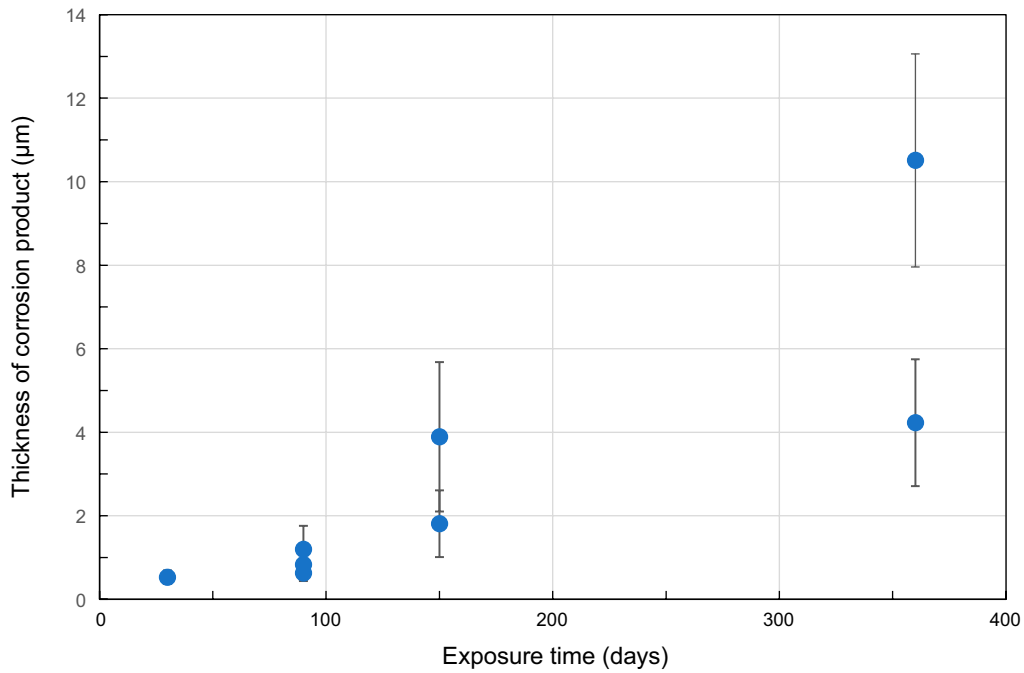
Figure 2-7. *Time-dependent thickness of corrosion products in patches and regions of more general corrosion on copper exposed to humid air at 75 °C (after data from Ibrahim et al. 2018).*

2.3.4 Stifling (death)

Pits will continue to propagate provided that (i) the spatial separation between anode and cathode is maintained and (ii) the cathode can supply sufficient current to the anode. Conversely, if either of these conditions is not met then the pits will stifle (die). The evidence for limited propagation from large-scale *in situ* experiments (Table 2-1) suggests that pits do indeed stifle under repository-relevant conditions.

Here, a number of possible stifling mechanisms are described. The various mechanisms are divided into those related to the evolving redox-hydraulic-thermal conditions in the repository (environmental stifling mechanisms) and those related more to the mechanism of pitting. Table 2-3 summarises the various stifling mechanisms along with the underlying cause in each case. Additional or alternative stifling mechanisms may exist.

Table 2-3. Summary of the stifling mechanisms currently considered for the PUP model and the underlying cause of stifling. Stifling mechanisms #1 relate to the redox-hydraulic-thermal evolution of the repository environment and stifling mechanisms #2 relate to non-environmental causes.

Stifling mechanism #	Stifling mechanism	Underlying cause of stifling
1(a)	Surface dries out	Loss of cathode-anode separation
1(b)	Consumption of O_2	Cathodic limitation
1(c)	Decrease in O_2 supply due to water saturation	Cathodic limitation
1(d)	Dilution of deliquesced electrolyte	Cathodic limitation
1(e)	Uniform wetting of the surface	Loss of cathode-anode separation
2(a)	Formation of less-catalytic cathode	Cathodic limitation
2(b)	Blocked cathode	Cathodic limitation
2(c)	Lateral spread of anodic reaction	Cathodic limitation
2(d)	Droplet coalescence	Cathodic limitation
2(e)	iR drop in thin electrolyte layer	Cathodic limitation
2(f)	iR drop due to precipitation within droplet	Cathodic limitation
2(g)	Loss of critical pit chemistry	Loss of cathode-anode separation

Environmental stifling mechanisms

1(a) Surface dries out

Notwithstanding the requirement that the surface needs to be wet in order to initiate a pit (Section 2.3.1), subsequent drying of the surface will stifle pit growth. Such a situation may occur during the initial thermal-hydraulic transient if the surface is initially wet and the moisture is driven away from the canister due to the thermal gradient (Section 3.2.2). Alternatively, drying of the surface can occur as a consequence of the formation of a less-deliquescent corrosion product following initial deliquescence and consumption of the original surface salt contaminant (Situm et al. 2024).

1(b) Consumption of O_2

Atmospheric corrosion of copper cannot be sustained in the absence of gaseous O_2. Although Cu^{2+} can also act as an oxidant for copper pitting, as in the Lucey mechanism for Type 1 pitting of copper potable water pipes (Lucey 1967), the cupric ion is formed by the homogeneous oxidation of Cu(I) by O_2, so that the latter species is still required for sustained pit growth.

According to Galvele's pit stability criterion for passive materials, a sufficient rate of hydrolysis of dissolved metal ions is required to maintain acidic conditions within the pit and to prevent repassivation (Galvele 1976). In turn, this implies that there must be a sufficient rate of O_2 reduction to supply the cathodic current, which forms the basis for the atmospheric pitting model of Chen and Kelly (2010). If there is insufficient cathodic current, for example, due to a decrease in O_2 partial pressure, the pit will stifle. If we extend this model to the pitting of copper canisters in the repository, then it implies that there is a threshold $[O_2]$ below which pits will stifle.

The consumption of the initially trapped O_2 in the repository is the consequence of a number of processes (Figure 2-8) , including:

- Corrosion of the canister.

- Corrosion of metallic materials used in the construction of the repository and not removed prior to closure.

- Oxidation of accessory minerals in the bentonite buffer and backfill and in the host rock.

- Aerobic microbial activity in regions of the near-field where such activity is possible.

- Sorption of O_2 by the bentonite, although it is uncertain whether this process is reversible, in which case it would not result in permanent sequestration of the O_2.
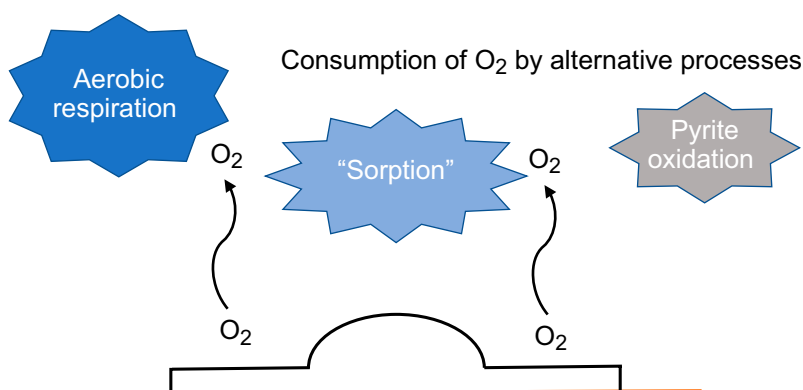
Figure 2-8. *Schematic illustration of pit stifling by consumption of the initially trapped O_2 by processes other than pit growth.*

The duration of aerobic conditions in the repository is somewhat uncertain, with evidence from both laboratory experiments and full-scale tests indicating timescales of a few weeks to a year or longer (SKB 2022b). Without identifying the specific processes responsible, Briggs et al. (2020, 2021) simulated the rate of O_2 consumption using an exponential expression:

$$[O_2] = [O_2]_{init} \cdot e^{-\alpha t} \tag{2-1}$$

where $[O_2]_{init}$ is the initial O_2 concentration and a is a time constant describing the rate of O_2 consumption with time t.

1(c) Decrease in O_2 supply due to water saturation

In addition to consumption by one or more of the processes listed above, the flux of O_2 to the canister surface (and, hence, the maximum cathodic current) will also decrease as the near-field saturates. The effective diffusivity of O_2 in unsaturated pores is 4–5 orders of magnitude higher than that in saturated buffer (Posiva 2021). Thus, as the buffer approaches saturation, the ability of the cathode to supply sufficient current to support the anode will be reduced (Figure 2-9).

However, as illustrated in Figure 1-1, it is expected that the rate of O_2 consumption will exceed the rate of buffer saturation so that this stifling mechanism may not occur under repository conditions.

1(d) Dilution of deliquesced electrolyte

Stifling will also occur if the anodic area becomes too large for the cathode to support. One mechanism by which this could occur is an increase in the droplet size due to an increase in RH (Figure 2-10). As the RH increases, the equilibrium solute concentration decreases and the droplet size increases as a consequence.

Decrease in O_2 supply due to buffer saturation
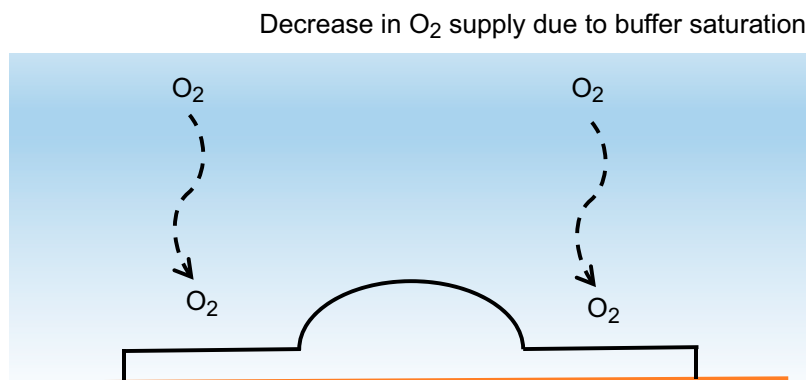
Figure 2-9. Stifling of pit growth by a decrease in O_2 supply due to saturation of the near-field.

Dilution of electrolyte and decrease in C:A
surface area ratio due to increase in RH
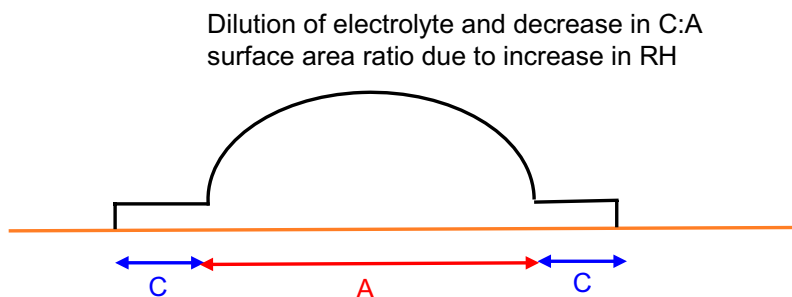
Figure 2-10. Stifling due to a decrease in cathode:anode surface area ratio as a result of an increase in RH. The horizontal red and blue arrows indicate the location of the anode (A) and cathode (C), respectively.

The rate of change of droplet size and the resulting impact on the cathode:anode (C:A) surface area ratio, however, may be minimal under repository conditions. Figure 2-11 shows the dependence of the equilibrium solute concentration on RH for three common salt contaminants. Taking NaCl as an example, the equilibrium concentration decreases by a factor of five, from 5 mol/kg to 1 mol/kg, as the RH increases from 81 % to 97 %. A 5-fold increase in droplet volume will result in a 2.9-fold increase in cross-sectional area of the anode (equivalent to $(5)^{2/3}$), based on the simplified geometry illustrated in Figure 2-10. The surface area of the cathode will also increase as the central droplet grows, even if the width of the region of secondary remains unchanged. Thus, the C:A surface area ratio may decrease by a factor of ~2 for this increase in RH from 81 % to 97 %.

The length of time for the near-field RH to change by this amount will depend on the local hydraulic conductivity but, based on the data presented in Section 3.2.2, could be as little as 1–2 years for an overall repository saturation time of 20 years and > 50 years for overall saturation times of 100 years or longer. Even for the fastest saturation time, the atmospheric [O_2] is likely to change by more than a factor of 2 within this period of time. Therefore, the effect of dilution of the electrolyte on the ability of the cathode to supply sufficient current to the anode due to the change in C:A surface area ratio is likely to be small compared with that due to the overall consumption of the atmospheric O_2.

(1e) Uniform wetting of the surface

Maintenance of pit growth depends on the continuing spatial separation of anode and cathode. While non-uniform wetting leads to spatial separation of anode and cathode and pit initiation, uniform wetting of the surface will result in the opposite effect and cause propagating pits to stifle. This situation is illustrated schematically in Figure 2-12 where the anodic and cathodic reactions are shown occurring over the entire wetted surface. However, Chen et al. (2004) have suggested that, even at 95 % RH, the adsorbed water layer thickness remains non-uniform even though the entire surface may be wetted to some degree, with thicker layers at the locations of the precursor salt particles. Thus, completely uniform wetting of the surface may not be achieved until the RH approaches 100 %.
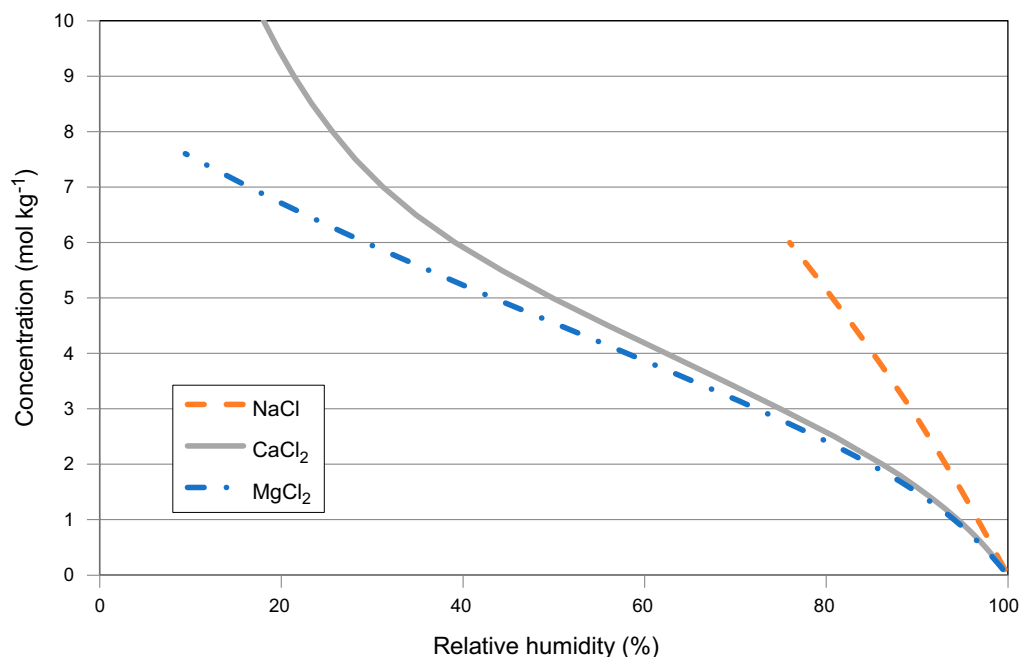
Figure 2-11. *Variation of the equilibrium solute concentration with relative humidity for three common salt contaminants. Data for NaCl and CaCl$_2$ from Robinson and Stokes (1959) and for MgCl$_2$ from Tang et al. (1997).*
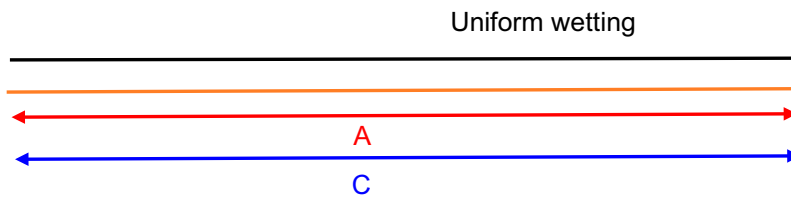
Uniform wetting

Figure 2-12. *Illustration of the uniform wetting of the copper surface resulting in overlapping anodic and cathodic reactions. The horizontal red and blue arrows indicate the location of the anode (A) and cathode (C), respectively.*

Non-environmental stifling mechanisms

2(a) Formation of less-catalytic cathode

The ability of the cathode to supply sufficient current to the anode will not only depend on the rate of supply of O_2 but also on the interfacial kinetics of the oxygen-reduction reaction (ORR) (Figure 2-13). It is known that the presence of a Cu_2O layer inhibits the rate of the ORR compared with that on a freshly polished copper surface (King et al. 1995a,b). Alternatively, CuO may precipitate on the cathode as a result of the increase in pH due to the ORR (Chen et al. 2005b, Schindelholz et al. 2018).

2(b) Blocked cathode

The catalytic nature of the cathode could also be compromised through the precipitation of insulating species from the electrolyte, such as Na_2CO_3 (Chen et al. 2005a) or $CaCO_3$ as a result of CO_2 absorption in the alkaline solution near the cathode (Figure 2-14).

The formation of a less-efficient cathode, either through the formation of a less-catalytic surface (case 2(a)) or because of blocking by an insulating species (case 2(b)), leads to stifling because the cathode is unable to supply sufficient current to the anode (Table 2-3).

Formation of less-catalytic Cu_2O surface
in region of secondary spreading
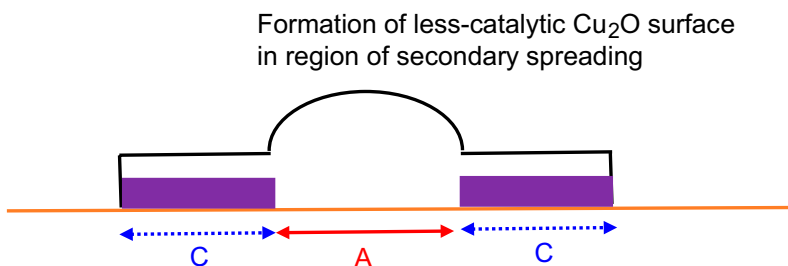
Figure 2-13. *Pit stifling because of the formation of a less-catalytic surface on the cathode. The horizontal red and blue arrows indicate the location of the anode (A) and cathode (C), respectively, with the dotted blue line indicating a decrease in the cathodic kinetics.*
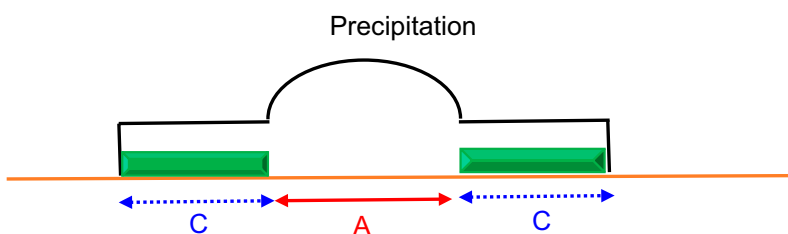
Precipitation

Figure 2-14. *Pit stifling because the cathode becomes blocked by the precipitation of an insulating surface film. The horizontal red and blue arrows indicate the location of the anode (A) and cathode (C), respectively, with the dotted blue line indicating a decrease in the cathodic kinetics.*

2(c) Lateral spread of anodic reaction

As discussed in Section 2.3.3, there are a number of mechanisms by which the location of the anodic reaction can spread laterally from the central droplet. Not only will this change the morphology of the corrosion damage, but it may also promote stifling of the pit through a decrease in the C:A surface area ratio (Figure 2-15).

Lateral spreading of the anodic reaction results in a decrease in C:A surface area ratio and causes stifling because the cathode is unable to supply sufficient current to maintain dissolution at the anode (Table 2-3).

2(d) Droplet coalescence

The C:A surface area ratio will also decrease as a consequence of the coalescence of neighbouring droplets (Figure 2-16). As illustrated in Figure 2-17, the C:A ratio is smaller for coalesced droplets, with or without secondary spreading of the droplet. This stifling mechanism becomes more likely at higher surface salt loadings where the spacing between neighbouring salt crystals will be smaller. Droplet coalescence will also be promoted by an increase in RH as the droplet size increases in response to the dilution of the deliquesced solution.

Droplet coalescence results in a decrease in C:A surface area ratio and causes stifling because the cathode is unable to supply sufficient current to maintain dissolution at the anode (Table 2-3).
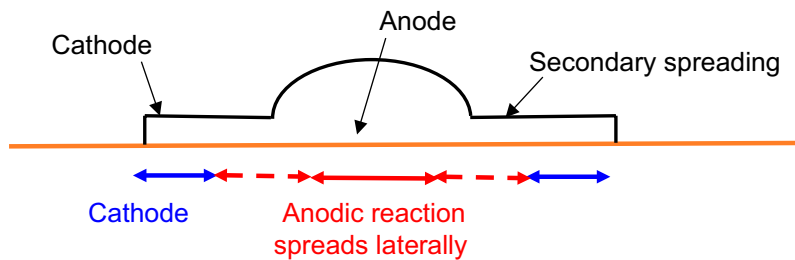
Figure 2-15. *Consequence of lateral spreading of the anodic reaction on the cathode:anode surface area ratio. The horizontal red and blue arrows indicate the location of the anode (A) and cathode (C), respectively, with the dashed red line indicating lateral growth of the anodic reaction.*
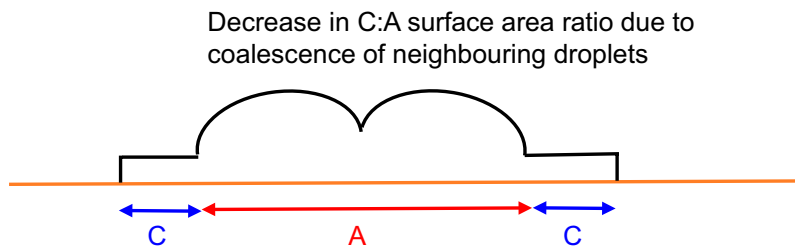
Figure 2-16. *Effect of droplet coalescence on the cathode:anode surface area ratio. The horizontal red and blue arrows indicate the location of the anode (A) and cathode (C), respectively.*
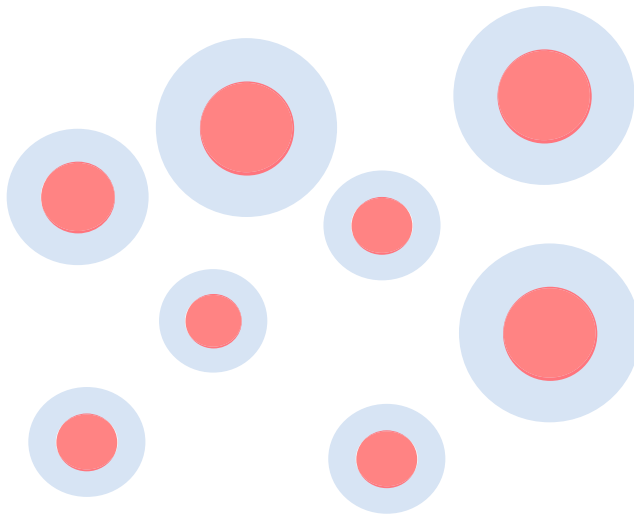
(a) Isolated droplets
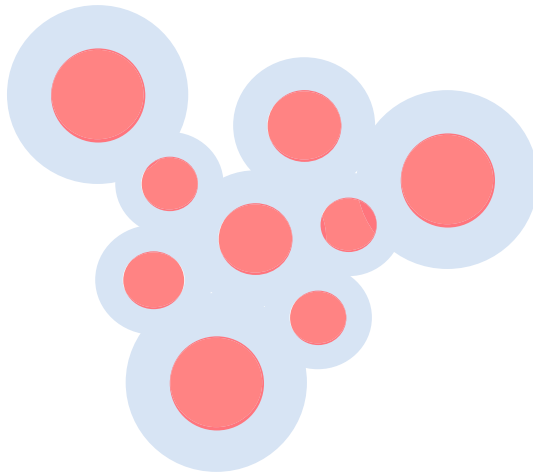
(b) Coalesced droplets

Figure 2-17. Comparison of the effective cathode:anode surface area ratio for (a) isolated droplets and (b) coalesced droplets. Red areas indicate the anode and blue regions indicate the cathodic areas.

2(e) iR drop in thin electrolyte layer

Pit growth involves galvanic coupling of the (external) cathode to the (internal) anode. The efficiency of this galvanic couple will be impacted by voltage (iR) drops through the electrolyte between the anode and cathode, which in turn is dependent on the specific resistance of the solution and the dimensions of the conductive path (Figure 2-18). The resistance (R) of an electrolyte solution is given by (Robinson and Stokes 1959):

$$R = \rho \frac{l}{A} \tag{2-2}$$

where r is the specific resistance of the solution and l and A are the length and cross-sectional area of the conductive path, respectively. In general, the specific resistance of an electrolyte solution increases with decreasing concentration or, expressed differently, the higher the concentration the more conductive the solution. In a deliquesced solution, therefore, the resistance increases with RH as the solution becomes progressively more dilute (cf. Figure 2-11). Figure 2-19 shows the specific resistance of deliquesced solutions as a function of the RH for a number of relevant electrolytes, based on the dependence of the equilibrium concentration on RH (from Figure 2-11) and the dependence of the specific resistance on concentration (CRC 2019, Robinson and Stokes 1959). For most solutes, the specific resistance only increases significantly at RH values > 95 %. The one exception is NaOH solution, which could be formed close to the cathode due to the increase in pH resulting from the reduction of O_2, for which the specific resistance starts to increase at RH > 80 %.
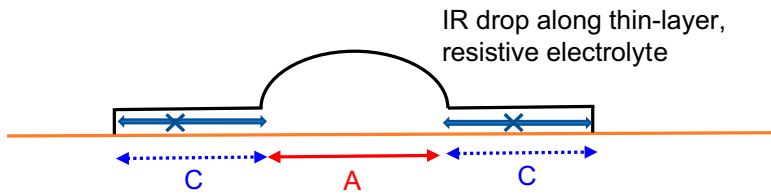
Figure 2-18. *Schematic illustration of voltage (iR) drop in the thin electrolyte layer in the region of secondary spreading.*
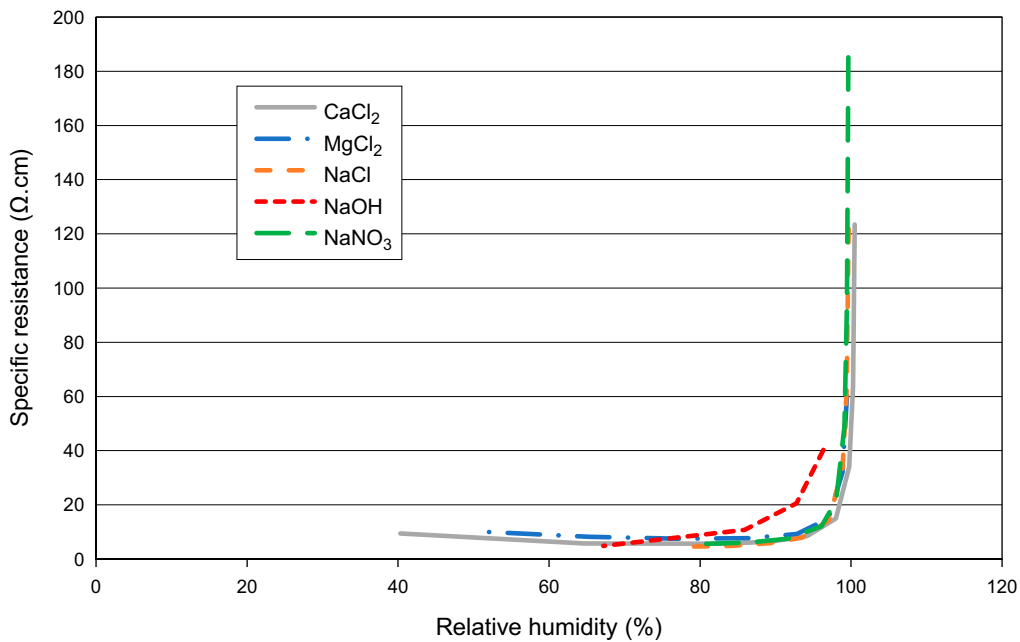
Figure 2-19. *Dependence of the specific resistance on relative humidity for deliquesced electrolyte solutions in equilibrium with a humid atmosphere.*

The resistance is also a function of the length of the conductive pathway (l) and the cross-sectional area (A). Thus, the greater the extent of secondary spreading and/or the thinner the electrolyte layer, the higher the resistance at a given RH.

The value of the solution resistance between the anode and cathode at which the pit will stifle is not known *a priori*, but can be estimated based on a suitable numerical model. In addition to promoting stifling, the solution iR drop will also cause the location of the anode to shift towards the periphery of the droplet since the galvanic current will be greater the shorter the distance between anode and cathode. Thus, the iR drop will cause the corrosion to spread laterally as well as possibly limit the overall extent of damage.

2(f) iR drop due to precipitation within droplet

An increase in cell resistance can also result from precipitation of corrosion products within the pit (Figure 2-20). Such a mechanism has been reported for the pitting of copper in potable water and is associated with a decrease in potential and current density at the base of the pit due to the increase in pit resistance (Ha et al. 2011).

Pit stifling due to iR drop through either the solution (case 2(e)) or because of precipitation within the pit (case 2(f)) is a result of the inability of the cathodic to supply sufficient current to the anode (Table 2-3).
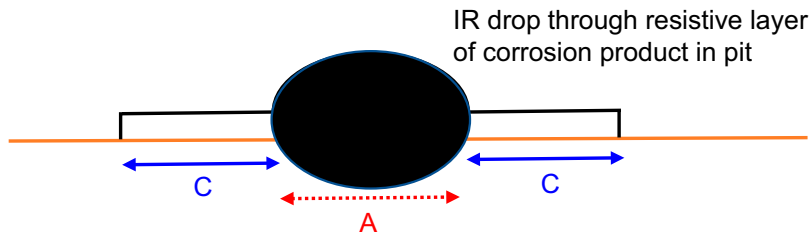
Figure 2-20. Schematic illustration of voltage (iR) drop due to precipitation of corrosion products within the pit.

2(g) Loss of critical pit chemistry

For many localised corrosion systems, continued dissolution is dependent on the maintenance of an anaerobic, acidic, and conducting environment within the occluded region. In systems prone to passivation, the maintenance of this critical chemistry prevents repassivation and stifling of the pit or crevice. The mound of precipitated corrosion products commonly observed for the pitting of copper pipes in potable water (Figure 2-6) prevents the transport of dissolved Cu ions out of the pit, the resulting hydrolysis of which creates a more-acidic environment immediately above the pit than in the bulk environment. To maintain charge balance, aggressive anions (Cl^- and/or SO_4^{2-}) diffuse through the corrosion product cap from the bulk environment.

The loss of the critical pit chemistry will lead to stifling because there is then no longer any spatial separation between the anode and cathode (Figure 2-21, Table 2-3). Such a mechanism may not be relevant for atmospheric pitting because the dissolved species within the pit cannot be easily transported into the bulk environment, as is the case for saturated systems. However, this potential stifling mechanism is retained here for completeness.
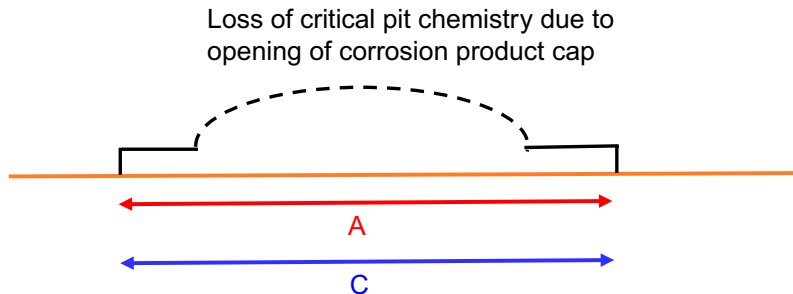
Figure 2-21. Loss of critical pit chemistry due to opening of the corrosion product cap resulting in stifling because there is no longer spatial separation of the anodic and cathodic reactions.

3 Implementation of the probabilistic pitting model

As for the probabilistic model for the pitting of copper canisters under saturated conditions (Briggs et al. 2020, 2021), the structure of the PUP model is based on a series of flow charts. Flow charts are used (i) to control execution of a single realisation, (ii) to determine whether the environment is suitable for pit growth, and (iii) to assess the extent of pit damage if the pit does not stifle due to non-environmental reasons. For the current stage of model development, only potential stifling mechanisms related to the evolution of the environmental conditions (cases 1(a) to 1(e) in Section 2.3.4) are considered. Non-environmental stifling mechanisms (cases 2(a) to 2(g), Section 2.3.4) may be included as part of future model development.

3.1 Conceptual model

3.1.1 Control flow chart

The main purpose of the control flow chart (Figure 3-1) is to control the overall execution of a single realisation and to terminate the run. A series of such realisations, typically of the order of one million runs, constitutes a full probabilistic simulation. An individual realisation represents the time-dependent pitting behaviour of a single canister in a deposition hole. The run, or realisation, is terminated when either the canister is deemed to have failed or the realisation has reached a user-defined maximum time, which for the current simulations has been arbitrarily set to 100 000 years, even though this time is far beyond the period of oxidising conditions.

At the start of each realisation, profiles for the time-dependent canister temperature and near-field RH are selected from the corresponding distributions (see Sections 3.2.1 and 3.2.2, respectively). A value of the deliquescence RH (DRH), i.e., the RH at which surface wetting first occurs (Section 3.2.3), is also selected from a suitable distribution. The simulation time is then incremented and wetting of the surface is determined based on the criterion:

RH ≥ DRH (3-1)

If this criterion is not met, then the time is incremented and the condition re-tested.

Once wetting is deemed to occur, the code progresses to the environment module (Figure 3-2). If it is determined that the conditions do not support pitting based on a number of additional environmental criteria even though the surface is wetted, then this condition is documented and the time is incremented. The process is repeated until the maximum simulation time is reached, in part to allow for the possibility of pit re-initiation should the environmental conditions be suitable.

If, on the other hand, the surface is wet and the environmental conditions support pitting, then the code proceeds to assess the extent of pit propagation. The pit propagation module (Section 3.1.3) also includes a number of conditions for pit stifling and, if stifling is deemed to occur, the reason is documented and the time is incremented. Otherwise, both the incremental and cumulative extent of pit propagation are determined, with the latter compared to the corrosion allowance to determine if the allowance has been exceeded. Once penetration of the corrosion allowance occurs, the time is recorded and the realisation is terminated. If penetration has not occurred, the time is incremented and the above steps are repeated until either the point of canister failure or the maximum simulation time is reached.
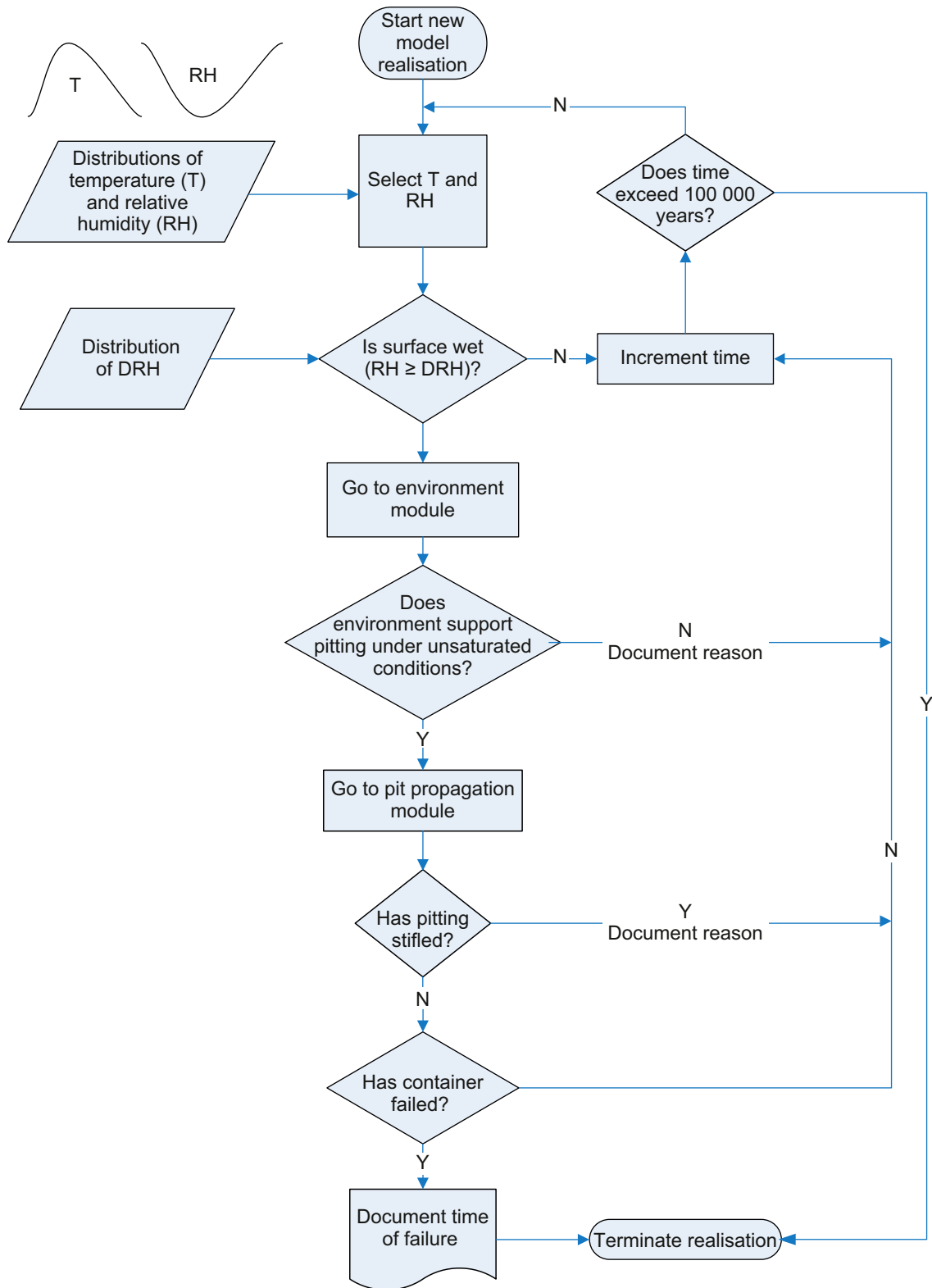
Figure 3-1. *Control flow chart for the probabilistic pitting model for aerobic, unsaturated conditions.*

3.1.2 Environment flow chart

The purpose of the environment module (Figure 3-2) is to determine whether the environmental conditions are suitable for pit propagation. Wetting of the surface has previously been established within the control module, but pitting via the Evans droplet mechanism requires that the surface be non-uniformly wetted. This condition is established based on the criterion:

$$RH \geq RH_{SAT} \tag{3-2}$$

where RH_{SAT} is the RH at which the surface is considered to be uniformly covered by a continuous film of electrolyte (stifling mechanism 1(e), Section 2.3.4). The value of RH_{SAT} is sampled for each realisation (Section 3.2.6).

The second criterion for pit propagation assessed in the environment module is that the cathode:anode surface area ratio is sufficient to support pit growth (stifling mechanism 1(d), Section 2.3.4). A threshold RH (RH_{thresh}) is defined for each run, below which pit propagation is possible, with pit stifling occurring if the following criterion is met:

$$RH \geq RH_{thresh} \tag{3-3}$$

Finally, the third environmental criterion for pit propagation is that there must be sufficient O_2 present to support pit growth (stifling mechanism 1(b), Section 2.3.4). Pit stifling occurs if the criterion

$$[O_2] \leq [O_2]_{thresh} \tag{3-4}$$

is satisfied, where $[O_2]_{thresh}$ is the minimum $[O_2]$ for pit growth (Section 3.2.6).

These three criteria are examined in the sequence above, as illustrated in Figure 3-2. For example, pit stifling due to insufficient O_2 is only possible if the surface is non-uniformly wetted ($RH < RH_{SAT}$) and the electrolyte is not too dilute ($RH < RH_{thresh}$).
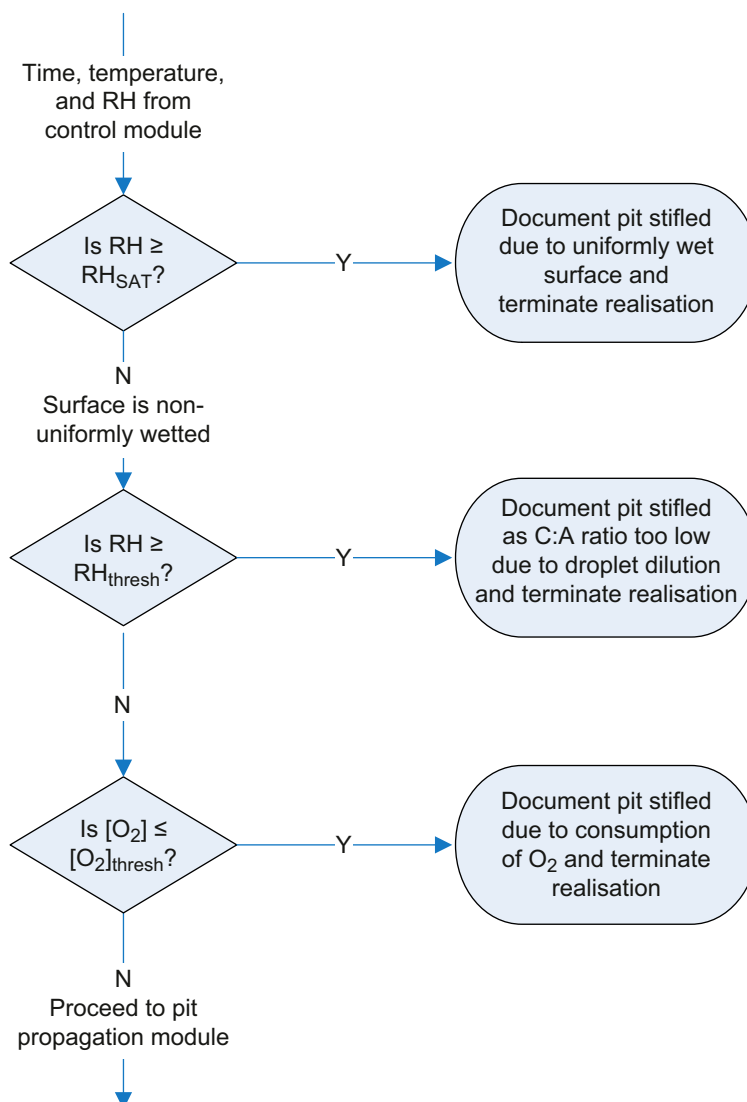
Figure 3-2. Environment flow chart for the probabilistic pitting model for aerobic, unsaturated conditions.

Pit stifling because of limited O_2 supply in saturated buffer (stifling mechanism 1(c), Section 2.3.4) has not been implemented in the current version of the model as the saturation time is expected to far exceed the duration of the aerobic period in the repository.

3.1.3 Empirical pit propagation flow chart

If the surface is wetted and the environment is suitable for pit propagation, then the code proceeds to the pit propagation module (Figure 3-3).

Although not considered for the current version of the code, the pit propagation module includes criteria for assessing whether pits will stifle for non-environmental reasons (stifling mechanisms 2(a) to 2(g) in Section 2.3.4). Prior to assessing the extent of pit growth, additional stifling criteria would be tested, including:

- Coalescence of neighbouring pits, leading to a decrease in cathode:anode surface area ratio (mechanism 2(d)).

- Cathodic limitation due to high iR drop across the thin layer of electrolyte within the region of secondary spreading where the cathode is located or within the pit due to the precipitation of corrosion products (mechanisms 2(e) and 2(f), respectively).

- Suppression of the cathode by an electrochemically less-catalytic surface layer or by the precipitation of an (electrically) insulating film (mechanisms 2(a) and 2(b), respectively).

Although lateral spreading of the anodic reaction could lead to pit stifling (mechanism 2(c)), this phenomenon is included in the current analysis through the use of an empirical pit growth expression that takes into account lateral growth of the pit. Pit stifling by the loss of the critical pit chemistry (mechanism 2(g)) is not implemented as it is uncertain whether such a mechanism applies under unsaturated conditions.
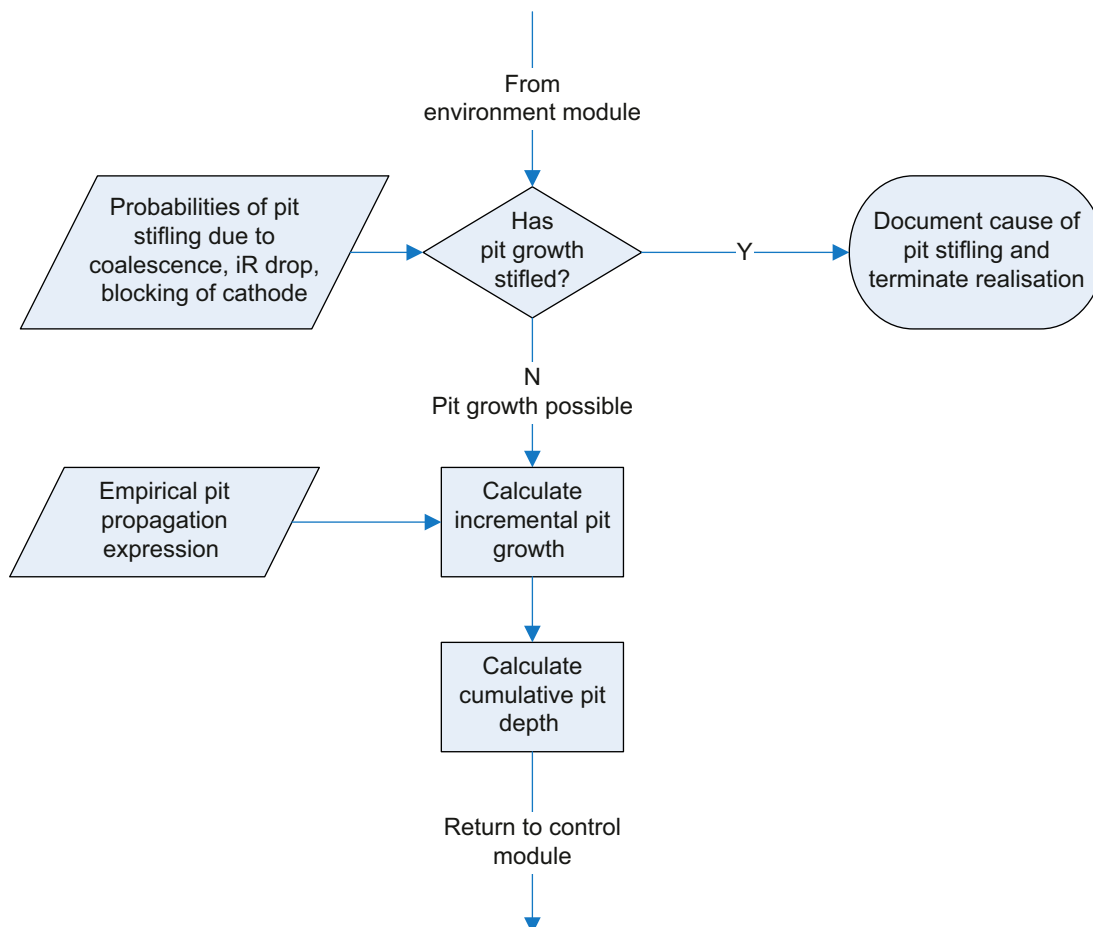
Figure 3-3. *Pit propagation flow chart for the probabilistic pitting model for aerobic, unsaturated conditions.*

If the pit is not stifled for any of these non-environmental reasons (as in the current simulations), pit growth occurs. Both the incremental pit growth for that time step and the cumulative pit growth to date are estimated, with the latter used in the control module to determine if the canister has failed due to a through-wall pit. The "pit age" is defined as the elapsed time from pit initiation to pit stifling.

Depending on the stifling mechanism, it is possible that a stifled pit could reinitiate at a later time. For example, if an initiated pit stifles because the surface dries out (stifling mechanism 1(a)), the pit could re-initiate if the surface subsequently re-wetted *and* if no other stifling mechanism (such as the consumption of O_2, stifling mechanism 1(b)) was operative. This scenario is most likely for a combination of a slow rate of O_2 consumption and a low $[O_2]$ threshold. If conditions for re-initiation do occur, growth of the pit is considered to be cumulative. The pit growth rate for the second period of propagation is assigned the same growth rate as during the first propagation phase. If the pit growth rate is time-dependent, then the growth rate re-sets to the initial growth rate for the second propagation phase.

The empirical pit growth expressions used for the current simulations are described further in Section 3.2.5.

3.2 Input data

3.2.1 Canister temperature

The time-dependent canister surface temperature is sampled from a collection of temperature profiles for each of the 6 916 positions in the repository at Forsmark. Temperature calculations were performed by Allan Hedin using the thermal model described in Hedin (2004) along with thermal properties appropriate for unsaturated buffer. For the probabilistic model simulations, temperatures were interpolated using a piecewise cubic method from those predicted by the thermal model to correspond to the time increments used for the Monte Carlo simulations. For times less than 0.01 years (the earliest output from the thermal model), the temperature was assumed to be constant at this initial value. Figure 3-4 shows a random collection of 100 of the total number of 6 916 temperature profiles.

For each Monte Carlo realisation, the 6 916 temperature profiles are sampled using a discrete uniform distribution with no consideration of duplicate selection. A single temperature profile was selected for each of the one million realisations used for the full probabilistic analysis.
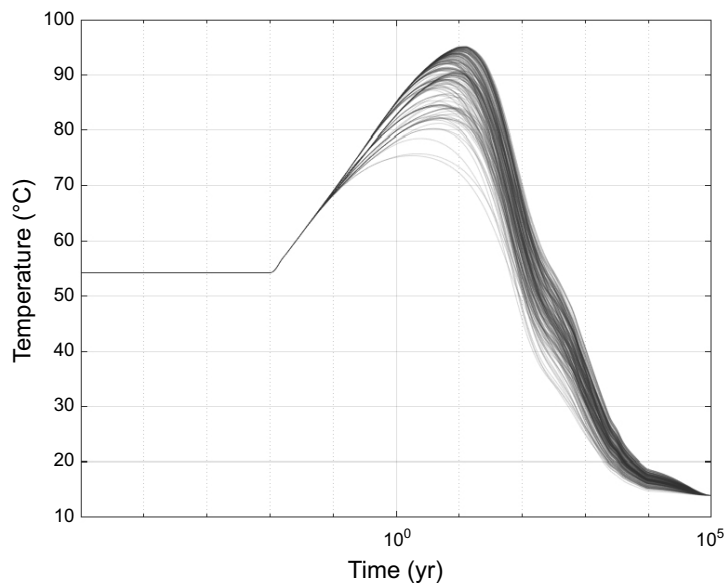
Figure 3-4. A collection of one hundred of the total of 6 916 individual temperature profiles calculated based on thermal properties for unsaturated buffer.

However, since none of the other parameters in the model is temperature-dependent for the current analysis, the selection of a thermal profile is somewhat redundant. Nevertheless, the capability of sampling the temperature profiles is retained in the code in case any of the input data are treated as being temperature dependent in future implementations of the model.

3.2.2 Near-field relative humidity

Expressions for the time-dependent RH at the canister surface were provided by Malmberg and Åkesson (2020). The form of the time dependence of the RH is shown in Figure 3-5. The RH profile is characterised by a dry-out phase up to time t_d and a wetting phase, from time t_d up until the time of complete saturation of the buffer t_S. The dry-out behaviour is determined by the heat output from the canister and, for the current assumption of a constant heat output from all canisters, is the same for all deposition holes. The saturation time, on the other hand, varies spatially within the repository depending upon whether water enters the deposition hole via fractures or through the rock matrix. There is also uncertainty in the value of the hydraulic conductivity for matrix flow. Together, the natural spatial variability along with the uncertainty, result in a range of saturation times ($t_{S,1}$, $t_{S,2}$, $t_{S,3}$, etc) leading to a distribution in the wetting portion of the RH profile.

Based on the model of Malmberg and Åkesson (2020), the time (t)-dependence of the RH during the drying period (RH_{dry}) is given by

$$RH_{dry} = \frac{24}{1+e^{3.5(\log(t)-\log(t_{0,dry}))}} + RH_0 \qquad (3\text{-}5)$$

where RH_0 and $t_{0,dry}$ are equal to 47 % and 0.22 years, respectively.

The wetting part of the RH profile (RH_{wet}) is given by

$$RH_{wet} = \frac{53}{1+e^{-k(\log(t)-\log(t_{mid}))}} + RH_0 \qquad (3\text{-}6)$$

where k and t_{mid} are related to the saturation time t_S by

$$t_{mid} = 4.9 \times t_S^{0.43} \qquad (3\text{-}7)$$

and

$$k = \frac{3.4}{\log(t_S)-\log(t_{mid})} \qquad (3\text{-}8)$$

The RH at any given time is then given by the maximum value of either Equation (3-5) or Equation (3-6).
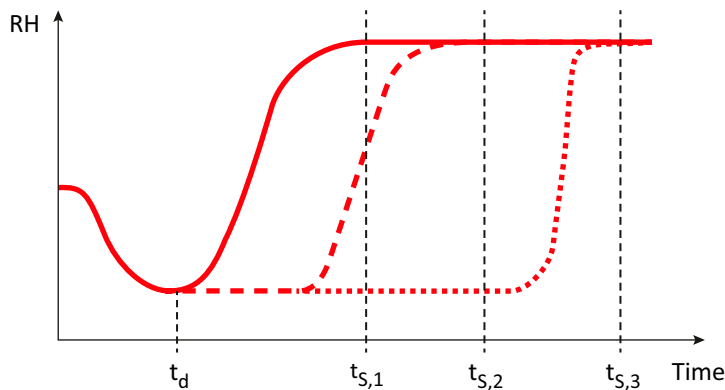
Figure 3-5. *Form of the time-dependence of the relative humidity (RH) at the canister surface assumed for the PUP model (Malmberg and Åkesson 2020).*

As noted above, there is spatial variability and uncertainty in the saturation time. Based on an assumption of a truncated log-normal distribution of matrix hydraulic conductivity (K_{matrix}) with maximum and minimum values of 10^{-13} m/s and 10^{-14} m/s, respectively, the distribution of saturation times based on 100 samples of K_{matrix} is shown in Figure 3-6. The upper and lower bounds of the K_{matrix} distribution correspond to saturation times of 1 500 years and 18 000 years, respectively. In Figure 3-6, saturation times of < 1 800 years correspond to cases in which fracture flow is responsible for buffer saturation.

Figure 3-7 shows the collection of RH profiles calculated from Equations (3-5) and (3-6) and the distribution of saturation times in Figure 3-6. As noted above, all deposition holes have the same RH profile during the drying phase, but then exhibit different wetting behaviour as a result of the distribution in saturation times. Based on Equation (3-5), the initial RH of the as-emplaced buffer is 71 %.
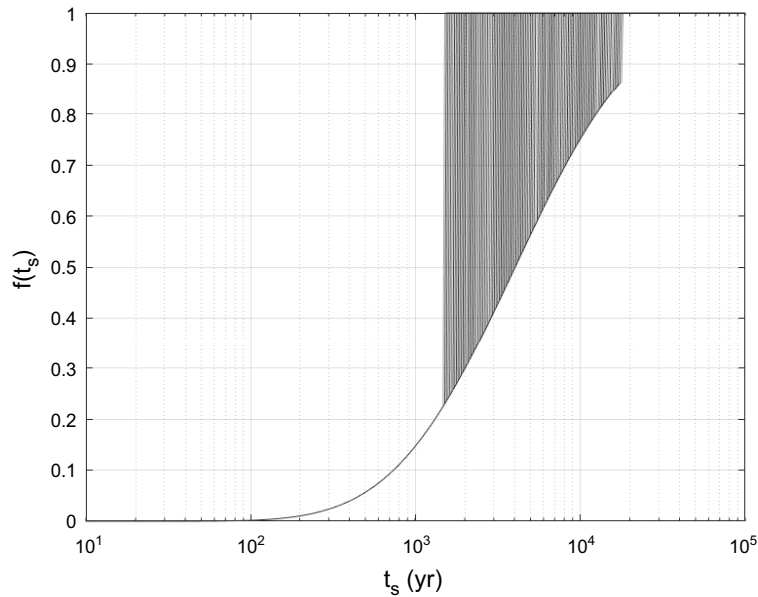
Figure 3-6. *Distribution of saturation times $f(t_S)$ based on one hundred samples of the matrix hydraulic conductivity.*
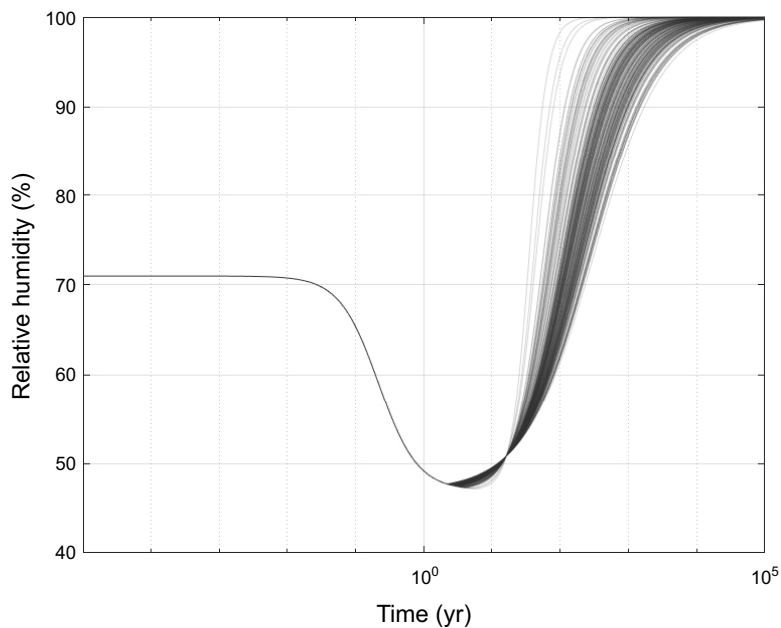
Figure 3-7. *A collection of one hundred relative humidity profiles based on the distribution of saturation times in Figure 3-6.*

Finally, although the canister temperature is not used in the current model simulations, it is important to note for future model developments that it is not necessary to correlate the selected temperature and RH profiles. As will be shown below, the maximum expected pit lifetime lies within the drying-out period during which the RH profiles are the same for all deposition holes.

3.2.3 Relative humidity thresholds

Deliquescence relative humidity

Based on the discussion in Section 2.3.1, it is apparent that there is uncertainty in the selection of the DRH. This uncertainty arises not only from the condition of the canister surface and the nature of possible deliquescent species, but also from experimental observations that corrosion can occur at RH significantly below the thermodynamically predicted DRH (Schindelholz et al. 2014).

In order to address this variability and uncertainty, the DRH is treated as a distributed parameter in the PUP, with a single value selected from a suitable distribution for each realisation. In the simulations reported here, a sensitivity analysis was performed involving various ranges for the DRH:

- 55–75 % RH

- 35–60 % RH

- 35–75 % RH

- 35 % RH

In the first three cases, the DRH is assumed to be uniformly distributed between the minimum and maximum values. Not all DRH ranges were combined with all of the O_2 consumption times investigated (next section).

In the current PUP model, the DRH is assumed not to be a function of temperature.

The DRH range of 55–75 % RH is based on the assumption that NaCl (DRH = 74–76 % RH, Figure 2-3) is the principal deliquescent species, but that the DRH could be as low as 55 % RH due to the presence of montmorillonite particles and/or a porous surface morphology. The maximum RH in the range exceeds the initial RH of the buffer, so pit initiation will not occur in some deposition holes until the wetting phase (if other factors have not otherwise resulted in pit stifling by that time, e.g., stifling due to insufficient O_2). The minimum RH in the range represents the condition under which the surface dries out.

The DRH range of 35–60 % RH is representative of a more-deliquescent surface contaminant than NaCl or suppression of the DRH for NaCl by montmorillonite particles, a porous surface layer, or a secondary salt such as $NaNO_3$ (possibly formed from the radiolysis of humid air). Since the maximum value of the range is lower than the initial RH, non-uniform wetting and pit initiation will occur in all realisations. The minimum RH in the range represents a surface that only dries out at a minimal degree of saturation.

The DRH range of 35–75 % RH represents a combination of the two previous DRH ranges, with non-uniform wetting occurring in most but not all realisations.

Finally, the assumption of a constant value for the DRH of 35 % RH will result in pit initiation for all realisations, with none of the pits stifling due to drying of the surface.

Efflorescence relative humidity

The efflorescence RH is not explicitly defined in the model, but is effectively defined by the minimum value of the DRH range.

3.2.4 Oxygen consumption time

As described in Section 2.3.4, the initially trapped O_2 in the buffer is consumed by a number of reactions, none of which are directly simulated in the model. In order to represent these various sinks in the model, the O_2 concentration is assumed to decrease exponentially with time (Equation 2-1), with the variability and uncertainty accounted for by sampling the value of the time constant a for each realisation.

The distribution of a values is defined based on an "O_2-consumption time" defined as the time required for consumption of 99.9 % of the original [O_2]. Based on a series of analyses of the rate of O_2 consumption in both full-scale *in situ* tests and laboratory experiments (SKB 2022b), the best-estimate for the range of O_2-consumption times is 1 week to 1 year. These bounding values correspond to a values of 360.4 yr^{-1} and 6.908 yr^{-1}, respectively. For the Monte Carlo simulations, the value of a was selected from a uniform distribution between these two bounding values. The choice of a uniform distribution places more weight on the shorter O_2-consumption times. Figure 3-8 shows distributions for a and for the O_2-consumption times based on 10 000 realisations.

As part of a sensitivity analysis, an alternative range of O_2-consumption times of 5 weeks to 5 years was also used. This range of O_2-consumption times corresponds to a range of a values of 72.084 yr^{-1} and 1.382 yr^{-1}, respectively, and is the same as that used for the saturated probabilistic pitting model (Briggs et al. 2020, 2021).
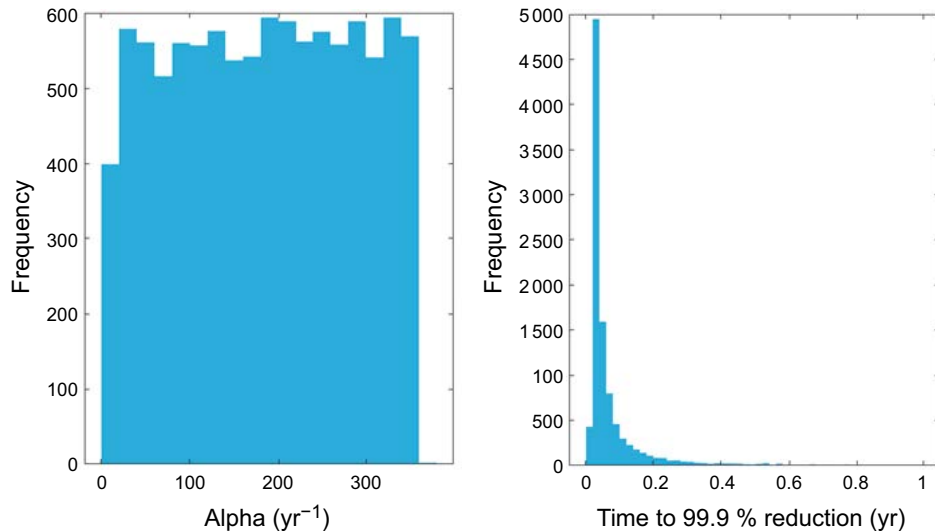
Figure 3-8. *Distribution of time constant a (left) and of the time required to reduce the O_2 concentration by 99.9 % (right) for 10 000 realisations based on a range of O_2-consumption times of 1 week to 1 year.*

3.2.5 Pit propagation kinetics

There is a lack of pit propagation kinetics for copper under atmospheric conditions. In the absence of more-relevant data, use is made of the pit growth data from the underground corrosion study of Denison and Romanoff (1950) for selected copper alloys and from selected soils.

Of the six "coppers" used in the Denison and Romanoff study, only data for "deoxidised copper" and "tough-pitch copper" are used, with various copper-silicon alloys (> 95 wt.% Cu) not considered. The deoxidised (99.94 % Cu, 0.18 % P) and tough-pitch (99.9 % Cu) coppers used by Denison and Romanoff are consistent with the modern alloy designations for phosphorous deoxidised high residual phosphorus copper (UNS C12200) and electrolytic tough-pitch copper (UNS C11000), respectively.

Of the fifteen soil types studied, only those with both good or fair drainage and a soil resistivity > 1 000 Ω cm were selected. Good drainage is taken as a surrogate for a soil that is both well-aerated and likely to be unsaturated, with a high soil resistivity also indicating a relatively dry soil condition (King et al. 2006). The three soils falling into this category were designated by the original authors as soil #53 (Cecil clay loam), soil #55 (Hagerstown loam), and soil #62 (Susquehanna clay). Soils exposures were conducted at ambient temperature, which likely falls in the range of 5–15 °C. These temperatures are lower than the initial canister temperatures and, therefore, could underestimate the effects of elevated temperature on O_2 diffusivity and pit growth kinetics. However, these data are used here in the absence of a more suitable dataset.

Maximum pit-depth measurements were made periodically on each of two samples of each alloy type for exposure times ranging from 2.0 yrs to 14.3 yrs. The minimum measurable pit depth was 6 mils (152 μm), with many of the measurements reported as being < 6 mils. Figure 3-9 shows the time-dependence of the maximum pit depth as a function of time (taken as the average of the two samples) for the two alloys and three soil types. Measurements below the detection limit (i.e., < 6 mils) are not shown.

The data shown in Figure 3-9 have been fitted to a log-log plot of the time dependence of the set of all measurable pit depths by linear regression, from which the time-dependent pit depth D can be expressed as:

$$D = At^n \tag{3-9}$$

where A = 159.2 μm and n = 0.112744. The fit to the log-log plot is poor (Figure 3-9(a)), with an R^2 value of 0.025. A consequence of the relatively small time exponent is that pits are predicted to grow rapidly initially, but then attain a relatively constant value (Figure 3-9(b)). This behaviour reflects that observed from the field tests.

Figure 3-9(b) also shows linear growth rate expressions based on the data of Ibrahim et al. (2018) shown in Figure 2-7 and the maximum localized penetration rate from Camitz and Vinka (2003) in a study of the corrosivity of Swedish soils. Ibrahim et al. (2018) did not observe discrete pits, but instead found thicker areas of corrosion in patches associated with condensed water droplets on the surface of copper coupons exposed to humid air. Based on the oxide thickness data shown in Figure 2-7, a maximum linear rate of corrosion of the underlying copper substrate of 5 μm/yr can be estimated. Camitz and Vinka (2003) studied the corrosion of copper in nine different Swedish soils for periods up to 7 years. The highest maximum localized penetration rate observed was 30 μm/yr in a sandy till soil which exhibited the highest resistivity (331 000 Ω cm), consistent with an unsaturated, well-aerated soil.

None of these datasets provide any information about the dependence of the pit growth rate on $[O_2]$, RH, or temperature, which are the three environmental parameters in the model.
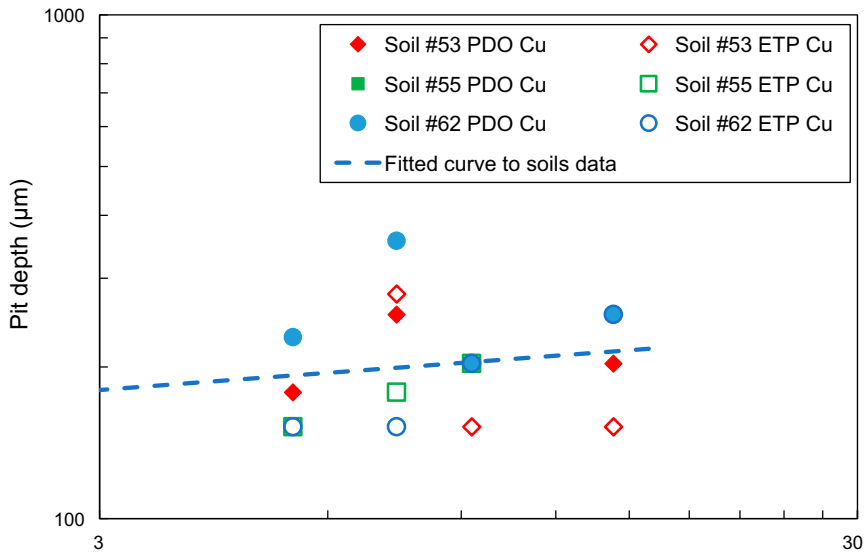
(a) log-log plot
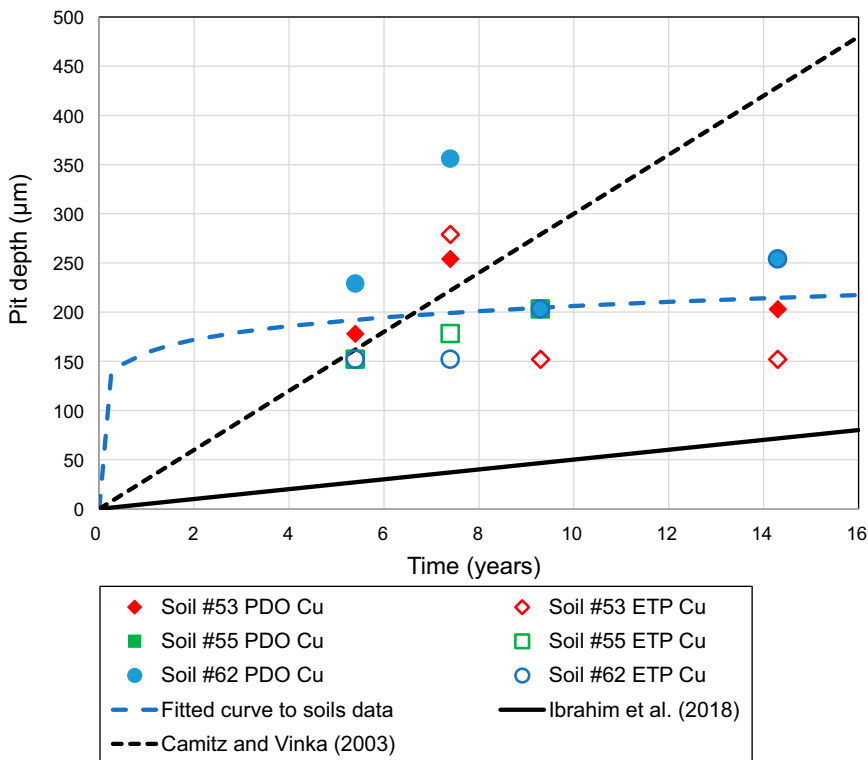
(b) Linear plot

Figure 3-9. *Alternative empirical pit growth rate expressions based on underground corrosion study of Denison and Romanoff (1950) (individual points and fitted curve on both (a) log-log and (b) linear plots), the soil corrosion study of Camitz and Vinka (2003) and the atmospheric corrosion study of Ibrahim et al. (2018) (on linear plot only).*

3.2.6 Pit stifling mechanisms

Various conceptual pit stifling mechanisms were discussed in detail in Section 2.3.4. Of the various proposed environmental and non-environmental mechanisms, only those associated with the drying of the surface (case 1(a)), the consumption of the initially trapped O_2 (case 1(b)), the decrease in C:A surface area ratio due to dilution of the droplet (case 1(d)), and the onset of uniform wetting of the surface (case 1(e)) are implemented here (Table 3-1). None of the non-environmental stifling mechanisms have been implemented for the analyses described in this report.

Surface dries out (stifling mechanism 1(a))

Following initial non-uniform wetting of the surface, the RH is compared with the DRH at each time step to determine whether the surface has dried out. For the current version of the code, the condition for drying of the surface is defined as

$$RH < DRH \tag{3-10}$$

Thus, the DRH serves not only as the condition for wetting, but also as the condition for drying of the surface. Although the ERH is typically less than the DRH, the presence of montmorillonite has been reported to increase the ERH in clay-salt mixtures (Ushijima et al. 2018) and preliminary experimental evidence has shown that surfaces can naturally dry out *at constant RH* due, it is believed, to the formation of a less-deliquescent corrosion product (Situm et al. 2024). Therefore, the use of the DRH to indicate both wetting and drying of the surface is appropriate for this preliminary modelling. The effect of an ERH less than the DRH, which would tend to delay the stifling of pitting and result in longer-lived and potentially deeper pits, can be explored in future modelling.

Table 3-1. Treatment of the various stifling mechanisms for the current analyses. Stifling mechanisms #1 relate to the redox-hydraulic-thermal evolution of the repository environment and stifling mechanisms #2 relate to non-environmental causes.

Stifling mechanism #	Stifling mechanism	Treatment for the current analyses
1(a)	Surface dries out	RH < DRH
1(b)	Consumption of O_2	Threshold $[O_2]$, $[O_2]_{thresh}$
1(c)	Decrease in O_2 supply due to water saturation	Not implemented
1(d)	Dilution of deliquesced electrolyte	Threshold RH, RH_{thresh}
1(e)	Uniform wetting of the surface	Threshold RH, RH_{SAT}
2(a)	Formation of less-catalytic cathode	Not implemented
2(b)	Blocked cathode	Not implemented
2(c)	Lateral spread of anodic reaction	Not implemented
2(d)	Droplet coalescence	Not implemented
2(e)	iR drop in thin electrolyte layer	Not implemented
2(f)	iR drop due to precipitation within droplet	Not implemented
2(g)	Loss of critical pit chemistry	Not implemented

Uniform wetting of the surface (stifling mechanism 1(e))

The threshold RH for uniform wetting of the surface RH_{SAT} is sampled for each realisation from a uniform distribution of between 95 % and 100 % RH.

The range is set to relatively high values of the RH based on the evidence of Chen et al. (2004) that the adsorbed water layer thickness remains non-uniform even at 95 % RH, even though the entire surface may be wetted to some degree.

Dilution of deliquesced electrolyte (stifling mechanism 1(d))

The threshold RH for stifling due to dilution of the electrolyte RH_{thresh} is sampled for each realisation from a uniform distribution of between 99 % and 100 % RH.

The range for dilution of the electrolyte is set so high based on the deliquescence behaviour shown in Figure 2-11. At 99 % RH, the equilibrium concentration of dissolved NaCl is approximately 0.3 mol/L. Based on the analysis in Section 2.3.4, such a dilution would result in a decrease in C:A surface area ratio by a factor of 2–3 from the ratio at 80 % RH.

Based on the logic in the environmental flow chart (Figure 3-2), the criterion for uniform wetting of the surface is assessed prior to the criterion for dilution. Given the respective ranges of RH for the two phenomena, a pit would only stifle due to dilution of the electrolyte if the sampled RH_{SAT} also exceeds 99 % RH.

Consumption of O_2 (stifling mechanism 1(b))

The existence of a minimum $[O_2]$ below which pit growth cannot be sustained is based on the concept that a minimum rate of dissolution is required to maintain a critical pit environment. Such a concept has not yet been demonstrated for the atmospheric corrosion of copper and, for this reason, the existence of, and the value for, $[O_2]_{thresh}$ are uncertain. Therefore, a sensitivity study has been performed assuming various ranges for $[O_2]_{thresh}$ as follows:

- 10–30 % of the initial $[O_2]$
- 5–20 % of the initial $[O_2]$
- 1–10 % of the initial $[O_2]$
- 0.1–1 % of the initial $[O_2]$
- 0.01–0.1 % of the initial $[O_2]$
- 0 %

For each of the first five ranges, a value of $[O_2]_{thresh}$ was selected for each realisation based on the assumption of a uniform distribution between the upper and lower bounds. The last of the six ranges (i.e., 0 %) was used to examine the effect of stifling due to an increase in RH alone, with no limitation based on the availability of O_2.

3.3 Software, hardware, and code implementation

3.3.1 Software

The PUP code was developed using the MathWorks MATLAB software package. MathWorks MATLAB is a commercial numerical computing tool for mathematical calculations, such as matrix manipulations, linear algebra and statistical analysis (among many other applications). The MATLAB software and associated toolboxes provide a platform of mathematical calculations based on the well-accepted mathematical libraries known as LAPACK and other algorithms from the literature. They allow users to develop their own calculation programs within this platform. MATLAB has been under development since 1984 by MathWorks. It is widely used in industry and academia. It is being actively developed and maintained.

Development was completed using MATLAB version R2022b including the Statistics and Machine Learning Toolbox. Built-in MATLAB mathematical algorithms were used for most calculations, for example data input, vector operations, interpolation, random number generation, data output and data visualisation. The statistical methods also used built-in functions including creating probability distribution and cumulative distribution functions using the Statistics and Machine Learning Toolbox.

3.3.2 Hardware

The software was developed and run on a workstation computer with Intel Xeon processors (total of 36 cores) and 384 GB of error catching and correcting (ECC) memory. Wherever possible the code was developed to be parallel by design, using built-in MATLAB vector operations and running the Monte Carlo (MC) realisations in parallel. When running the largest models (1 million MC realisations) the simulation can take 30 minutes and take upwards of 64 GB of memory. For rapid development of the model, smaller MC simulations can be run in much less time.

3.3.3 Code implementation

During the implementation of the PUP, the code was developed as described by the conceptual model in Section 3.1 but separated into three components. The first component is responsible for initialization of parameters and input data; for example, physical parameters for temperature, RH, specified DRH, $[O_2]$ thresholds, etc as well as numerical parameters for the number of Monte Carlo realisations and time stepping. To allow for the possibility of short-lived pits, the timesteps are chosen with increased discretization at early time compared to late time. Specifically, one hundred timesteps for each order of magnitude between 10^{-5} years and 100 000 years. In this first component of the code, figures are produced to represent the environment being modelled (Section 3.2).

The second component of the model is the main compute loop which determines the outcome for each Monte Carlo realisation at each timestep. During initial development, this component was based on typical branching loops to account for the varying conditions specified by the conceptual model in Section 3.1. Initial trials were successful, but 1 million realisations took over a week of computation on a workstation with 36 cores. Development, testing and validation continued during which time optimization of the code was also prioritized. Optimizations were implemented to take advantage of vector capable operations on modern processors. With this capability, mathematical manipulations on a vector, or one-dimensional array, are as fast as a single calculation due to the ability of a processor to pack multiple operations into a single clock cycle. MATLAB handles the abstraction and optimization of the vector operators on the CPU requiring only a single line of code to specify an operation be completed on all realisations.

A secondary optimization was also implemented; instead of checking the environmental state at each timestep for each condition, including wetting, pitting and stifling environment, the code continually narrows the data set to the conditions of interest and minimizes vector size and calculation requirements. For example, when checking if the surface is wet, the code will throw out all timesteps where the surface is dry as this data is not needed, drastically reducing array size. Similar choices are made for each environmental condition and pitting is only calculated for the small subset of realisations and timesteps where it occurs.

The third component of the model is the results and output section of the code. Due to the choices made during optimization, namely the narrowing down of data, results like those shown in Figure 4-1 only indicate the first reason why pitting did not occur as the other environmental conditions are not tested. All results are also output to a comma separated files for further analysis.

4 Results of probabilistic pitting analyses

The conditions for the five sets of sensitivity analyses described here are summarised in Table 4-1.

Table 4-1. Summary of the ranges of conditions used for the various senstivity analyses.

O₂.consumption time	DRH	[O₂]thresh	Results
1 week – 1 year	55–75 % RH	In all cases, 10–30 %, 5–20 %, 1–10 %, 0.1–1 %, and 0.01–0.1 % of the initial value, as well as 0 % O₂	Table 4-2
	35–60 % RH		Table 4-3
5 weeks – 5 years	55–75 % RH		Table 4-4
	35–75 % RH		Table 4-5
	35 % RH		Table 4-6

In all cases, RH_{SAT} was sampled from a uniform distribution of 95–100 % RH and RH_{thresh} from a uniform distribution of 99–100 % RH.

Table 4-2 to Table 4-6 show the results of the sensitivity analyses performed using the PUP model. These analyses were designed to investigate the extent to which the evolution of the near-field environment stifles pit growth under unsaturated conditions. Particular attention has been paid to the evolution of the degree of buffer saturation and of the redox conditions and the associated stifling mechanisms.

4.1 O₂-consumption time 1 week to 1 year, DRH 55–75 % RH

The results from the PUP simulations for an O_2-consumption time of 1 week to 1 year and a DRH range of 55–75 % RH are discussed here as an example of the predictions from the model. A summary of the results for various $[O_2]_{thresh}$ ranges is given in Table 4-2, including (i) the numbers of realisations in which the criteria for each of the three stifling mechanisms (and the requirement for a non-uniformly wetted surface) were met for at least one time step, (ii) the number of realisations in which a pit was initiated, (iii) the mean, standard deviation, maximum, and minimum pit ages, and (iv) various statistics regarding the predicted pit depth based on the Denison and Romanoff expression (Equation (3-9)). One million realisations were performed for each simulation, with each realisation terminated after 100 000 years. No realisation was terminated at an earlier time due to penetration of the corrosion allowance.

In terms of the various environmental pre-requisite and stifling criteria:

- The canister surface was predicted to be dry for at least one time step in 100 % of the realisations because the minimum RH of 47 % in Figure 3-7 is less than the minimum DRH of 55 % RH.

- Although the canister surface was predicted to eventually become uniformly wetted in 98.9 % of the realisations, there are a small number of realisations in which the selected RH_{thresh} was less than the RH for uniform wetting.

- In approximately 9.8 % of the realisations, the deliquesced solution was assessed to be too dilute to support pitting. This relatively small fraction is a consequence of (a) the assumed range for RH_{thresh} of 99–100 % RH and (b) the possibility of pit stifling due to uniform wetting is assessed prior to this dilution mechanism (see the logic sequence in the environment flow chart in Figure 3-2).

- Except for the simulation in which pits were not stifled by the availability of O_2 ($[O_2]_{thresh} = 0$ %), pits were predicted to be stifled at some stage in 100 % of the realisations. (An O_2 threshold of 0 % makes no mechanistic sense since corrosion of any form will not proceed in the absence of O_2. The $[O_2]_{thresh} = 0$ % simulation was performed simply to check the code and to assess the relative importance of the other stifling mechanisms. The absence of a lower bound $[O_2]$ also results in pit re-initiation when a pit previously stifled because the surface dried out re-initiates because of re-wetting. This scenario can then lead to maximum pit depths that exceed the maximum depth predicted for a single pit using Equation (3-9) and a pit age of 100 000 yr).

Table 4-2. Predicted pit characteristics for a range of O$_2$-consumption times of 1 week to 1 year and a deliquescence relative humidity range of 55–75 %. Pit depths based on expression for the Denison and Romanoff soils data.

DRH	55–75 %					
[O$_2$]$_{thresh}$ (% of initial value)	10–30 %	5–20 %	1–10 %	0.1–1 %	0.01–0.1 %	0 %
# realisations with dry surface events	1 000 000	1 000 000	1 000 000	1 000 000	1 000 000	1 000 000
# realisations with uniformly wetted events	988 894	988 894	988 894	988 894	988 894	988 894
# realisations in which RH > RH$_{THRESH}$	97 864	97 864	97 864	97 864	97 864	97 864
# realisations where surface is wet, but insufficient O$_2$	1 000 000	1 000 000	1 000 000	1 000 000	1 000 000	0
Number of realisations with pits	799 976	799 976	799 976	799 976	799 976	1 000 000
Average age (yrs)	0.01666	0.02089	0.02787	0.04294	0.05518	4 155
St dev pit age (yrs)	0.02266	0.02715	0.03333	0.04266	0.0481	8 015
Max. pit age (yrs)	0.3162	0.3467	0.3467	0.3467	0.3467	99 969
Min. pit age (yrs)	3.802×10^{-5}	3.802×10^{-5}	3.802×10^{-5}	3.802×10^{-5}	3.802×10^{-5}	5.973
Number of realisations Pit Depth > 100 µm	208 966	275 545	397 978	698 191	777 843	1 000 000
Number of realisations Pit Depth > 1 mm	0	0	0	0	0	0
Max Pit Depth (mm)	0.140	0.141	0.141	0.141	0.141	0.724
Mean Pit Depth (mm)	0.0960	0.0987	0.102	0.108	0.112	0.479
Pit Depth Standard Deviation (mm)	0.00924	0.0093	0.00933	0.00903	0.00883	0.0721

Table 4-3. Predicted pit characteristics for a range of O$_2$-consumption times of 1 week to 1 year and a deliquescence relative humidity range of 35–60 %. Pit depths based on expression for the Denison and Romanoff soils data.

DRH	35–60 %					
[O$_2$]$_{thresh}$ (% of initial value)	10–30 %	5–20 %	1–10 %	0.1–1 %	0.01–0.1 %	0 %
# realisations with dry surface events	499 790	499 790	499 790	499 790	499 790	499 790
# realisations with uniformly wetted events	988 894	988 894	988 894	988 894	988 894	988 894
# realisations in which RH > RH$_{THRESH}$	97 864	97 864	97 864	97 864	97 864	97 864
# realisations where surface is wet, but insufficient O$_2$	1 000 000	1 000 000	1 000 000	1 000 000	1 000 000	0
Number of realisations with pits	1 000 000	1 000 000	1 000 000	1 000 000	1 000 000	1 000 000
Average age (yrs)	0.01825	0.02365	0.03337	0.05743	0.0804	4 230
St dev pit age (yrs)	0.02776	0.03572	0.04986	0.08167	0.1112	8 027
Max. pit age (yrs)	0.3311	0.4266	0.6457	0.9772	1.318	100 000
Min. pit age (yrs)	0.00331	0.00447	0.00631	0.01259	0.01905	10.4
Number of realisations Pit Depth > 100 µm	268 529	354 442	511 264	897 629	1 000 000	1 000 000
Number of realisations Pit Depth > 1 mm	0	0	0	0	0	0
Max Pit Depth (mm)	0.141	0.145	0.152	0.159	0.164	0.758
Mean Pit Depth (mm)	0.0964	0.0993	0.103	0.110	0.115	0.453
Pit Depth Standard Deviation (mm)	0.00978	0.0100	0.0104	0.0108	0.011	0.0877

Table 4-4. Predicted pit characteristics for a range of O₂-consumption times of 5 weeks to 5 years and a deliquescence relative humidity range of 55–75 %. Pit depths based on expression for the Denison and Romanoff soils data.

DRH	55–75 %					
$[O_2]_{thresh}$ (% of initial value)	10–30 %	5–20 %	1–10 %	0.1–1 %	0.01–0.1 %	0 %
# realisations with dry surface events	1 000 000	1 000 000	1 000 000	1 000 000	1 000 000	1 000 000
# realisations with uniformly wetted events	988 894	988 894	988 894	988 894	988 894	988 894
# realisations in which RH > RH_{THRESH}	97 864	97 864	97 864	97 864	97 864	97 864
# realisations where surface is wet, but insufficient O₂	1 000 000	1 000 000	1 000 000	1 000 000	1 000 000	0
Number of realisations with pits	799 976	799 976	799 976	799 976	799 976	1 000 000
Average age (yrs)	0.05783	0.06834	0.08379	0.1111	0.1272	4 155
St dev pit age (yrs)	0.04947	0.05312	0.05779	0.0651	0.0714	8 014
Max. pit age (yrs)	0.3467	0.3467	0.3467	0.3467	0.3467	99 969
Min. pit age (yrs)	3.802×10^{-5}	3.802×10^{-5}	3.802×10^{-5}	3.802×10^{-5}	3.802×10^{-5}	5.97
Number of realisations Pit Depth > 100 µm	777 843	777 843	777 843	777 843	777 843	1 000 000
Number of realisations Pit Depth > 1 mm	0	0	0	0	0	0
Max Pit Depth (mm)	0.141	0.141	0.141	0.141	0.141	0.724
Mean Pit Depth (mm)	0.112	0.115	0.118	0.122	0.124	0.479
Pit Depth Standard Deviation (mm)	0.0090	0.0089	0.0089	0.0093	0.0099	0.0721

Table 4-5. Predicted pit characteristics for a range of O₂-consumption times of 5 weeks to 5 years and a deliquescence relative humidity range of 35–75 %. Pit depths based on expression for the Denison and Romanoff soils data.

DRH	35–75 %					
$[O_2]_{thresh}$ (% of initial value)	10–30 %	5–20 %	1–10 %	0.1–1 %	0.01–0.1 %	0 %
# realisations with dry surface events	687 174	687 174	687 174	687 174	687 174	687 174
# realisations with uniformly wetted events	988 894	988 894	988 894	988 894	988 894	988 894
# realisations in which RH > RH_{THRESH}	97 864	97 864	97 864	97 864	97 864	97 864
# realisations where surface is wet, but insufficient O₂	1 000 000	1 000 000	1 000 000	1 000 000	1 000 000	0
Number of realisations with pits	900 143	900 143	900 143	900 143	900 143	1 000 000
Average age (yrs)	0.07543	0.09415	0.1259	0.1989	0.2640	4 203
St dev pit age (yrs)	0.1043	0.1303	0.1782	0.2946	0.4137	8 029
Max. pit age (yrs)	1.622	2.138	3.236	4.898	6.607	100 000
Min. pit age (yrs)	1.259×10^{-5}	1.259×10^{-5}	1.259×10^{-5}	1.259×10^{-5}	1.259×10^{-5}	8.5
Number of realisations Pit Depth > 100 µm	889 079	889 079	889 079	889 079	889 079	1 000 000
Number of realisations Pit Depth > 1 mm	0	0	0	0	0	0
Max Pit Depth (mm)	0.168	0.173	0.182	0.344	0.358	0.757
Mean Pit Depth (mm)	0.114	0.117	0.121	0.127	0.131	0.458
Pit Depth Standard Deviation (mm)	0.0106	0.0108	0.0112	0.0121	0.0133	0.0832

Table 4-6. Predicted pit characteristics for a range of O$_2$-consumption times of 5 weeks to 5 years and a deliquescence relative humidity of 35 %. Pit depths based on expression for the Denison and Romanoff soils data.

DRH	35 %					
[O$_2$]$_{thresh}$ (% of initial value)	10–30 %	5–20 %	1–10 %	0.1–1 %	0.01–0.1 %	0 %
# realisations with dry surface events	0	0	0	0	0	0
# realisations with uniformly wetted events	988 894	988 894	988 894	988 894	988 894	988 894
# realisations in which RH > RH$_{THRESH}$	97 864	97 864	97 864	97 864	97 864	97 864
# realisations where surface is wet, but insufficient O$_2$	1 000 000	1 000 000	1 000 000	1 000 000	1 000 000	0
Number of realisations with pits	1 000 000	1 000 000	1 000 000	1 000 000	1 000 000	1 000 000
Average age (yrs)	0.09131	0.1185	0.1681	0.2951	0.4221	4 243
St dev pit age (yrs)	0.1391	0.1802	0.2566	0.4425	0.6301	8 027
Max. pit age (yrs)	1.622	2.138	3.236	4.898	6.607	100 000
Min. pit age (yrs)	0.0166	0.02188	0.03162	0.0631	0.0955	24
Number of realisations Pit Depth > 100 µm	1 000 000	1 000 000	1 000 000	1 000 000	1 000 000	1 000 000
Number of realisations Pit Depth > 1 mm	0	0	0	0	0	0
Max Pit Depth (mm)	0.168	0.173	0.182	0.190	0.197	0.583
Mean Pit Depth (mm)	0.116	0.119	0.124	0.132	0.138	0.381
Pit Depth Standard Deviation (mm)	0.0117	0.0121	0.0126	0.0132	0.0137	0.0487

Pits were not predicted to initiate in every realisation. The initial RH in the buffer is 71 % for all of the profiles (Figure 3-7). Because this value is $^4/_5^{th}$ along the DRH range of 55–75 % RH, pits are predicted to initiate in only 80 % of the realisations based on the requirement for non-uniform wetting of the surface (Table 4-2). In fact, pit initiation is predicted to consistently occur in 799 976 of the one million realisations, which suggests that even with such a large sample size the selection of the RH profiles is not entirely random (although consistently so). The one exception to the 80 % occurrence of pitting is the simulation where the availability of O$_2$ is not limiting. In this case, the approximately 20 % of simulations in which pits do not initiate immediately (i.e., those with sampled DRH values of 71–75 % RH) do subsequently predict pit initiation during the wetting stage as the RH at the canister surface increases (Figure 3-7). This also indicates that if the availability of O$_2$ does limit pit propagation, as is reasonable to assume, pit initiation only occurs during the initial drying phase since there is insufficient O$_2$ remaining during the wetting phase.

Figure 4-1 shows the predicted time dependence of the number of realisations with active pitting and of the various environmental stifling mechanisms for a simulation with an assumed [O$_2$]$_{thresh}$ range of 10–30 % of the initial O$_2$ concentration (O$_2$-consumption time 1 week to 1 year, DRH range 55–75 % RH). As noted above, pit initiation occurs immediately in 80 % of the realisations (pink curve in Figure 4-1), with the majority of pits propagating for 0.003–0.004 years (1.1–1.5 days) before stifling. (In fact, the earliest stifling event occurs after 3.8×10^{-5} years (20 minutes), Table 4-2). Apart from the approximately 20 % of realisations in which pits do not initiate because the surface does not wet initially (black curve in Figure 4-1), the mechanism responsible for this early stifling of pits is the lack of sufficient O$_2$ (blue curve, Figure 4-1). After approximately 0.01–0.02 years (3.7–7.3 days), pit stifling begins to occur because the surface dries out as the sampled DRH drops below the decreasing RH at the canister surface during the drying phase. The number of pits stifling due to the lack of O$_2$ reaches a maximum after 0.03–0.04 years (11–15 days), after which the drying of the surface becomes increasingly responsible for pit stifling and becomes the predominant mechanism for times longer than 0.1 year (37 days). After 0.3–0.4 years, virtually all of the pits stifle because the surface is too dry. This interval corresponds to the maximum pit age of 0.3162 years (Table 4-2), at which time the surface RH is predicted to be 55.8 % (based on the expression for the drying phase in Equation (3-5)).

Based on the collection of one hundred RH profiles in Figure 3-7, the minimum surface RH of 47 % is achieved after 2–10 years. As the surface RH increases, non-uniform wetting occurs once again and the number of realisations in which this is the primary criterion for the absence of pits (black curve in Figure 4-1) decreases. This does not mean that pits re-initiate because there is still insufficient O$_2$ to support pit growth and this becomes the predominant cause for the absence of pits (blue curve in Figure 4-1). In fact, in none of the 1 million realisations is a pit predicted to re-initiate as the surface re-wets.

At times longer than 100 years, uniform wetting of the surface is predicted to become an increasingly frequent reason for the stifling of pits (red curve, Figure 4-1). However, this in part is a consequence of the logic sequence in which the code assesses whether pitting is possible or whether it stifles at each time step, namely:

- Is the surface non-uniformly wetted (RH $\geq$ DRH)?
- Is the surface uniformly wetted (RH $\geq$ RH$_{SAT}$)?
- Is the deliquesced solution too dilute (RH $\geq$ RH$_{thesh}$)?
- Is there sufficient O$_2$ ([O$_2$] $\geq$ [O$_2$]$_{thresh}$)?

At these long times, pit stifling would occur both because the surface is uniformly wetted and because there is insufficient O$_2$, but the code identifies uniform wetting as the "first" mechanism that leads to stifling.

Based on the assumed RH profiles and the existence of an [O$_2$] threshold, the predicted ages of pits are relatively short (Table 4-2). Since the availability of O$_2$ is the most important stifling mechanism initially, the average age of pits increases with decreasing [O$_2$]$_{thresh}$, from 0.0167 years (6.1 days) for a [O$_2$]$_{thresh}$ range of 10–30 % of the initial concentration to 0.0552 years (20 days) for a [O$_2$]$_{thresh}$ range of 0.01–0.1 % of the initial value. The maximum pit age increases from 0.316 years (115 days) to 0.347 years (127 days), respectively, for the same [O$_2$]$_{thresh}$ ranges, although the maximum pit age is less sensitive to the value of [O$_2$]$_{thresh}$ than the average pit depth because the oldest pits tend to stifle because the surface dries out. In fact, the maximum pit age of 0.347 years for the majority of [O$_2$]$_{thresh}$ ranges (Table 4-2) corresponds to the time at which the RH reaches 55 % (based on Equation (3-5)), corresponding to the lower bound of the DRH range. If the availability of O$_2$ does not stifle pit growth (i.e., [O$_2$]$_{thresh}$ = 0 %), at least one pit is predicted to grow for almost the entire 100 000 year simulation period (maximum pit age 99 969 years).
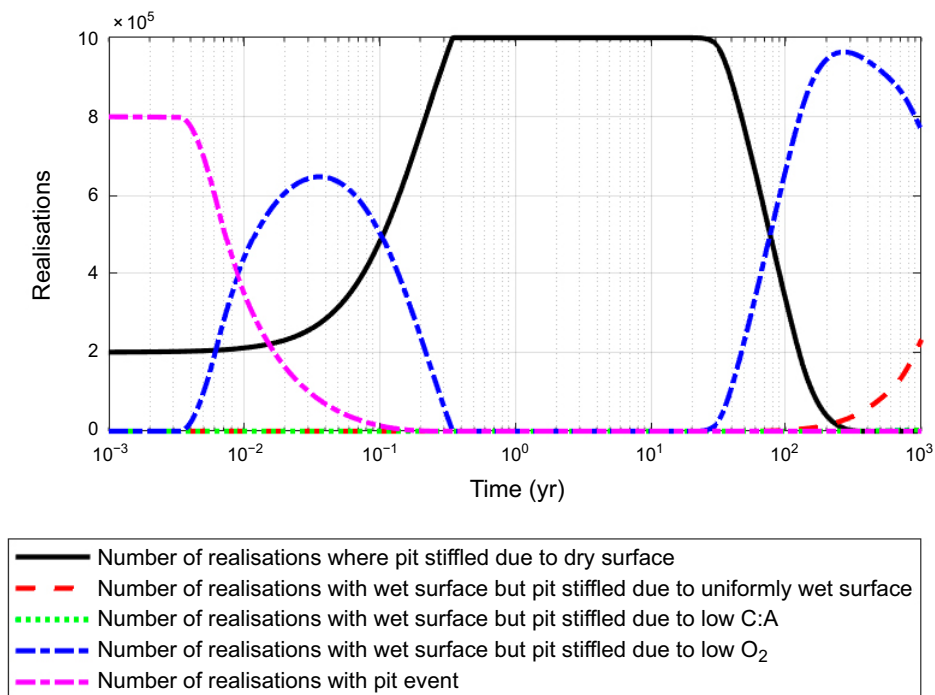
Figure 4-1. *Time dependence of the number of realisations with actively growing pits and in which the various environmental pit stifling criteria are met. Simulation shown for an overall O$_2$-consumption time of 1 week to 1 year, DRH range of 55–75 % RH, and [O$_2$]$_{thresh}$ of 10–30 % of the initial O$_2$ concentration, and times from 10^{-5} years to 10^3 years.*

Figure 4-2 shows the distribution and cumulative distribution of pit ages for the simulation with an $[O_2]_{thresh}$ range of 10–30 % of the initial concentration (O_2-consumption time of 1 week to 1 year, DRH range 55–75 % RH). The distribution of pit ages is skewed, with the median age being 0.00871 years (3.2 days), compared with an average age of 0.0167 years (6.1 days) and a maximum age of 0.316 years (115 days). Comparison with the RH profiles in Figure 3-7 confirms that pitting occurs during the initial drying phase of the near-field environment.
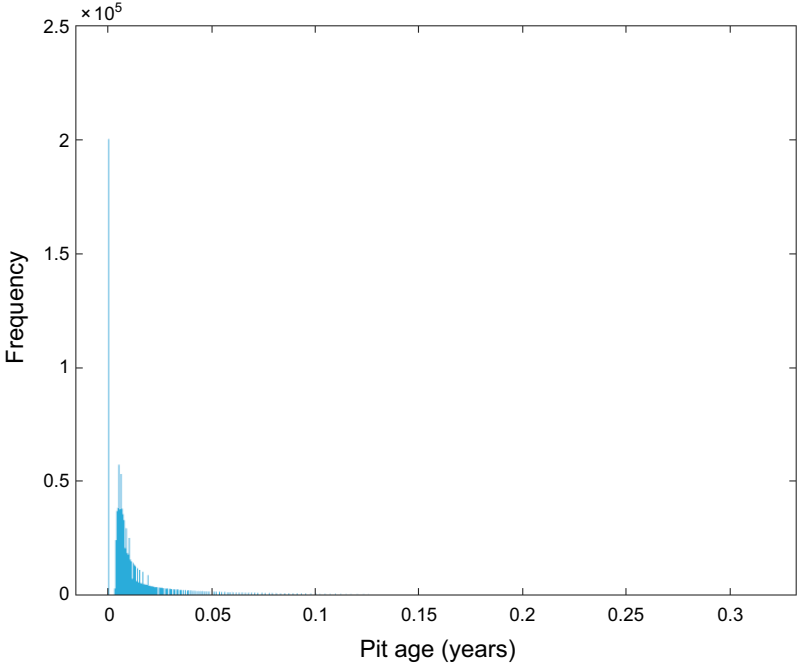
(a) Distribution of pit ages
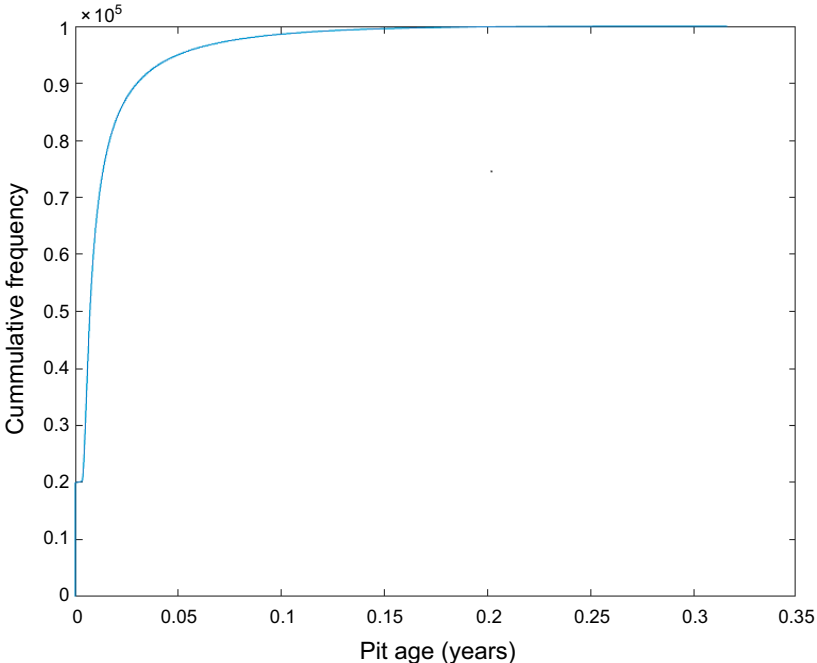
(b) Cumulative distribution of pit ages

Figure 4-2. *Predicted pits ages for a simulation with an overall O_2-consumption time of 1 week to 1 year, DRH range of 55–75 % RH, and $[O_2]_{thresh}$ of 10–30 % of the initial O_2 concentration, a) probability distribution, b) cumulative distribution.*

An important conclusion from these analyses is that the nature of the near-field environment and how it evolves with time does not support long-lived pits under unsaturated conditions.

Table 4-2 also provides information about the distributions of pit sizes based on the pit growth expression from the Denison and Romanoff soils study illustrated in Figure 3-9. Each realisation predicts the growth of a single pit, provided the surface is non-uniformly wetted leading to pit initiation. In none of the simulations (comprising 1 million individual realisations), did the predicted pit depth exceed 1 mm. Indeed, for simulations in which the availability of O_2 was assumed to stifle pit growth, the maximum predicted pit depth was 0.141 mm. The number of pits exceeding 100 μm increased with decreasing $[O_2]_{thresh}$, ranging from 208 966 (representing 26.1 % of the total number of pits) for $[O_2]_{thresh}$ = 10–30 % of the initial O_2 concentration to 777 843 (97.2 % of the total) for $[O_2]_{thresh}$ = 0.01–0.1 %. The depth of 100 μm is typical of that observed from large-scale *in situ* experiments and is used as an allowance for localised corrosion under aerobic conditions (SKB 2022c). If the availability of O_2 is assumed not to limit pit growth then all realisations result in pitting and all of those pits exceed 100 μm in depth, with the maximum pit depth predicted to be 0.72 mm. However, as noted above, such predictions have no technical basis since O_2 is required for pit propagation.

The alternative "pit" growth expressions of Ibrahim et al. (2018) and Camitz and Vinka (2003) are based on constant propagation rates of 5 μm/yr and 30 μm/yr, respectively (Figure 3-9). If those rates are applied to the maximum pit ages in Table 4-2, the maximum predicted depth ranges from 1.6 μm to 1.7 μm and 8.0 μm to 8.5 μm, respectively, for the various ranges of $[O_2]_{thresh}$ considered.

4.2 O_2-consumption time 1 week to 1 year, DRH 35–60 % RH

Table 4-3 provides a summary of the results of the simulations for the various $[O_2]_{thresh}$ ranges for an overall O_2-consumption time of 1 week to 1 year, but with a DRH range of 35–60 %. There are some similarities and some differences with the behaviour predicted for a DRH range of 55–75 % RH (Section 4.1).

Because the maximum value of the DRH range is less than the initial value in the buffer of 71 % RH, the surface is deemed to be non-uniformly wetted at some stage in every realisation. Because the surface is non-uniformly wetted from the outset when there is still sufficient O_2 to support pit growth, pitting occurs in 100 % of the realisations, compared with approximately 80 % of the realisations for the DRH range of 55–75 % RH (cf. Table 4-2). In fact, for those realisations in which the selected DRH is lower than the minimum RH of approximately 47 % (Figure 3-7), the surface is predicted to never dry out, with drying occurring in only approximately 50 % of the realisations (Table 4-3). The numbers of realisations in which the surface is either uniformly wetted, too dilute, or in which there is insufficient O_2 to support pit growth (all for at least one time step) are the same as those for the higher DRH range.

The fact that pits initiate and grow in all realisations leads to slightly longer-lived pits, with the minimum, maximum, and average pit ages all increasing with decreasing $[O_2]$ threshold, as above.

Figure 4-3 shows the time dependence of the stifling mechanisms for the simulations with a DRH range of 35–60 % for comparison with that for the higher DRH range in Figure 4-1. Compared with the results for the higher DRH range, it can be seen that all realisations result in pitting initially and that stifling because of drying of the surface only affects approximately 50 % of the runs. Stifling due to insufficient O_2 is a more important mechanism if the surface is less likely to dry out.
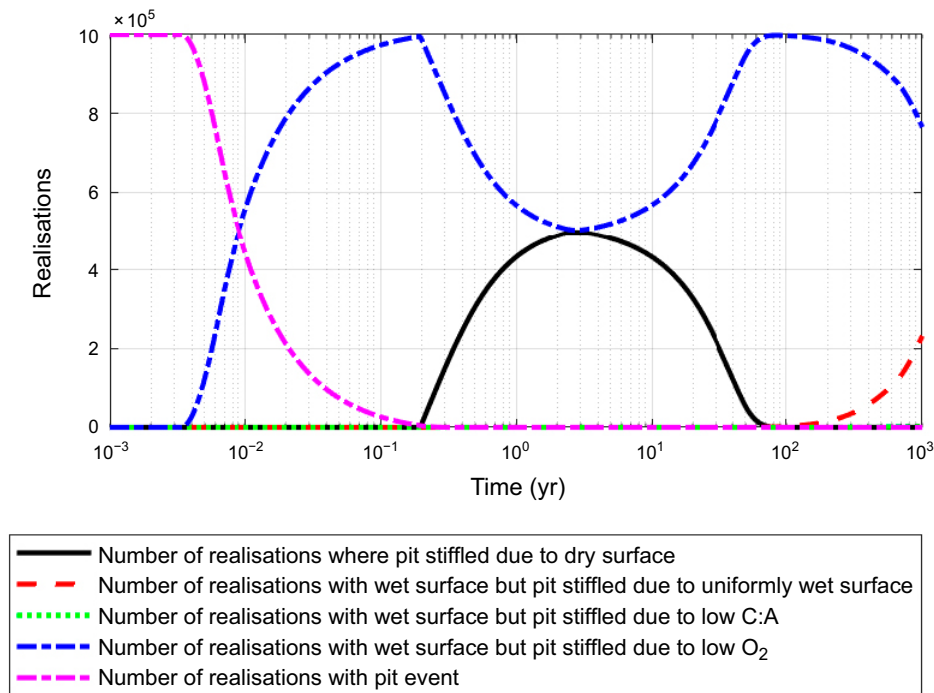
Figure 4-3. *Time dependence of the number of realisations with actively growing pits and in which the various environmental pit stifling criteria are met. Simulation shown for an overall O_2-consumption time of 1 week to 1 year, DRH range of 35–60 % RH, and $[O_2]_{thresh}$ of 10–30 % of the initial O_2 concentration and for times of 10^{-3} years to 10^3 years.*

4.3 Effect of [O_2] threshold

Figure 4-4 shows the effect of the [O_2] threshold range on the time dependence of the number of pitting events and on the different stifling mechanisms for an overall O_2-consumption time of 1 week to 1 year and a DRH range of 55–75 % RH. All simulations exhibit the same behaviour initially, with pit initiation and growth in approximately 80 % of the realisations. However, the extent to which the availability of O_2 limits pit propagation (the blue dashed curve) decreases with decreasing $[O_2]_{thresh}$ range, with the height of the early peak decreasing and shifting to later times. The $[O_2]_{thresh}$ range does not affect the time dependence or the number of realisations in which pits stifles because the surface dries out (black solid curve). The second peak in the number of pits stifling due to O_2 exhaustion that appears after approximately 20 years is because the RH is such that the surface is non-uniformly wetted and the electrolyte is not sufficiently diluted to cause stifling. For an $[O_2]_{thresh} = 0$ % (Figure 4-4(f)), the availability of O_2 is never limiting, and pit stifling only occurs because either the surface dries out (at earlier times) or becomes uniformly wetted (at longer times).
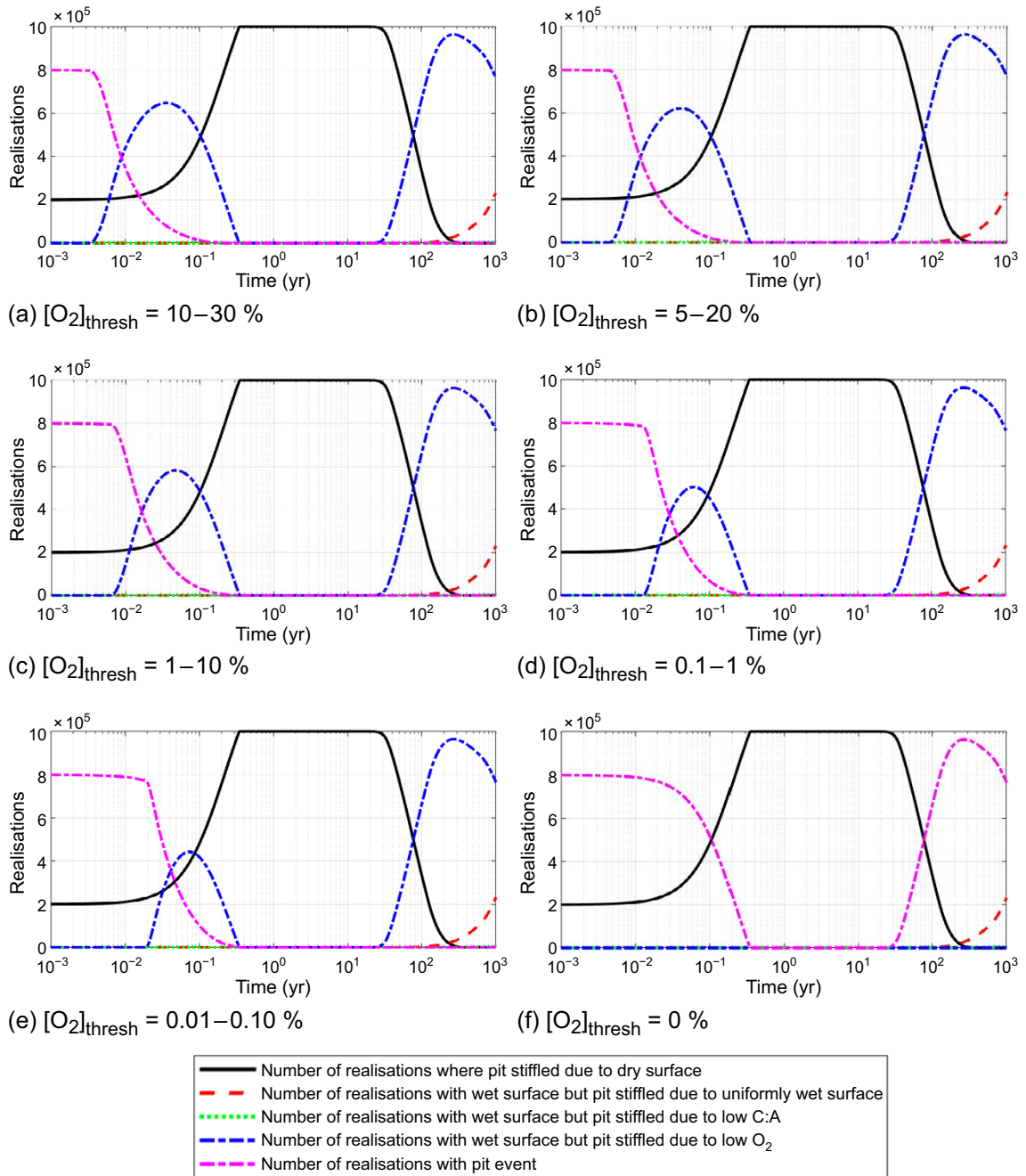
Figure 4-4. *Effect of threshold [O_2] range on the time dependence of the number of realisations with actively growing pits and of various environmental pit stifling criteria. Simulations shown for an overall O_2-consumption time of 1 week to 1 year, DRH range of 55–75 % RH, and for times of 10^{-3} years to 10^3 years.*

In general, the pit ages and depths increase with decreasing threshold $[O_2]$ (Table 4-2 to Table 4-3). Figure 4-5 shows the dependence of the average pit age on the $[O_2]_{thresh}$ range. The average pit age progressively increases with decreasing $[O_2]_{thresh}$ if there is a finite threshold value (Figure 4-5(b)), but is much greater if O_2 is not limiting ($[O_2]_{thresh} = 0$ %, Figure 4-5(a)). Clearly, provided there is a finite $[O_2]$ below which pits growth cannot be sustained, then the pit lifetimes are limited given the expected evolution of redox and RH conditions in the near-field.

In contrast to the trend of increasing average pit age with decreasing $[O_2]_{thresh}$ range, the maximum pit age is relatively insensitive to the $[O_2]$ threshold (Figure 4-6). This insensitivity is because the longest-lived pits stifle because the surface dries our rather than because of a lack of O_2. This can be seen from Figure 4-4 where the primary stifling mechanism changes from O_2-limitation (blue dashed curve) to drying of the surface (black curve) at times greater than approximately 0.1 year.
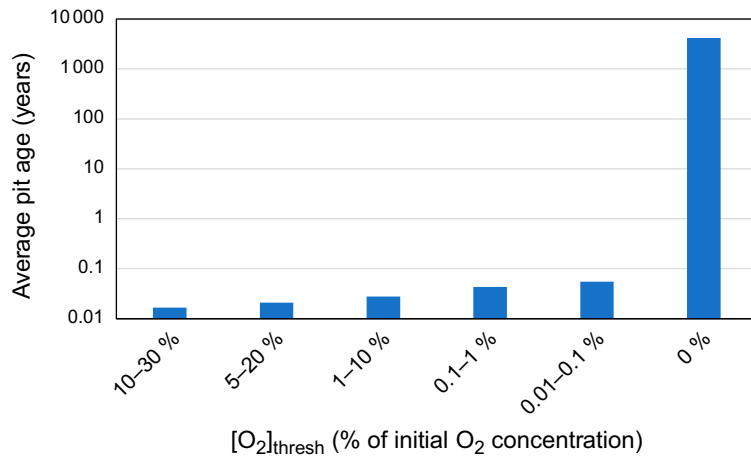
(a) All $[O_2]_{thresh}$ ranges, logarithmic pit age axis
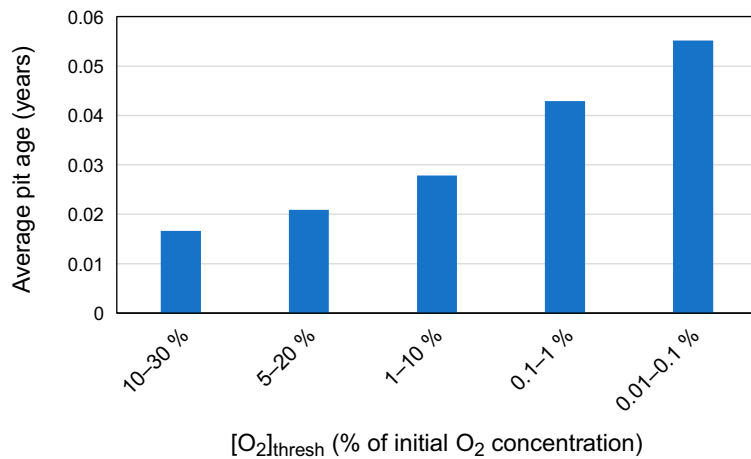
(b) Finite $[O_2]_{thresh}$ ranges, linear pit age axis

Figure 4-5. *Effect of threshold $[O_2]$ range on the average pit age. Simulations shown for an overall O_2-consumption time of 1 week to 1 year, DRH range of 55–75 % RH.*
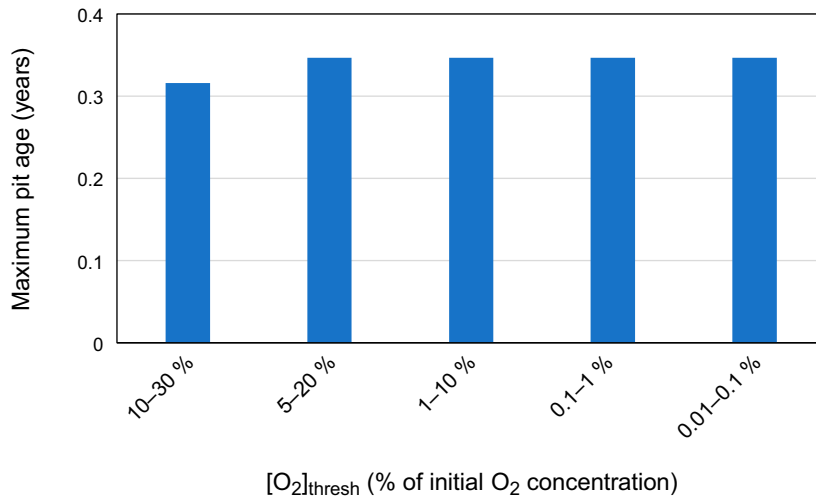
Figure 4-6. Effect of threshold [O₂] range on the maximum pit age. Simulations shown for an overall O₂-consumption time of 1 week to 1 year, DRH range of 55–75 % RH.

The effect of the $[O_2]_{thresh}$ range on the predicted pit depth depends on the form of the pit growth expression and whether average or maximum pit depths are of interest. The time-dependent growth rate given by the soils data of Denison and Romanoff (Figure 3-9) exhibits a rapid initial growth rate followed by a levelling off of the pit depth after 1–2 months. Thus, both the average and, especially, the maximum pit depths are relatively insensitive to the $[O_2]_{thresh}$ (Figure 4-7). The constant propagation rates of 5 µm/yr and 30 µm/yr derived from the results of Ibrahim et al. (2018) and Camitz and Vinka (2003), respectively, give predicted pit depths that are proportional to the pit age, but which are considerably shallower than those predicted using the Denison and Romanoff expression.
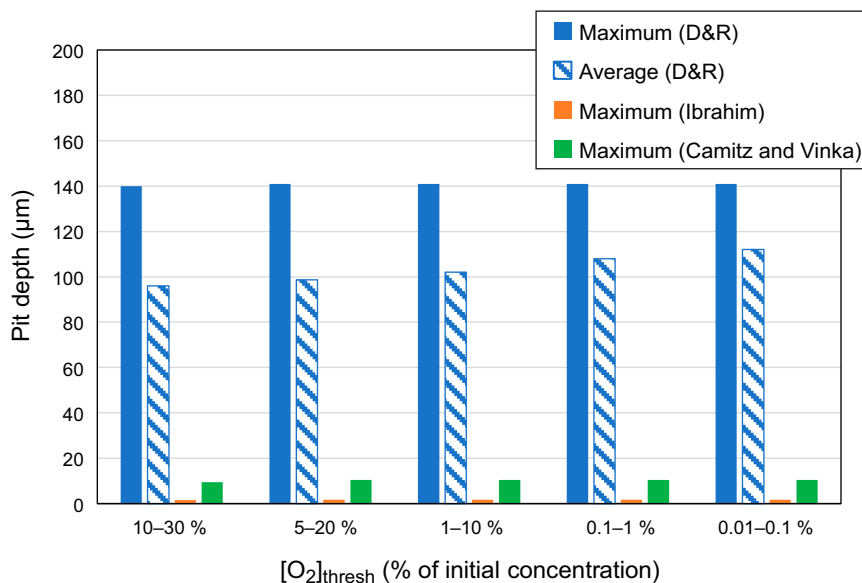
Figure 4-7. Effect of threshold [O₂] range on the predicted pit depth. Maximum and average pit depths are shown for the time-dependent growth expression of Denison and Romanoff (D&R) and maximum pit depth for the constant growth rates of Ibrahim et al. (2018) and Camitz and Vinka (2003). Simulation shown for an overall O₂-consumption time of 1 week to 1 year, DRH range of 55–75 % RH.

4.4 Effect of DRH

The effect of the assumed DRH range on the average and maximum pit ages is shown in Figure 4-8 for various $[O_2]_{thresh}$ values. Since the average pit ages fall within the period when the availability of O_2 is the primary stifling mechanism (cf. Figure 4-4), the average pit age increases with decreasing $[O_2]_{thresh}$ for both DRH ranges considered. This is especially so for the lower DRH range of 35–60 % RH (Figure 4-8(a)), for which pit stifling by drying of the surface is suppressed and does not occur at all for approximately 50 % of the realisations (Table 4-3).

In the case of the maximum pit age (Figure 4-8(b)), there is a difference in behaviour depending on the assumed DRH range. For a DRH range of 55–75 % RH, the maximum pit age is relatively insensitive to $[O_2]_{thresh}$ since drying of the surface is the primary cause of pit stifling. In contrast, for a DRH range of 35–60 % RH, the maximum pit age increases significantly with decreasing $[O_2]_{thresh}$ because the availability of O_2, rather than surface drying, is the principal stifling mechanism and is the only stifling mechanism for those 50 % of realisations where the surface does not dry out.
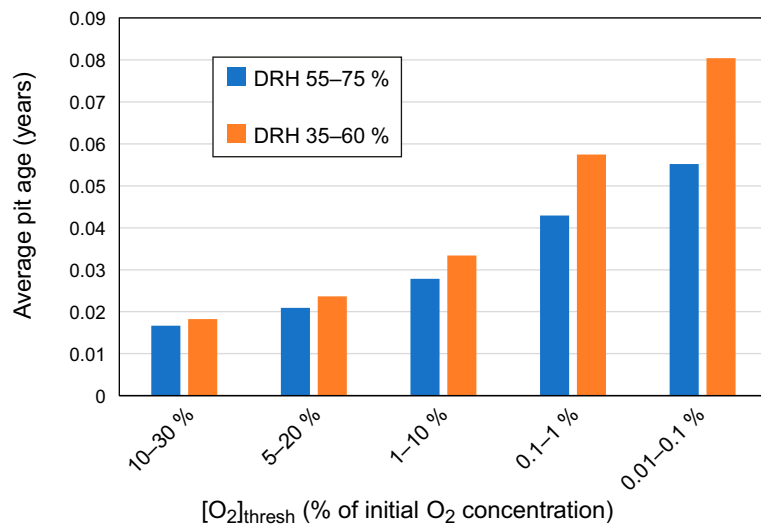
(a) Average pit age
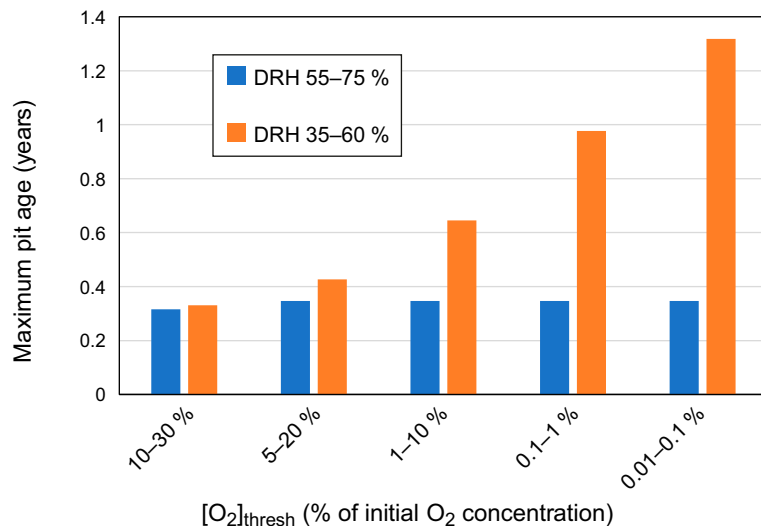
(b) Maximum pit age

***Figure 4-8.** Effect of the DRH range on a) the average, b) maximum pit ages for various $[O_2]$ thresholds. Simulations shown for an overall O_2 consumption time of 1 week to 1 year.*

4.5   Effect of O$_2$-consumption time

All of the results presented to this point have been based on an overall O$_2$-consumption time of 1 week to 1 year. Table 4-4 to Table 4-6 summarise the results of simulations for an overall O$_2$-consumption period of 5 weeks to 5 years, as assumed for the saturated probabilistic pitting model (Briggs et al. 2020, 2021).

Figure 4-9 shows the effect of the O$_2$-consumption time on the predicted average and maximum pit ages for various [O$_2$]$_{thresh}$ ranges. As above, the effect depends on the predominant pit stifling mechanism. Since the average pit ages correspond to the time at which the availability of O$_2$ is the principal stifling mechanism, the average pit age is greater for the slower O$_2$-consumption time (Figure 4-9(a)). In contrast, the maximum pit age is primarily determined by the drying of the canister surface, so that the maximum age does not depend strongly on [O$_2$]$_{thresh}$ or on the O$_2$-consumption rate (Figure 4-9(b)).
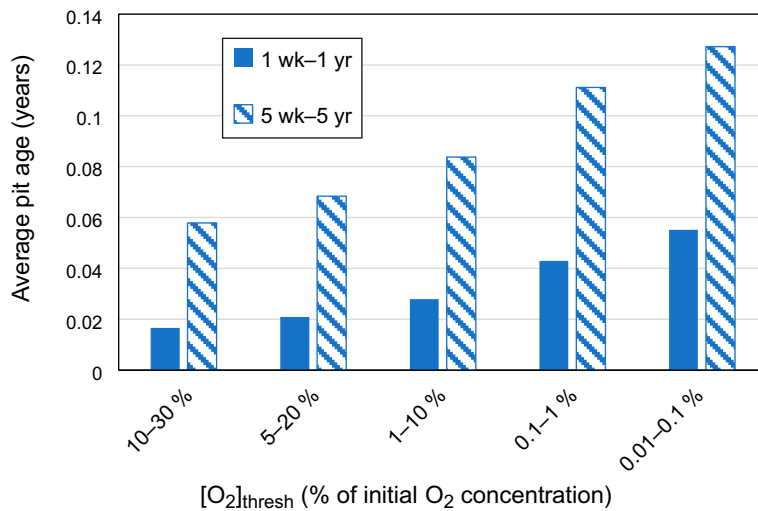
(a) Average pit age
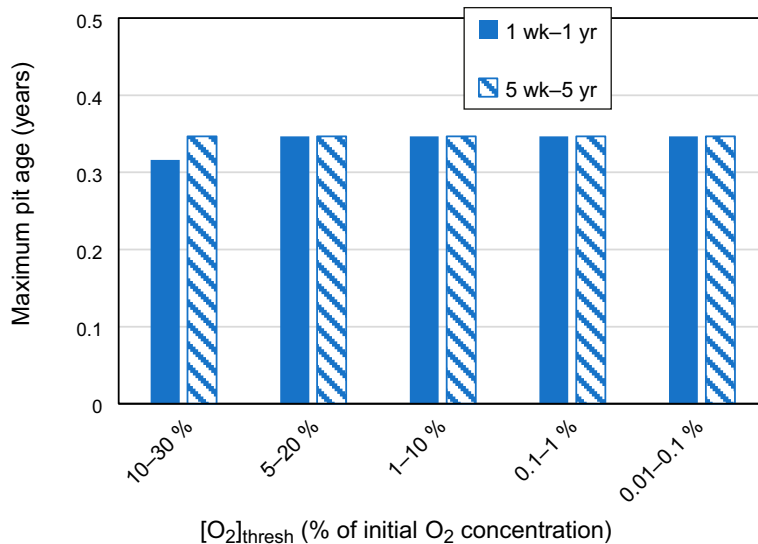
(b) Maximum pit age

Figure 4-9. *Effect of the overall O$_2$-consumption time on the predicted (a) average and (b) maximum pit ages for various [O$_2$]$_{thresh}$ ranges. Simulations shown for a DRH range of 55–75 % RH.*

5 Future developments

Based on the results of the preliminary simulations, various developments to the PUP model have been identified, as described below. In addition, there is the opportunity for further improvement of the underlying conceptual model and of the quality of the input data based on additional experimental studies.

5.1 Implications for future development of the model

5.1.1 Inclusion of the efflorescence relative humidity (ERH)

Drying of the surface has been shown to be an important stifling mechanism. For some combinations of input parameters, the maximum pit age and, hence, the maximum pit depth is determined by the time at which the surface dries. In the current version of the model described here, the DRH is used to determine both whether the surface wets initially and the point at which the surface dries out. Typically, the efflorescence point occurs at an RH lower than the DRH (Section 2.3.1), although the ERH will be affected by corrosion of the surface which may produce corrosion products that are more or less deliquescent than the original surface.

The use of the DRH to represent the point at which the surface dries out is potentially non-conservative as it may lead to an underestimate of the pit age and depth.

One method for including the ERH in the model is to use an "ERH offset" (ΔERH), as follows:

$$ERH = DRH - \Delta ERH \tag{5-1}$$

The values of both DRH and ΔERH would be sampled from distributions for each realisation. The use of an ERH offset avoids the problem that the ERH could be higher than the DRH if both are independently sampled from overlapping distributions.

5.1.2 Improved pit growth expression

The pit growth expression that was used to estimate pit depths in the previous section was derived from a long-term underground corrosion study rather than from atmospheric corrosion tests. A more appropriate expression should be derived from experiments under simulated near-field conditions, ideally as a function of the following parameters:

- Exposure time (up to 1 year)
- Type of salt contaminant and surface condition
- RH
- Temperature
- O_2 concentration

5.1.3 Stifling mechanisms

Environmental stifling mechanisms

The environmentally related stifling mechanisms have been largely implemented in the model already (Table 3-1).

The only remaining environmental stifling mechanism that could be implemented is the decrease in O_2 supply due to saturation of the near field and the resulting decrease in O_2 diffusivity. However, it is apparent from the relative rates of O_2 consumption and buffer saturation that the O_2 will be consumed by corrosion and other processes long before the near-field becomes saturated. Therefore, this stifling mechanism is unlikely to ever be operative under repository conditions and its implementation is not considered to be worthwhile.

Non-environmental stifling mechanisms

None of the potential non-environmental stifling mechanisms has yet been implemented in the model (Table 3-1). While each of the proposed mechanisms has some underlying mechanistic basis, there is insufficient experimental evidence on which to decide how to implement them in the model. Pit stifling by droplet coalescence (stifling mechanism 2(d)) could presumably be related to surface salt loading, although this parameter is not currently included in the model. Other stifling mechanisms, such as the formation of a less-catalytic or blocked cathode or the development of an iR drop (stifling mechanisms 2(a), 2(b), 2(e), and 2(f), respectively) would become increasingly likely with time, but at the moment there is no experimental basis for determining the timescale over which such effects might occur.

Therefore, the implementation of non-environmental stifling mechanisms should be delayed until more mechanistic information becomes available.

5.1.4   Temperature effects

Although a temperature profile is currently selected for each realisation, none of the other parameters in the model is temperature dependent. Therefore, the results are independent of temperature.

In theory, the DRH could be expressed as a function of temperature (Figure 2-3), although the uncertainty in the nature of the surface condition (and of the associated DRH) is probably greater than the variation in DRH with temperature for most potential salt contaminants. Nevertheless, the DRH could be expressed as a function of temperature in order to take into account variability due to the range of canister temperatures.

It is also possible that the pit growth rate is temperature dependent and this is one of the dependences that should be examined experimentally.

However, given that other factors limit the duration of pitting to a few months at most, the variation in the canister surface temperature for a given realisation (and even between realisations) will be relatively minor (Figure 5-1). Thus, even if temperature effects are included in the model, there may not be much effect on the predicted pit ages or depths.
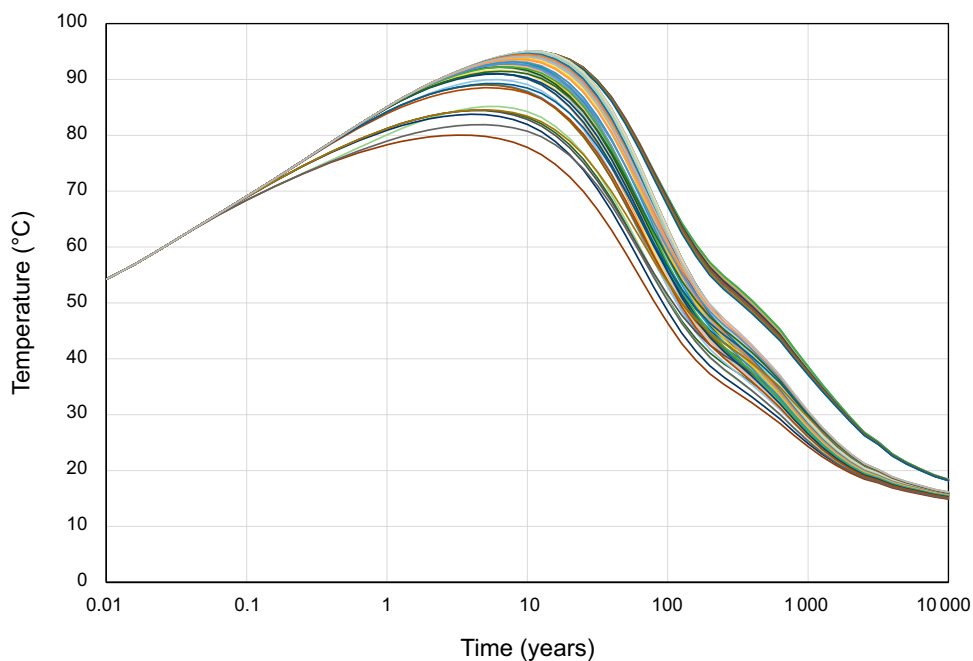
Figure 5-1. *Random collection of temperature profiles for 10 % of the canisters in the repository. Note the relatively small variation in temperature with time and between the different canisters for the period of 0.1 to 1 year corresponding to the period of pitting.*

5.1.5 Improved DRH range

The results of the preliminary simulations are sensitive to the assumed DRH range, not only in terms of the number of canisters subject to pit initiation but also the relative importance of O_2 consumption and surface drying as stifling mechanisms.

Additional experimental studies are required to better characterise the wetting behaviour of the actual canister surface (see below).

5.2 Implications for future experimental measurements

5.2.1 Threshold [O_2] for pit growth

The results of the simulations with various ranges of $[O_2]_{thresh}$, and indeed for no $[O_2]$ threshold, indicate that this is an important parameter in determining pit stifling. Pit propagation cannot continue in the absence of O_2, so such a threshold must exist although the precise value, or range of values, is uncertain.

Experimental confirmation of the existence of an $[O_2]$ threshold for pit propagation would be beneficial, as would as an indication of the actual value (or range of values).

5.2.2 Improved pit growth expression

As noted above, there is a need for an improved pit growth expression, ideally as a function of the various model parameters, including:

- Exposure time
- Type of salt contaminant and surface condition
- RH
- Temperature
- O_2 concentration

In addition to depth-wise penetration, it would also be useful to determine the extent of lateral pit growth (independent of effects due to droplet coalescence). The extent of lateral growth could be expressed as a time- or depth-dependent pit aspect ratio (width:depth).

5.2.3 Nature of canister surface condition

Liquid water will form on the canister surface by a number of processes, including deliquescence of surface contaminants and capillary condensation in pores and surface asperities. For the preliminary simulations, ranges of DRH values have been used based on assumed surface contaminants. The selected DRH range does affect the results, especially in terms of the fraction of canisters affected.

The surface wetting characteristics of samples representative of the surface condition of canisters emplaced in deposition holes should be assessed in order to improve the DRH range used in the simulations.

5.2.4 Non-environmental pit stifling mechanisms

A total of seven non-environmental stifling mechanisms have been proposed (Table 3-1), namely:

- Formation of a less-catalytic cathode (possibly due to oxide formation).
- Blocked cathode (for example, due to the precipitation of $CaCO_3$).
- Lateral spread of the anodic reaction, resulting in a decrease in the cathode:anode surface area ratio.
- Coalescence of adjacent droplets, again resulting in a decrease in the cathode:anode surface area ratio.

- iR drop in the thin electrolyte layer in the region of secondary spreading.

- iR drop due to precipitation in the centre of the droplet resulting from the accumulation of corrosion products.

- Loss of the critical pit chemistry due to the rupture of a cap of precipitated corrosion products.

There may be additional non-environmental stifling mechanisms that have not yet been identified. Any one or more of these potential stifling mechanisms could be implemented in the model if there was sufficient mechanistic evidence, along with an indication of how the mechanism could be implemented numerically.

It is difficult to identify exactly what type of experiments should be conducted, but the ability to make real-time *in situ* electrochemical measurements, coupled with high-resolution visual imaging would seem to be appropriate.

6   Conclusions

A probabilistic model for predicting the pitting of copper canisters in a KBS-3 repository at Forsmark has been developed. The model, referred to as the Probabilistic Unsaturated Pitting (PUP) model, is based on the Evans droplet mechanism for atmospheric corrosion and accounts for the initiation, propagation, and stifling stages of the localised corrosion process. Monte Carlo methods are used to account for the spatial variability in environmental conditions in the repository, as well as uncertainty in the underlying mechanisms and the values of various environment- and pitting-related input parameters. Input parameters are described by probability distribution functions rather than by discrete values. The basic output of the model is the distribution of pit ages and pit depths for all 6 916 canisters in the repository.

The impact of various environment-related stifling mechanisms has been investigated. It has been found that the nature of the near-field environment and how it evolves with time does not support long-lived pits under unsaturated conditions. In particular, the exhaustion of O_2 and the drying of the surface due to the heat output from the canister are predicted to lead to pit stifling. Pitting is limited to the initial dry-out phase of the saturation transient which corresponds to the period of highest O_2 concentration.

The sensitivity of the model predictions to the uncertainty in the overall O_2 consumption time, the deliquescence relative humidity (DRH) for wetting (and drying) of the surface, and the threshold $[O_2]$ ($[O_2]_{thresh}$) for pit stifling has been determined. For the default distribution of O_2-consumption times of 1 week to 1 year (defined as the time to consume 99.9 % of the initial O_2) and default DRH range of 55–75 % RH, the average duration of pitting (i.e., the pit age) varies from 0.017 to 0.055 years (6–20 days) depending on the assumed $[O_2]$ threshold for stifling. The corresponding maximum pit age, which will determine the maximum pit depth, varies from 0.32 to 0.35 years (114–127 days). The average pit age is determined primarily by the time for stifling by the lack of O_2, with the average age increasing as the $[O_2]_{thresh}$ range is decreased from 10–30 % to 0.01–0.1 % of the initial [O]. In contrast, the maximum pit age is determined by the drying of the surface for all $[O_2]_{thresh}$ ranges except for the highest range of 10–30 % of the initial $[O_2]$.

Because the initial RH of the as-emplaced buffer is 71 % RH, pits are predicted to initiate for only 80 % of the realisations for the default RH range of 55–75 % RH. If the DRH range is lowered to 35–60 % RH, pits initiate in all realisations and drying of the surface becomes a less-important stifling mechanism. Thus, for the same overall O_2-consumption time and the same ranges of $[O_2]_{thresh}$, the maximum pit age increases to 0.33–1.3 years compared with the default DRH range, with stifling primarily determined by O_2 exhaustion rather than drying of the surface. The average pit age for the lower DRH range (7–29 days) is similar to that predicted for the default RH range (6–20 days) because O_2 exhaustion rather than drying of the surface is the more important stifling mechanism.

There are relatively few reliable pit growth data for copper under relevant environmental conditions and none as a function of $[O_2]$. Instead, an empirical pit growth expression determined from long-term burial studies in unsaturated soils has been used to estimate the pit depth. The empirical power-law expression predicts relatively rapid initial pit growth kinetics followed by a slow decrease in rate. However, the empirical expression does not explicitly account for the time-dependent RH and $[O_2]$ characteristic of the evolution of the near-field environment. Notwithstanding these limitations, when combined with the predicted pit ages, the average and maximum pit depths for the default O_2-consumption times of 1 week to 1 year and DRH range of 55–75 % RH are 96–112 µm and 140–141 µm, respectively for the various ranges of $[O_2]_{thresh}$. For the lower DRH range of 35–60 % RH, the average and maximum pit depths are predicted to be 96–115 µm and 141–164 µm, respectively.

As well as providing useful insight into the duration and extent of pitting under unsaturated conditions, these preliminary PUP simulations have highlighted areas of further model refinement and of additional experimental studies. Given the importance of O_2 exhaustion and surface drying on pit stifling, it is important to (a) establish experimentally that an $[O_2]$ threshold exists and the approximate value and (b) to formally include an efflorescence RH (ERH) in the model to simulate drying of the surface. Since the ERH ≤ DRH, the incorporation of a distribution for the ERH will tend to

extend the lifetime of pits that are currently predicted to stifle due to drying of the surface. Thus, for the default simulations, the maximum pit age will increase, but the average pit age will be relatively unaffected as it is determined primarily by O_2 exhaustion rather than drying of the surface. The other experimental need is for a more-relevant pit growth expression, ideally as a function of temperature, electrolyte composition, RH and [O_2].

In summary, the PUP model is a useful tool for exploring the duration and extent of localised corrosion during the early saturation and redox transients in the evolution of the near-field environment.

7 Acknowledgements

8 References

SKB's (Svensk Kärnbränslehantering AB) publications can be found at www.skb.com/publications. SKBdoc documents will be submitted upon request to document@skb.se.

Attwood A R, Greenslade M E, 2012. Deliquescence behavior of internally mixed clay and salt aerosols by optical extinction measurements. Journal of Physical Chemistry A 116, 4518–4527.

Birgersson M, Goudarzi R, 2018. Investigations of gas evolution in an unsaturated KBS-3 repository. SKB TR-18-11, Svensk Kärnbränslehantering AB.

Briggs S, Lilja C, King F, 2020. Probabilistic model for the pitting of copper canisters under aerobic, saturated conditions. SKB TR-20-01, Svensk Kärnbränslehantering AB.

Briggs S, Lilja C, King F, 2021. Probabilistic model for pitting of copper canisters. Materials and Corrosion 72, 308–316.

Camitz G, Vinka T-G, 2003. Corrosion resistance of copper in Swedish soils. In Proceedings CEOCOR, Sicily, 2023, European Committee for the Study of Corrosion and protection of Piping Systems, Brussels, Belgium. Available from: https://ceocor.lu/download/2003_sicily/CAMITZ-VINKA-2003-Corrosion-Resistance-of-Copper-in-Swedish-Soils.pdf

Chen Z Y, Kelly R G, 2010. Computational modeling of bounding conditions for pit size on stainless steel in atmospheric environments. Journal of Electrochemical Society 157, C69–C78.

Chen Z Y, Zakipour S, Persson D, Leygraf C, 2004. Effect of sodium chloride particles on the atmospheric corrosion of pure copper. Corrosion 60, 479–491.

Chen Z Y, Persson D, Nazarov A, Zakipour S, Thierry D, Leygraf C, 2005a. In situ studies of the effect of CO_2 on the initial NaCl-induced atmospheric corrosion of copper. Journal of Electrochemical Society 152, B342–B351.

Chen Z Y, Persson D, Samie F, Zakipour S, Leygraf C, 2005b. Effect of carbon dioxide on sodium chloride-induced atmospheric corrosion of copper. Journal of Electrochemical Society 152, B502–B511.

Cole I S, Muster T H, Furman S A, Wright N, Bradbury A, 2008. Products formed during the interaction of seawater droplets with zinc surfaces: I. Results from 1- and 2.5-day exposures. Journal of Electrochemical Society 155, C244–C255.

Cole I S, Muster T H, Lau D, Wright N, Azmat N S, 2010. Products formed during the interaction of seawater droplets with zinc surfaces: II. Results from short exposures. Journal of Electrochemical Society 157, C213–C222.

Cole I S, Muster T H, Azmat N S, Venkatraman M S, Cook A, 2011. Multiscale modelling of the corrosion of metals under atmospheric corrosion. Electrochimica Acta 56, 1856–1865.

CRC, 2019. Handbook of Chemistry and Physics, 100th Edition, 2019–2020, J.R. Rumble (editor-in-chief). Baco Raton, FL: CRC Press, pp. 5-90 to 5-96.

Denison I A, Romanoff M, 1950. Soil-corrosion studies, 1946 and 1948: copper alloys, lead, and zinc. Journal of research of the National Bureau of Standards 44, 259–289.

Evans U R, 1925. Oxygen distribution as a factor in the corrosion of metals. Industrial & Engineering Chemistry 17, 363–372.

Galvele J R, 1976. Transport processes and the mechanism of pitting of metals. Journal of Electrochemical Society 123, 464–474.

Giroud N, 2014. FEBEX – assessment of redox conditions in Phase 2 before dismantling. National Cooperative for the Disposal of Radioactive Waste Arbeitsbericht, NAB 14-55.

Greenspan L, 1977. Humidity fixed points of binary saturated aqueous solutions. Journal of Research of the National Bureau Standards – A. Physics and Chemistry 81, 89–96.

Gupta D, Kim H, Park G, Li X, Eom H J, Ro C U, 2015. Hygroscopic properties of NaCl and NaNO3 mixture particles as reacted inorganic sea-salt aerosol surrogates. Atmospheric Chemistry and Physics 15, 3379–3393.

Ha H, Taxén C, Williams K, Scully J, 2011. Effects of selected water chemistry variables on copper pitting propagation in potable water. Electrochimica Acta 56, 6165–6183.

Hedin A, 2004. Integrated near-field evolution model for a KBS-3 repository. SKB R-04-36, Svensk Kärnbränslehantering AB.

Ibrahim B, Zagidulin D, Behazin M, Ramamurthy S, Wren J C, Shoesmith D W, 2018. The corrosion of copper in irradiated and unirradiated humid air. Corrosion Science 141, 53–62.

Johansson A J, Svensson D, Gordon A, Pahverk H, Karlsson O, Brask J, Lundholm M, Malmström D, Gustavsson F, 2020. Corrosion of copper after 20 years exposure in the bentonite field tests LOT S2 and A3. SKB TR-20-14, Svensk Kärnbränslehantering AB.

King F, 2006. Review and gap analysis of the corrosion of copper containers under unsaturated conditions. Ontario Power Generation, Nuclear Waste Management Division Report No.: 06819-REP-01300-10124.

King F, Lilja C, 2014. Localised corrosion of copper canisters. Corrosion Engineering, Science and Technology 49, 420–424.

King F, Litke C D, Tang Y, 1995a. Effect of interfacial pH on the reduction of oxygen on copper in neutral $NaClO_4$ solution. Journal of Electroanalytical Chemistry 384, 105–113.

King F, Quinn M J, Litke C D, 1995b. Oxygen reduction on copper in neutral NaCl solution. Journal of Electroanalytical Chemistry 385, 45–55.

King F, Van Boven G, Lawson K, Thompson N, Nichols P, Reid R, 2006. Cathodic protection of pipelines in high resistivity soils and the effect of seasonal changes. CORROSION/2006 (NACE International, Houston, TX), paper 06163.

King F, Lilja C, Pedersen K, Pitkänen P, Vähänen M, 2010. An update of the state-of-the-art report on the corrosion of copper under expected conditions in a deep geologic repository. SKB TR-10-67, Svensk Kärnbränslehantering AB.

King F, Chen J, Qin Z, Shoesmith D, Lilja C, 2017. Sulphide-transport control of the corrosion of copper canisters. Corrosion Engineering, Science and Technology, 52:sup1, 210–216.

Lucey V F, 1967. Mechanism of pitting corrosion of copper in supply waters. British Corrosion Journal 2, 175–185.

Lytle D A, Nadagouda M N, 2010. A comprehensive investigation of copper pitting in a drinking water distribution system. Corrosion Science 52, 1927–1938.

Malmberg D, Åkesson M, 2020. Relative-humidity evolution near the canister in models: Analysis of SR-Site and Prototype Repository models. SKBdoc 1885367 ver 1.0, Svensk Kärnbränslehantering AB.

Muster T H, Bradbury A, Trinchi A, Cole I S, Markley T, Lau D, Dligatch S, Bendavid A, Marin P, 2011. The atmospheric corrosion of zinc: The effects of salt concentration, droplet size and droplet shape. Electrochimica Acta 56, 1866–1873.

Peng C, Chen L, Tang M, 2022. A database for deliquescence and efflorescence relative humidities of compounds with atmospheric relevance. Fundamental Research 2, 578–587.

Posiva, 2021. Canister evolution. Posiva Working Report 2021-06, Posiva Oy, Finland.

Robinson R A, Stokes R H, 1959. Electrolyte Solutions, Second Edition Revised, Butterworths (London), Appendices 8.3 and 8.5.

Schindelholz E J, Risteen B E, Kelly R G, 2014. Effect of relative humidity on corrosion of steel under sea salt aerosol proxies. Journal of Electrochemical Society 161, C450–C459.

Schindelholz E J, Cong H, Jove-Colon C F, Li S, Ohlhausen J A, Moffat H K, 2018. Electrochemical aspects of copper atmospheric corrosion in the presence of sodium chloride. Electrochimica Acta 276, 194–206.

Situm A, Sabeti M, Schmidt N, Zagidulin D, Behazin M, Noël J J, 2024. Monitoring alterations in a salt layer's deliquescence properties during the atmospheric corrosion of a metal surface using a quartz crystal microbalance. Corrosion Science 229, 111845.

SKB, 2010. Corrosion calculations report for the safety assessment SR-Site. SKB TR-10-66, Svensk Kärnbränslehantering AB.

SKB, 2019. Supplementary information on canister integrity issues. SKB TR-19-15, Svensk Kärnbränslehantering AB.

SKB, 2022a. Post-closure safety for the final repository for spent nuclear fuel at Forsmark. Main report, PSAR version. SKB TR-21-01, Svensk Kärnbränslehantering AB.

SKB, 2022b. Buffer, backfill and closure process report, PSAR version. SKB TR-21-03, Svensk Kärnbränslehantering AB.

SKB, 2022c. Fuel and canister process report, PSAR version. SKB TR-21-02, Svensk Kärnbränslehantering AB.

Tang I N, Tridico A C, Fung K H, 1997. Thermodynamic and optical properties of sea salt aerosols. Journal of Geophysical Research: Atmospheres 102, 23269–23275.

Taxén, C, 2013. Ytprofiler på kopparkapslar från deponeringshål 5 och 6 i försöksserien Prototyp. SKB P-13-50, Svensk Kärnbränslehantering AB.

Taxén, C, Lundholm M, Persson D, Jakobsson D, Sedlakova M, Randelius M, Karlsson O, Rydgren P, 2012. Analyser av koppar från prototypkapsel 5 och 6. SKB P-12-22, Svensk Kärnbränslehantering AB.

Tomonaga Y, Giroud N, Brennwald M S, Horstmann E, Diomidis N, Kipfer R, Wersin P, 2019. On-line monitoring of the gas composition in the Full-scale Emplacement experiment at Mon Terri (Switzerland). Applied Geochemistry 100, 234–243.

Tsuru T, Tamiya K-I, Nishikata A, 2004. Formation and growth of micro-droplets during the initial stage of atmospheric corrosion. Electrochimica Acta 49, 2709–2715.

Ushijima S B, Davis R D, Tolbert M A, 2018. Immersion and contact efflorescence induced by mineral dust particles. Journal of Physical Chemistry A 122, 1303–1311.

Wersin P, Kober F (eds), 2017. FEBEX-DP. Metal corrosion and iron-bentonite interaction studies. National Cooperative for the Disposal of Radioactive Waste Arbeitsbericht, NAB 16-16.

You C, Briggs S, Orazem M E, 2023. Model development methodology for localized corrosion of copper. Corrosion Science 222, 111388.

Zhang J, Wang J, Wang Y, 2005. Micro-droplets formation during the deliquescence of salt particles in atmosphere. Corrosion 61, 1167–1172.

Results from all sensitivity analyses

The following plots are given below for each of the sensitivity analyses:

(a) time dependence of the various environmental stifling mechanisms,

(b) distribution of pit ages,
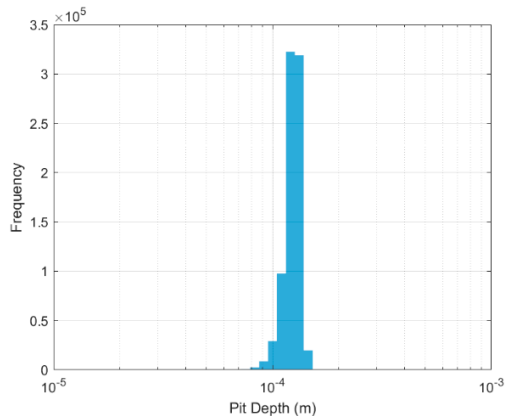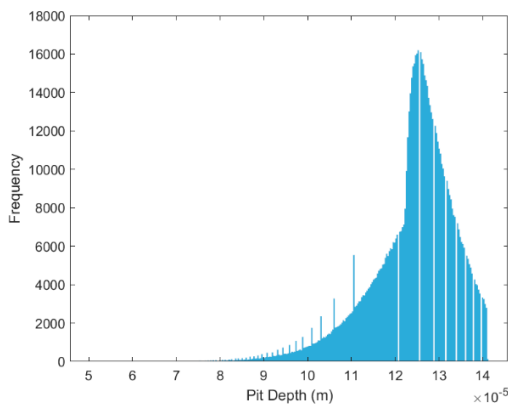
(c) cumulative distribution of the pit ages,

(d) distribution of pit depths on a linear depth scale, and

(e) distribution of pit depths on a logarithmic depth scale.

A1 O$_2$ consumption time 1 week – 1 year, DRH 55–75 % RH

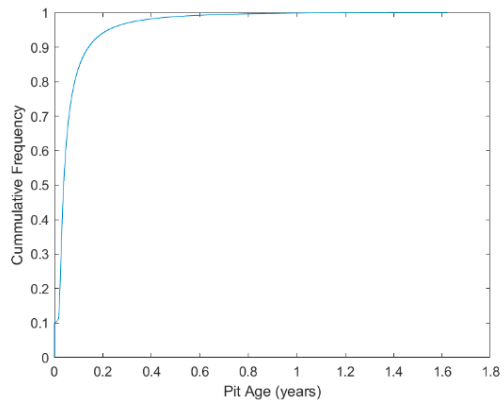The summary of the results is given in Table 4-2.

A1.1 O$_2$ threshold 10–30 % of initial concentration
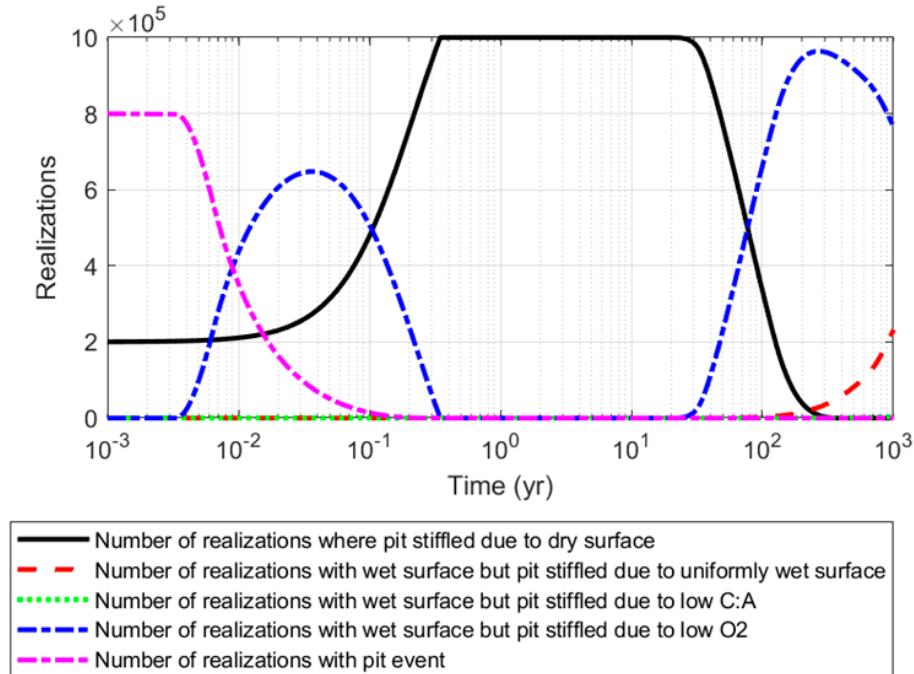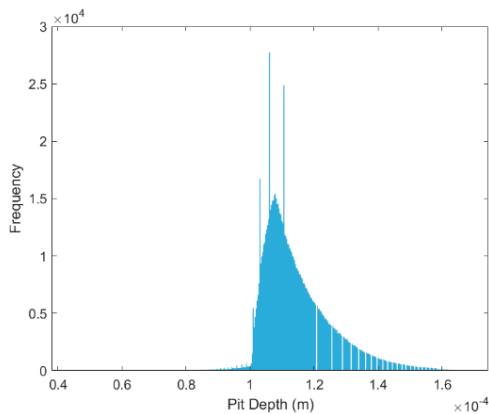

(a) Time dependence of the various stifling mechanisms.
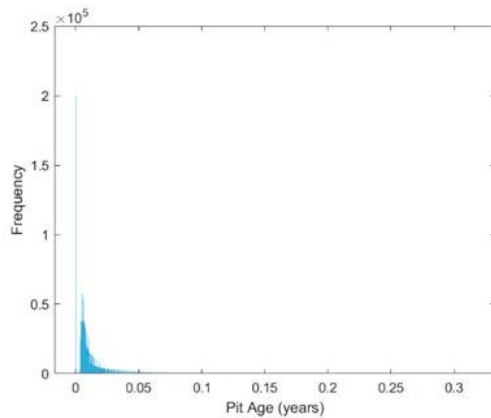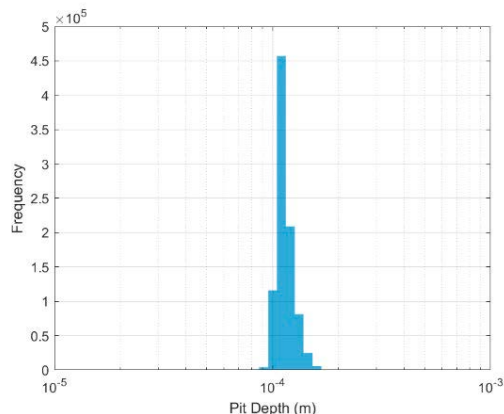

(b) Distribution of pit ages.
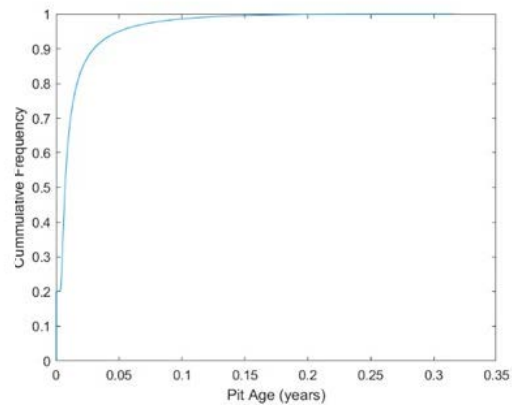
(c) Cumulative distribution of pit ages.
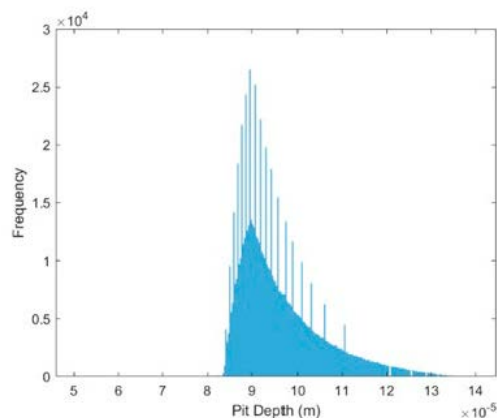
(d) Distribution of pits depths (linear scale).
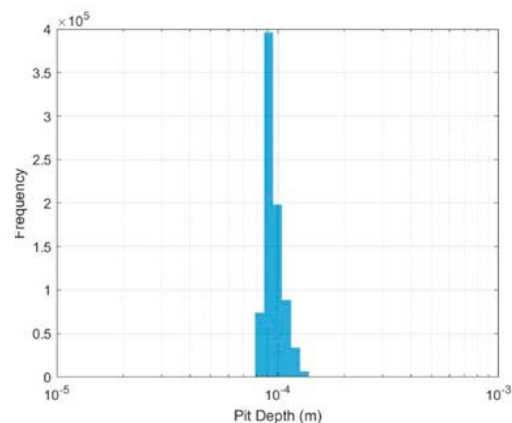
(e) Distribution of pits depths (logarithmic scale).

A1.2   O₂ threshold 5–20 % of initial concentration
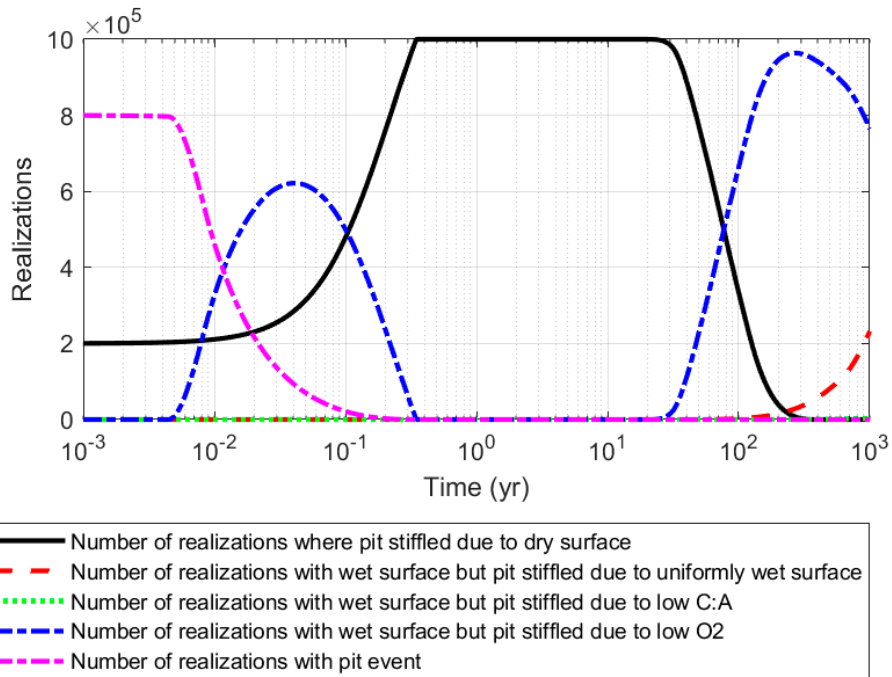
(a) Time dependence of the various stifling mechanisms.
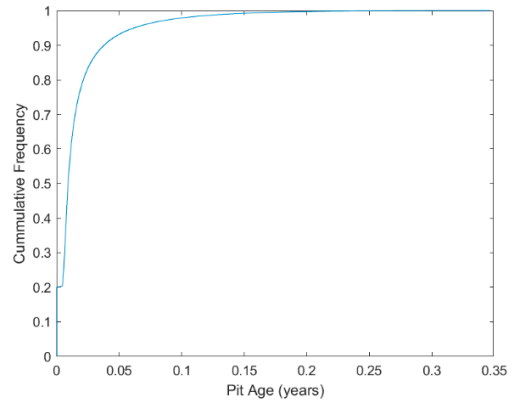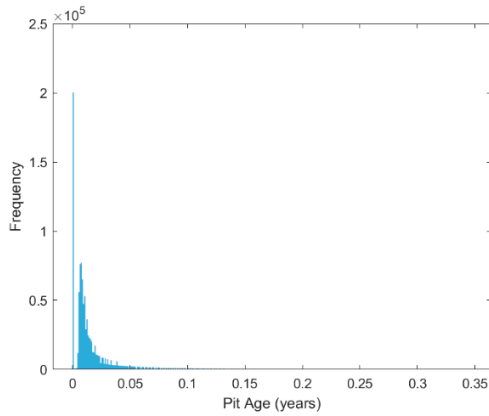
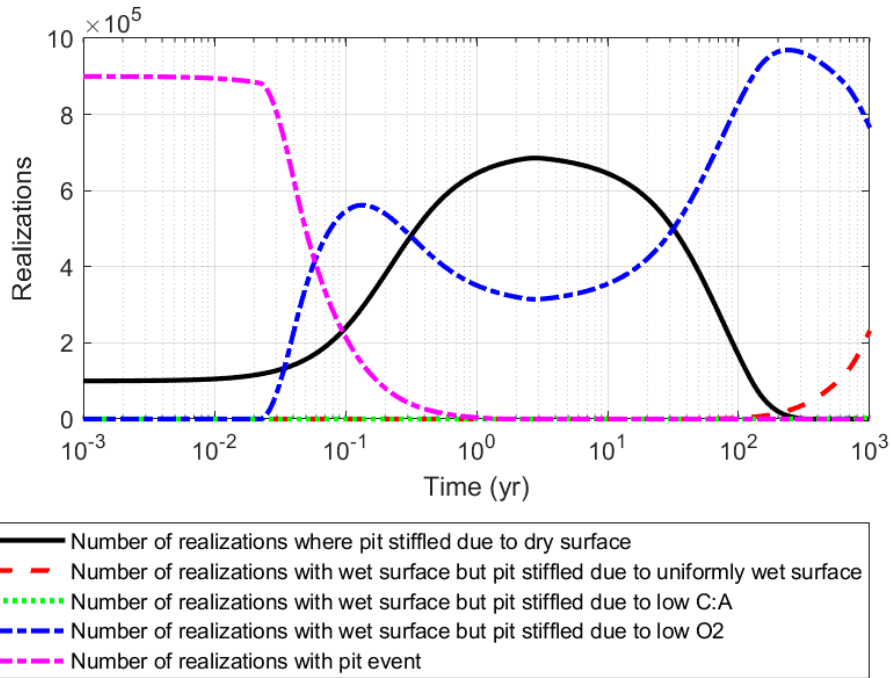(b) Distribution of pit ages.

(c) Cumulative distribution of pit ages.
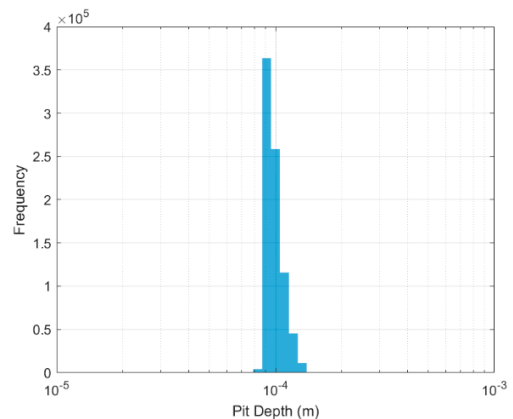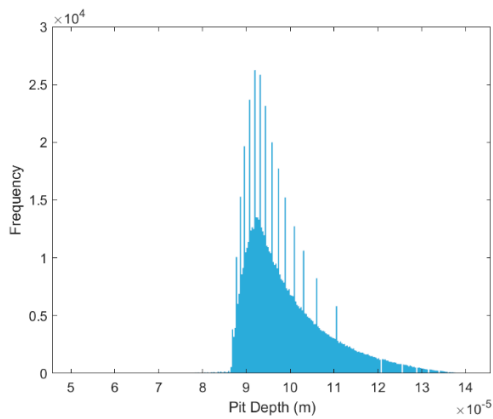
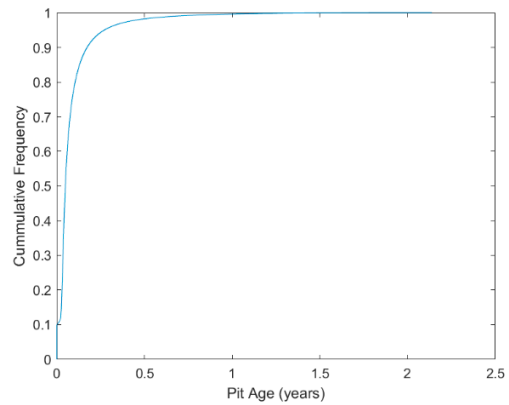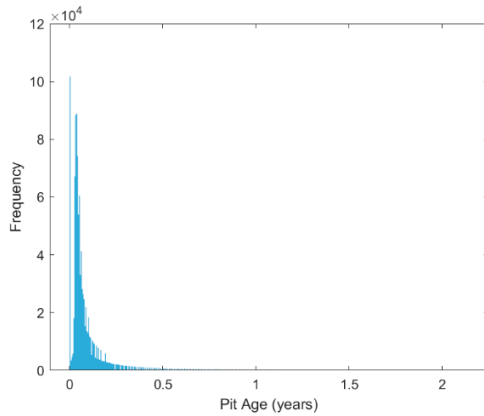(d) Distribution of pits depths (linear scale).

(e) Distribution of pits depths (logarithmic scale).

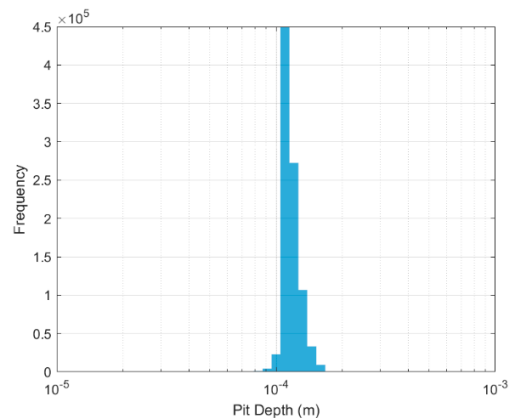## A1.3   O₂ threshold 1–10 % of initial concentration
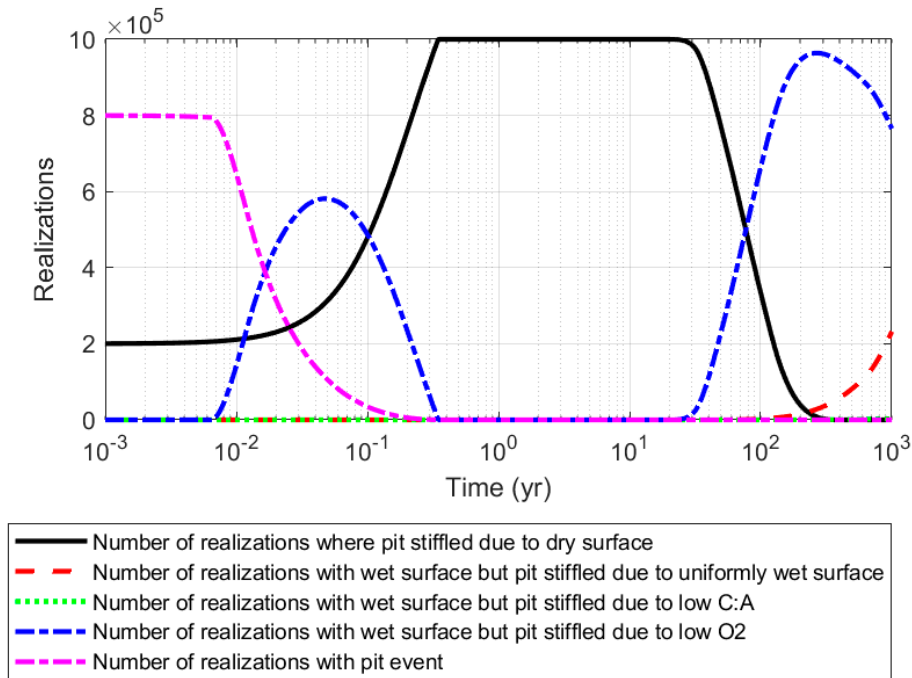
(a) Time dependence of the various stifling mechanisms.
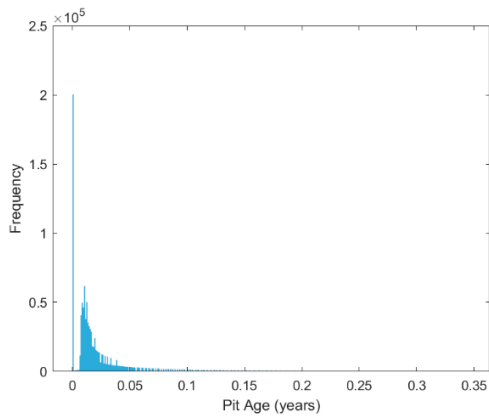
(b) Distribution of pit ages.
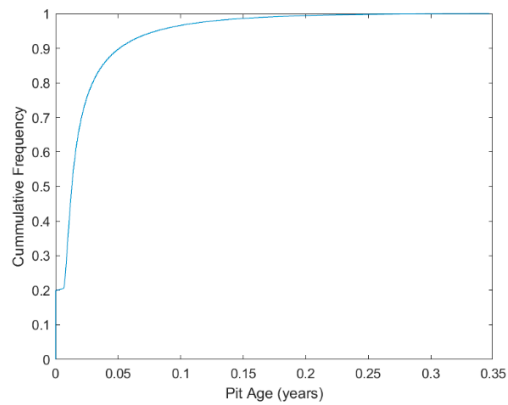
(c) Cumulative distribution of pit ages.
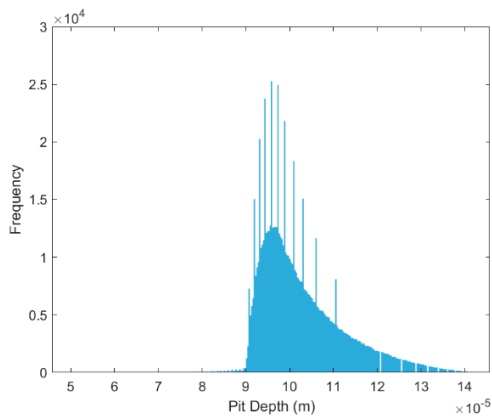
(d) Distribution of pits depths (linear scale).
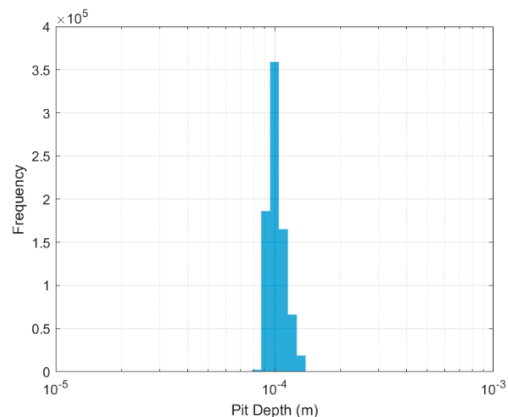
(e) Distribution of pits depths (logarithmic scale).

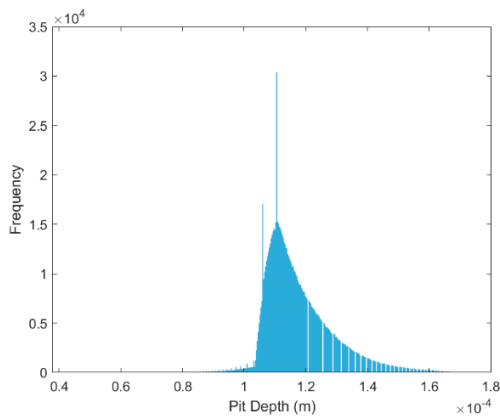## A1.4   O$_2$ threshold 0.1–1 % of initial concentration
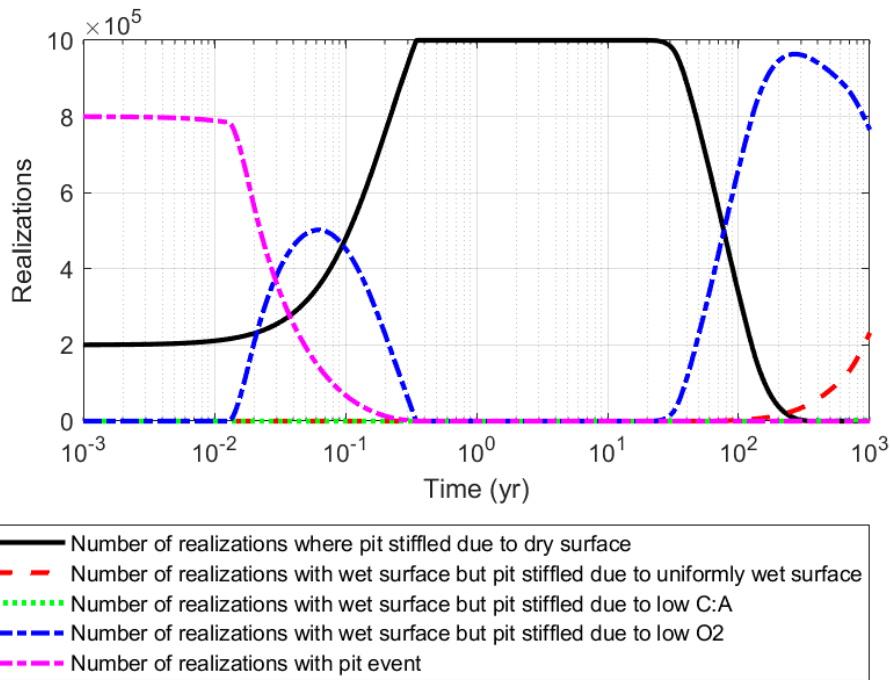
(a) Time dependence of the various stifling mechanisms.
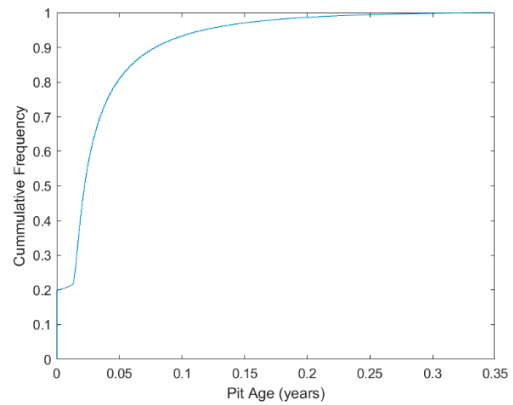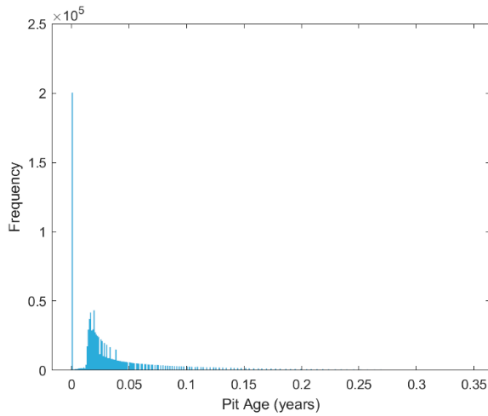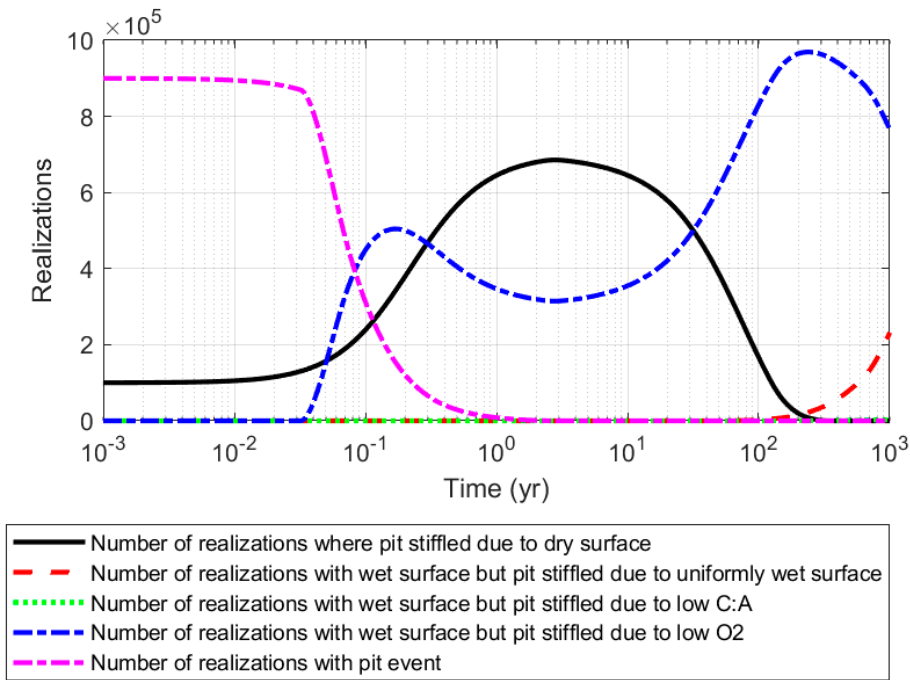

(b) Distribution of pit ages.
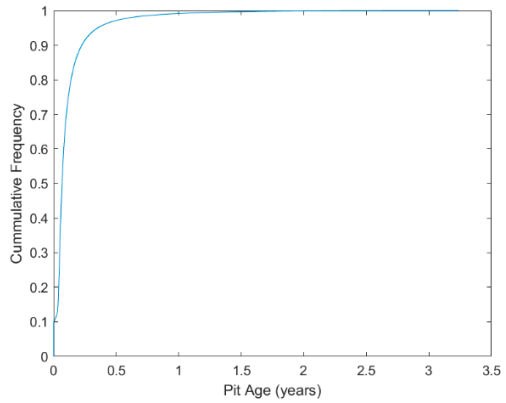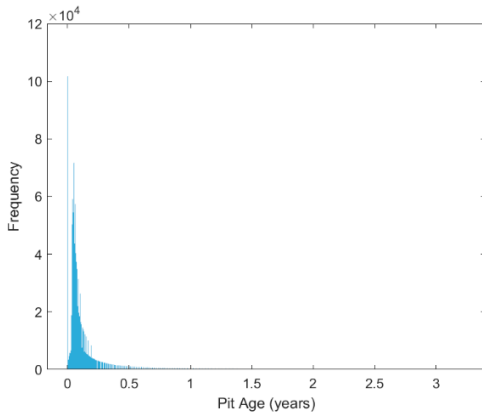

(c) Cumulative distribution of pit ages.
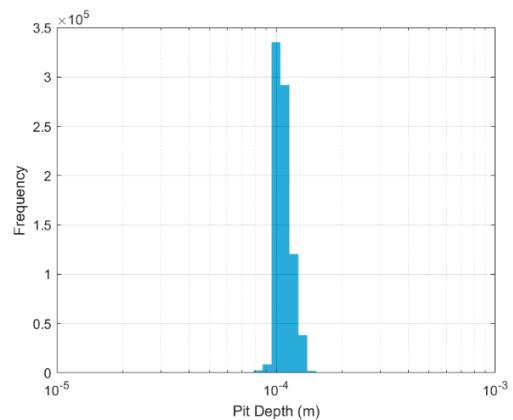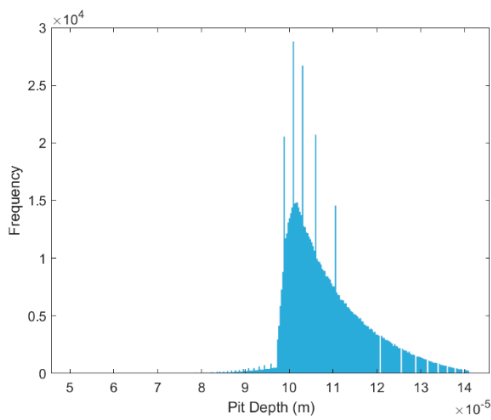
(d) Distribution of pits depths (linear scale).

(e) Distribution of pits depths (logarithmic scale).

A1.5 O₂ threshold 0.01–0.1 % of initial concentration
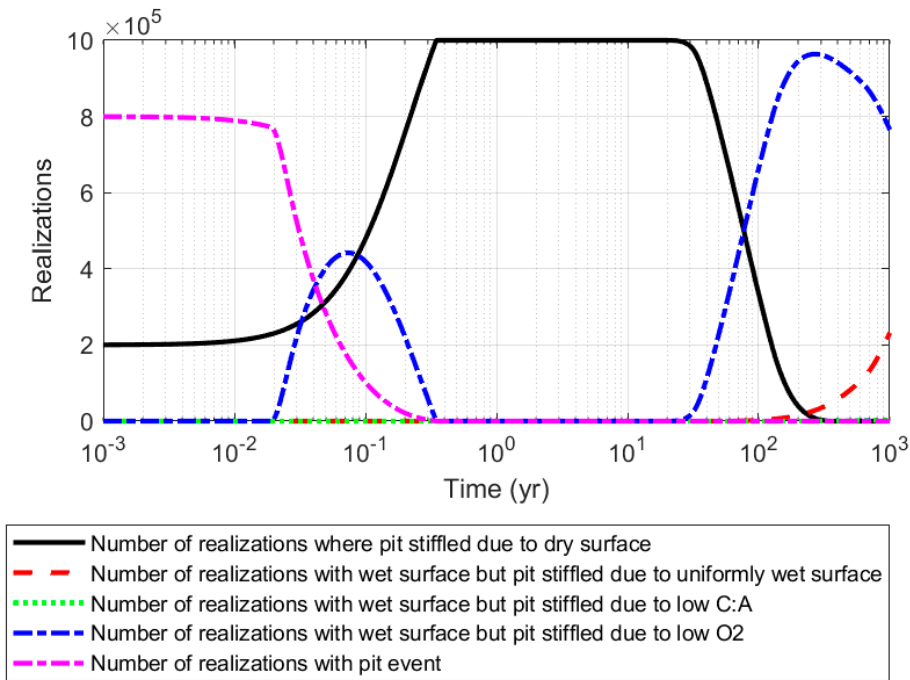
Number of realizations where pit stiffled due to dry surface
Number of realizations with wet surface but pit stiffled due to uniformly wet surface
Number of realizations with wet surface but pit stiffled due to low C:A
Number of realizations with wet surface but pit stiffled due to low O2
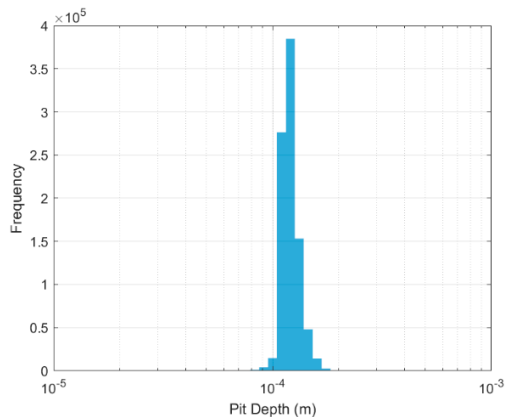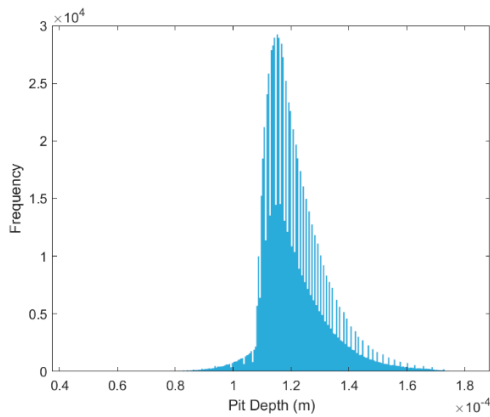Number of realizations with pit event

(a) Time dependence of the various stifling mechanisms.
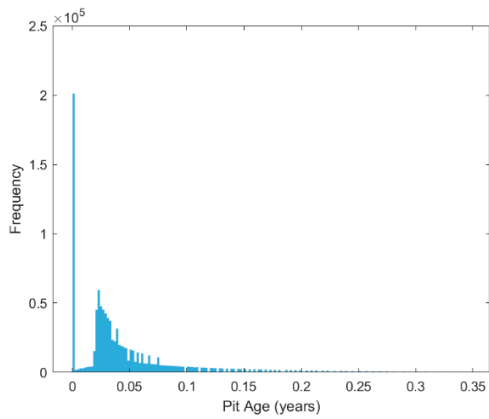
(b) Distribution of pit ages.
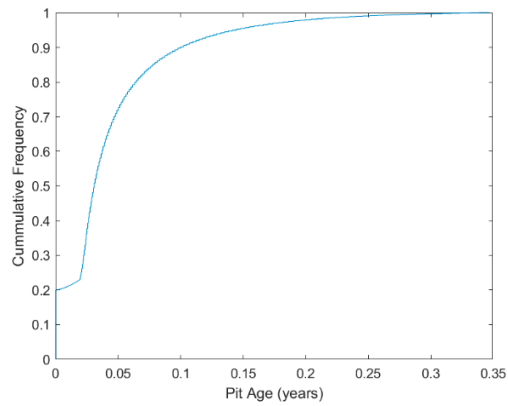
(c) Cumulative distribution of pit ages.
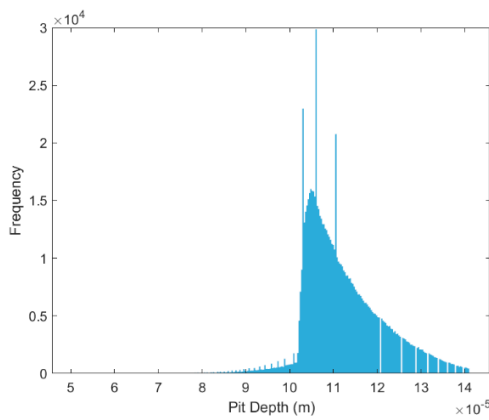
(d) Distribution of pits depths (linear scale).
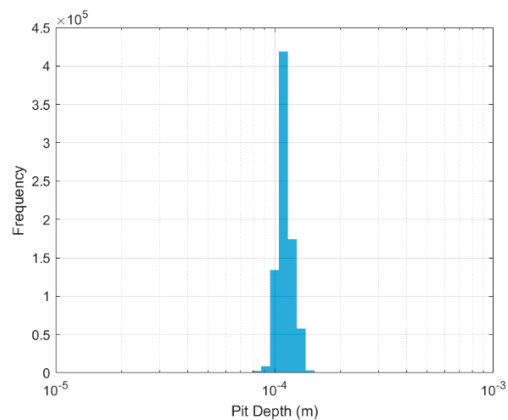
(e) Distribution of pits depths (logarithmic scale).

A1.6   O₂ threshold 0 %
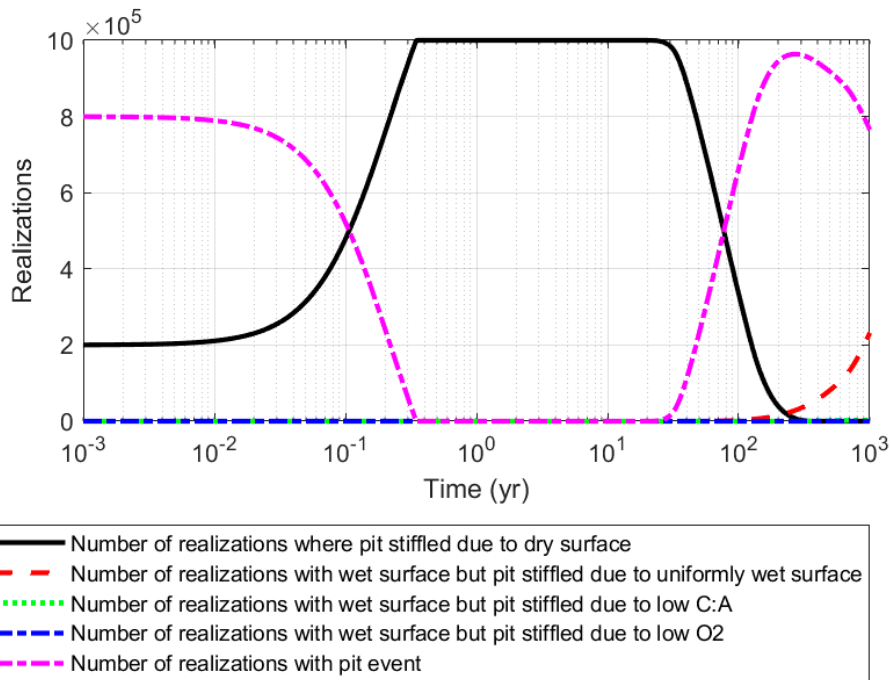
(a) Time dependence of the various stifling mechanisms.
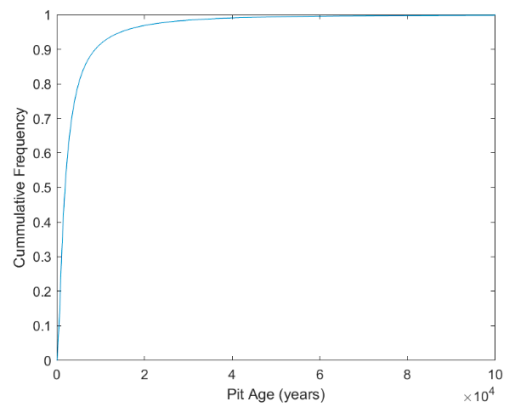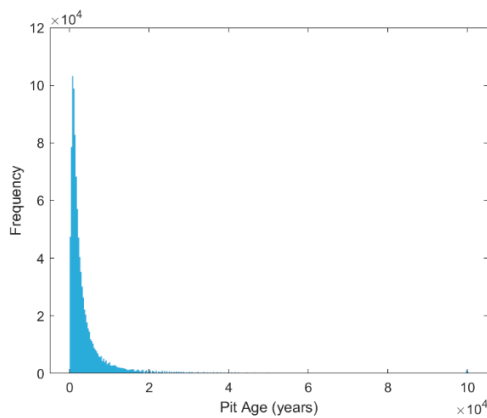
Legend:
- Number of realizations where pit stiffled due to dry surface
- Number of realizations with wet surface but pit stiffled due to uniformly wet surface
- Number of realizations with wet surface but pit stiffled due to low C:A
- Number of realizations with wet surface but pit stiffled due to low O2
- Number of realizations with pit event

(b) Distribution of pit ages.

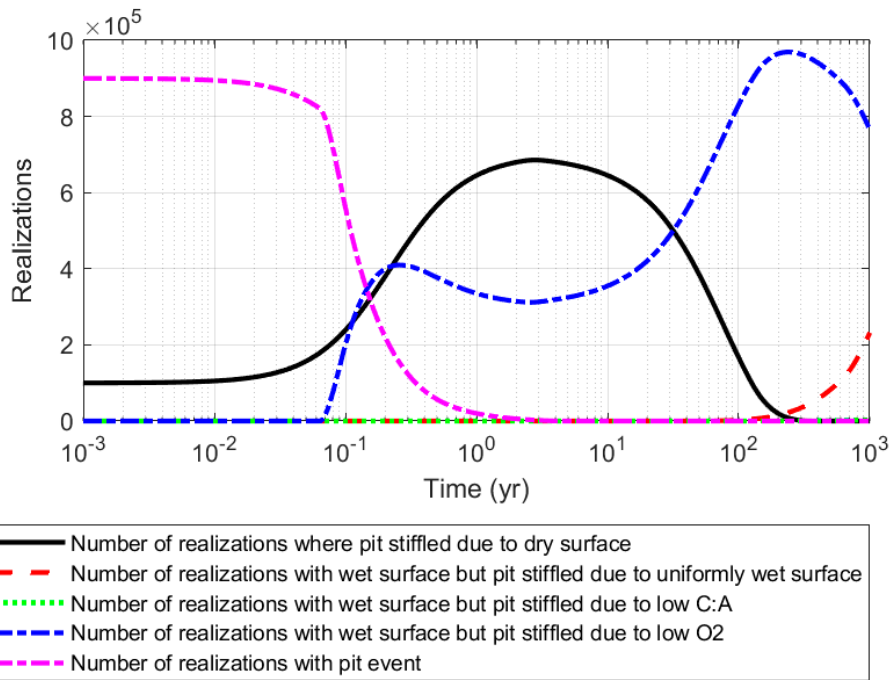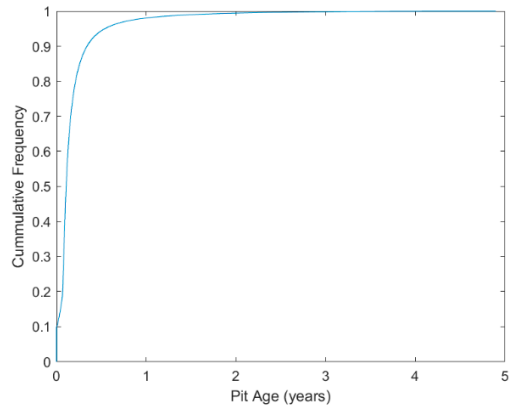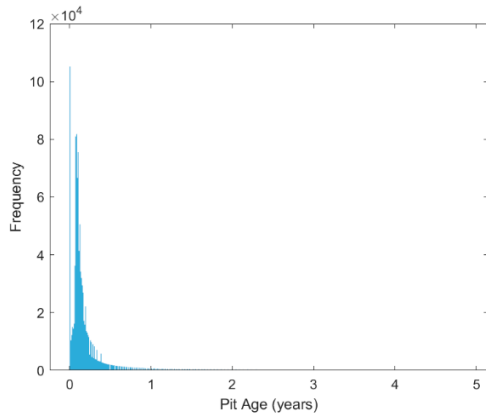(c) Cumulative distribution of pit ages.
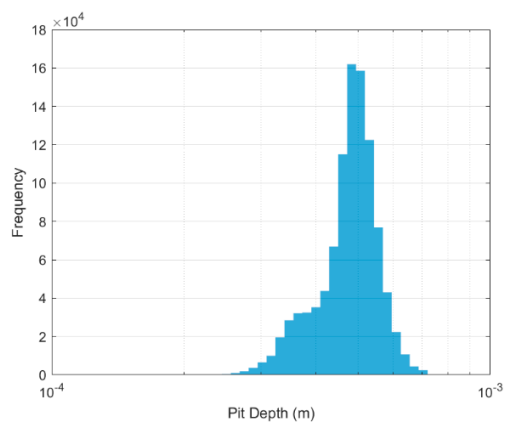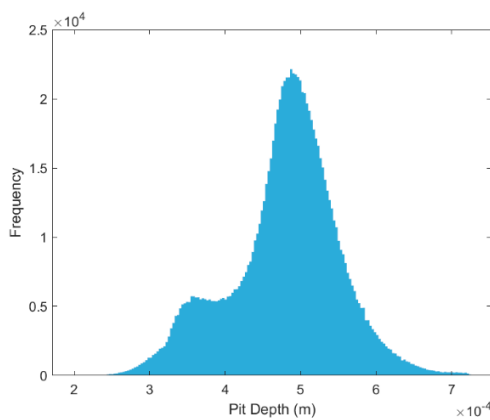
(d) Distribution of pits depths (linear scale).

(e) Distribution of pits depths (logarithmic scale).

A2   O$_2$ consumption time 1 week – 1 year, DRH 35–60 % RH

The summary of the results is given in Table 4-3.

A2.1   O$_2$ threshold 10–30 % of initial concentration
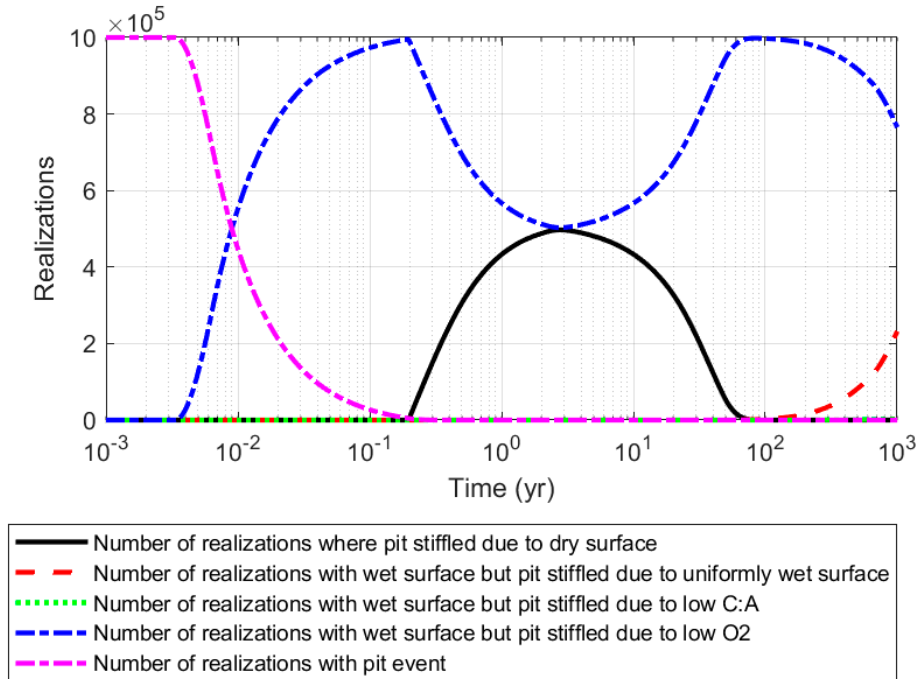
Number of realizations where pit stiffled due to dry surface
Number of realizations with wet surface but pit stiffled due to uniformly wet surface
Number of realizations with wet surface but pit stiffled due to low C:A
Number of realizations with wet surface but pit stiffled due to low O2
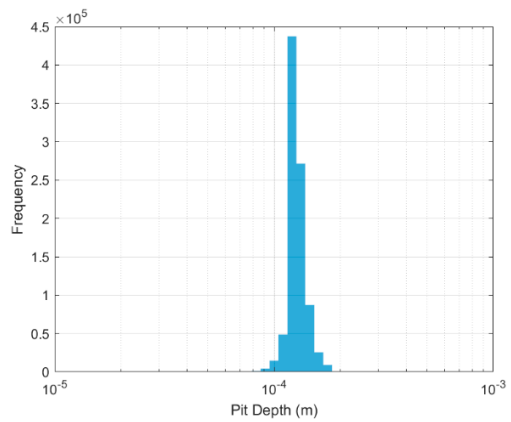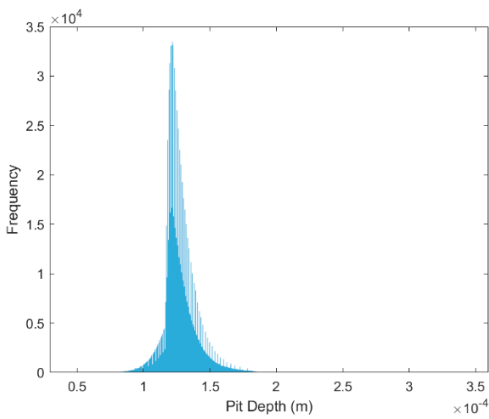Number of realizations with pit event

(a) Time dependence of the various stifling mechanisms.
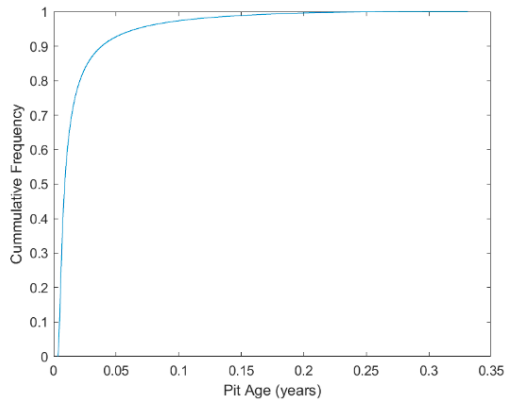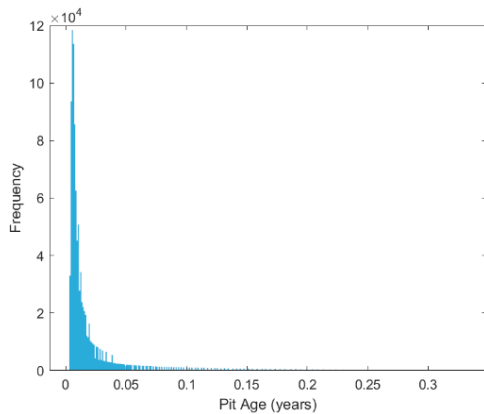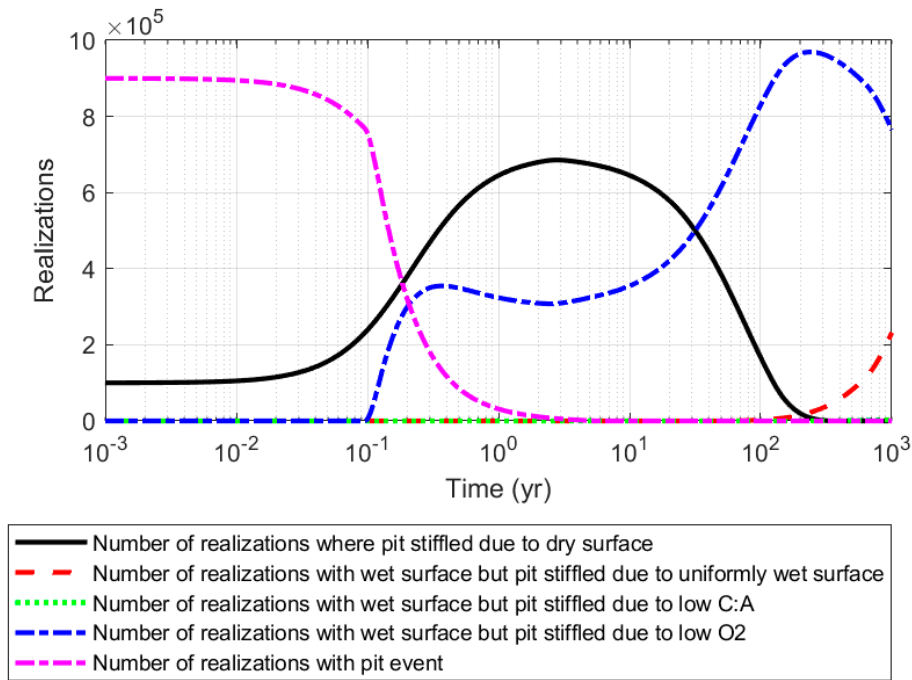

(b) Distribution of pit ages.
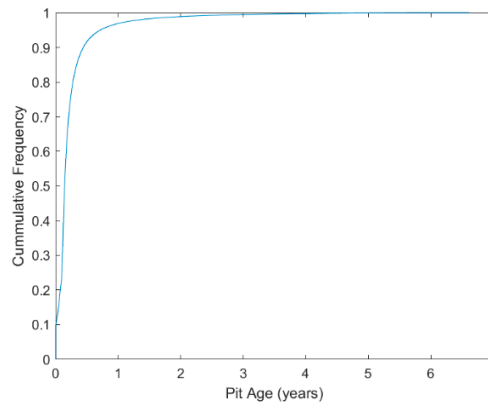

(c) Cumulative distribution of pit ages.
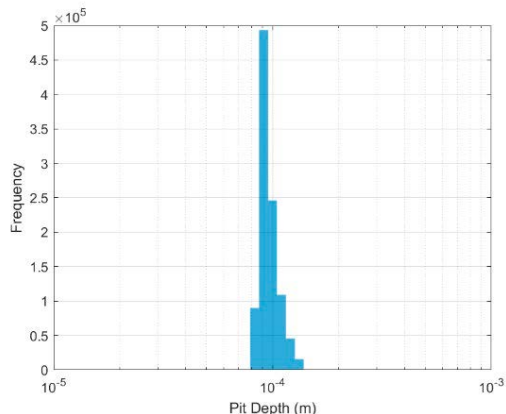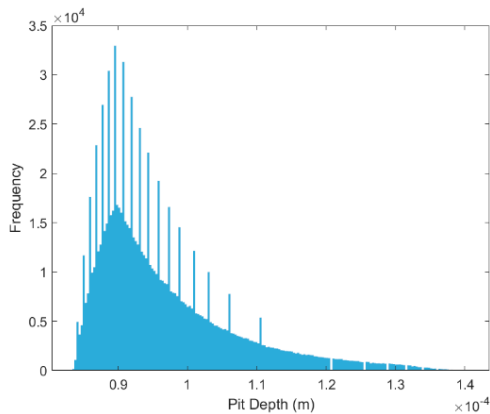
(d) Distribution of pits depths (linear scale).

(e) Distribution of pits depths (logarithmic scale).

A2.2 O₂ threshold 5–20 % of initial concentration
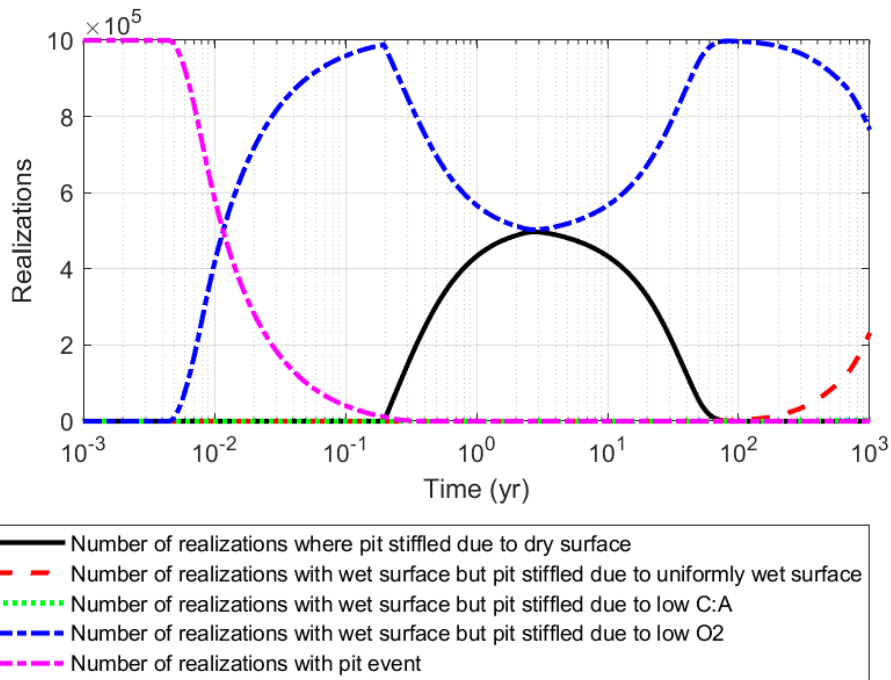
(a) Time dependence of the various stifling mechanisms.
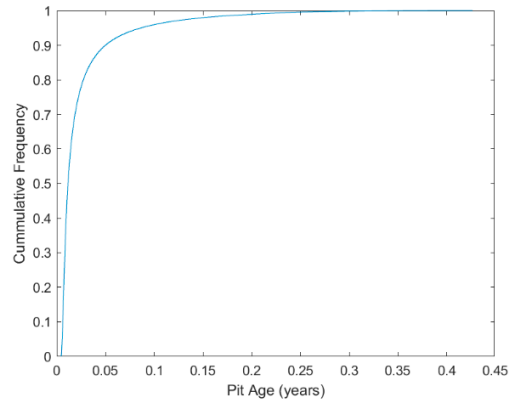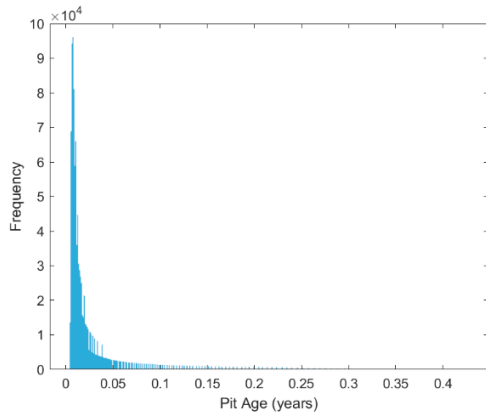
(b) Distribution of pit ages.
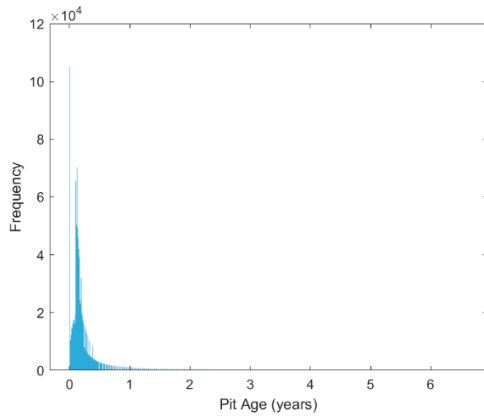
(c) Cumulative distribution of pit ages.
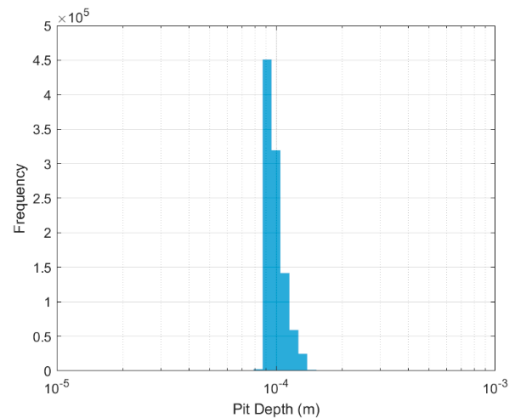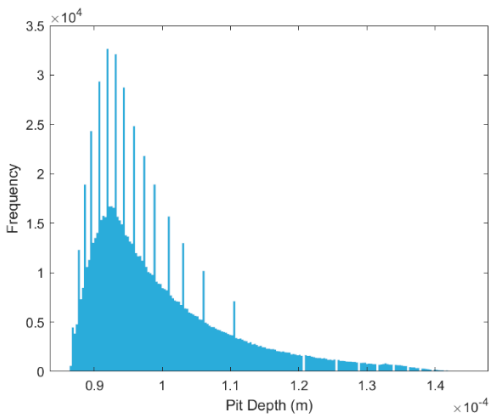
(d) Distribution of pits depths (linear scale).

(e) Distribution of pits depths (logarithmic scale).

A2.3 O$_2$ threshold 1–10 % of initial concentration
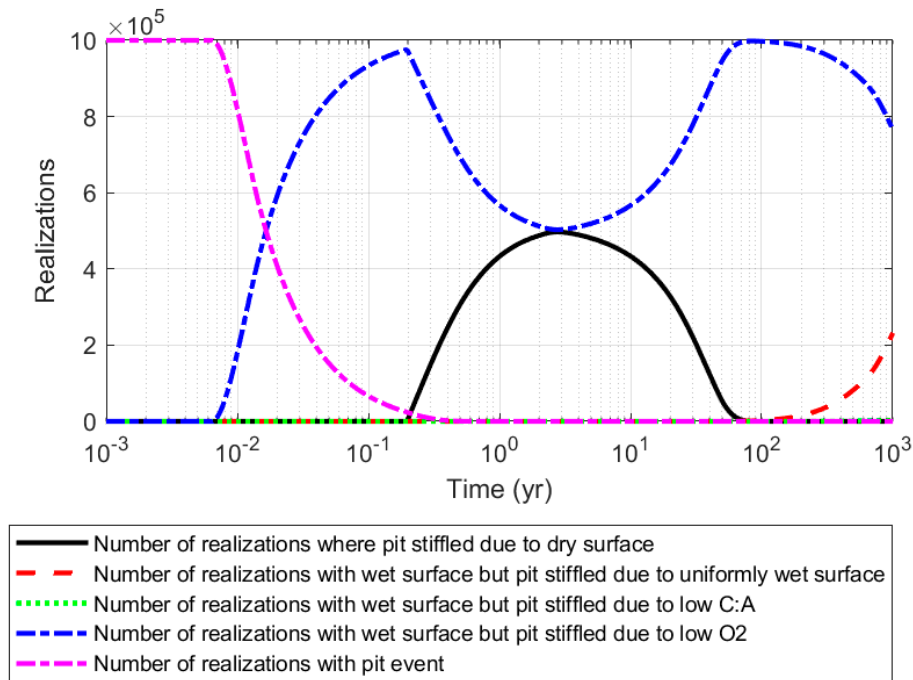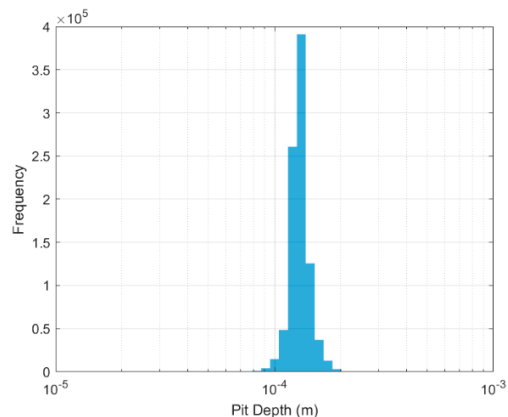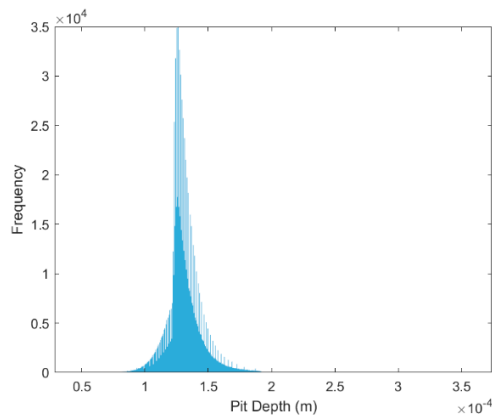

(a) Time dependence of the various stifling mechanisms.
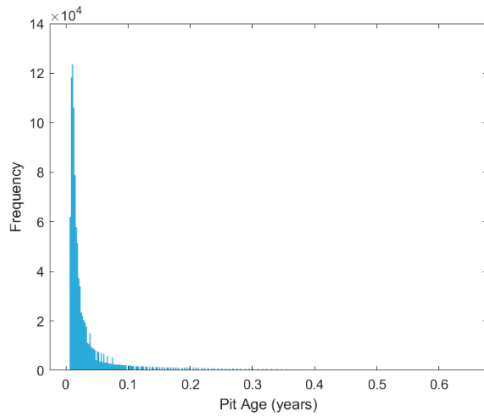
(b) Distribution of pit ages.
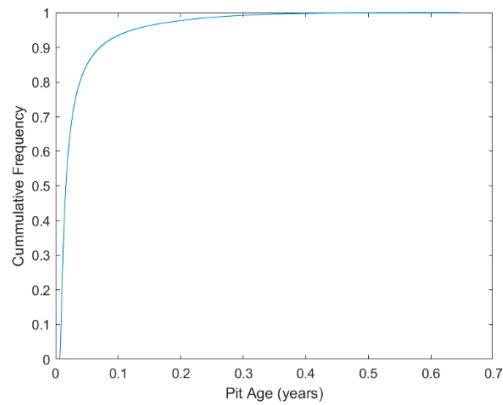
(c) Cumulative distribution of pit ages.
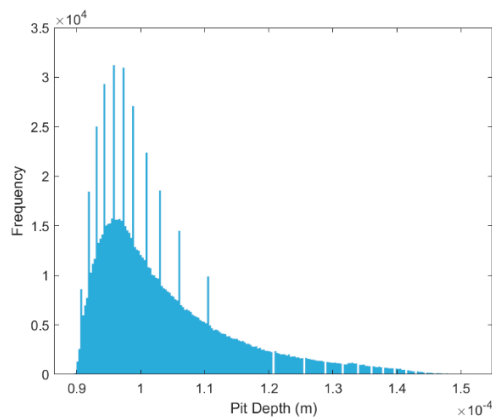
(d) Distribution of pits depths (linear scale).
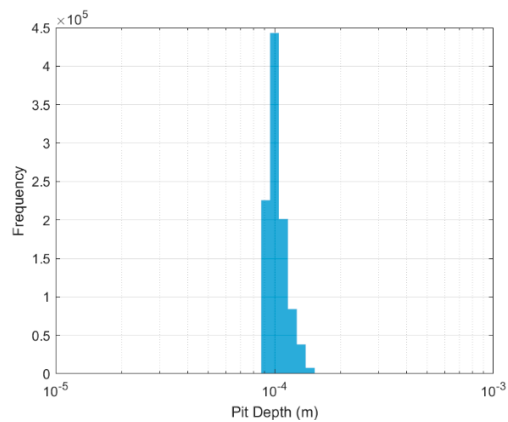
(e) Distribution of pits depths (logarithmic scale).

A2.4 O$_2$ threshold 0.1–1 % of initial concentration
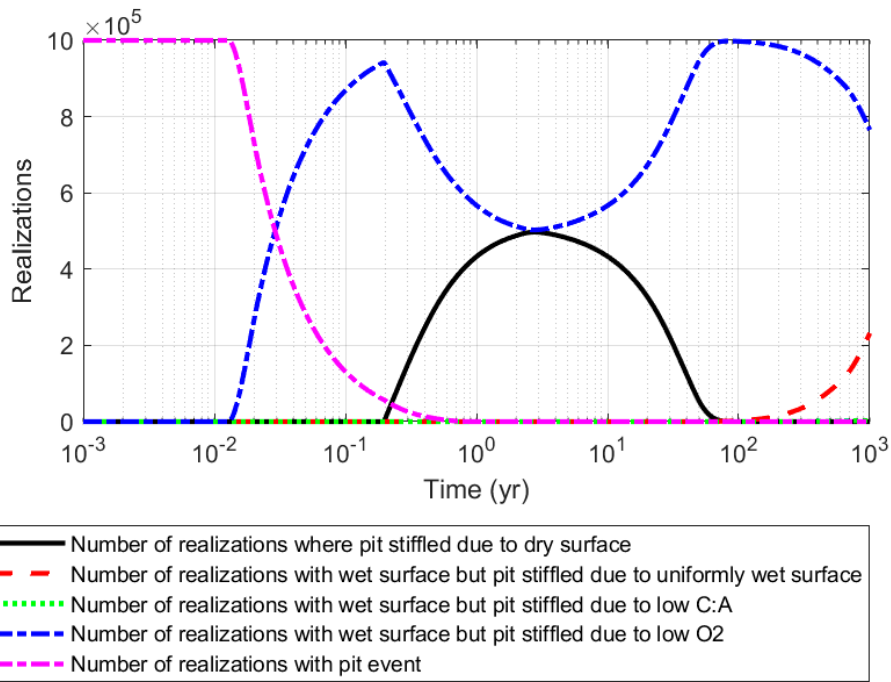
(a) Time dependence of the various stifling mechanisms.
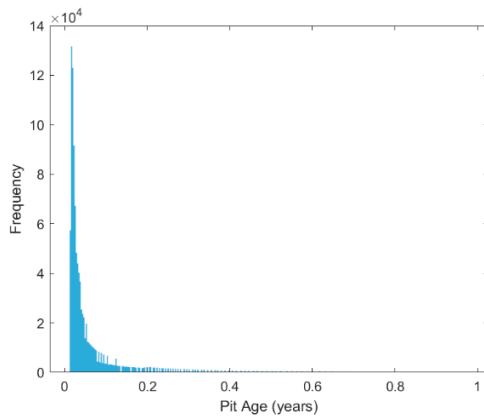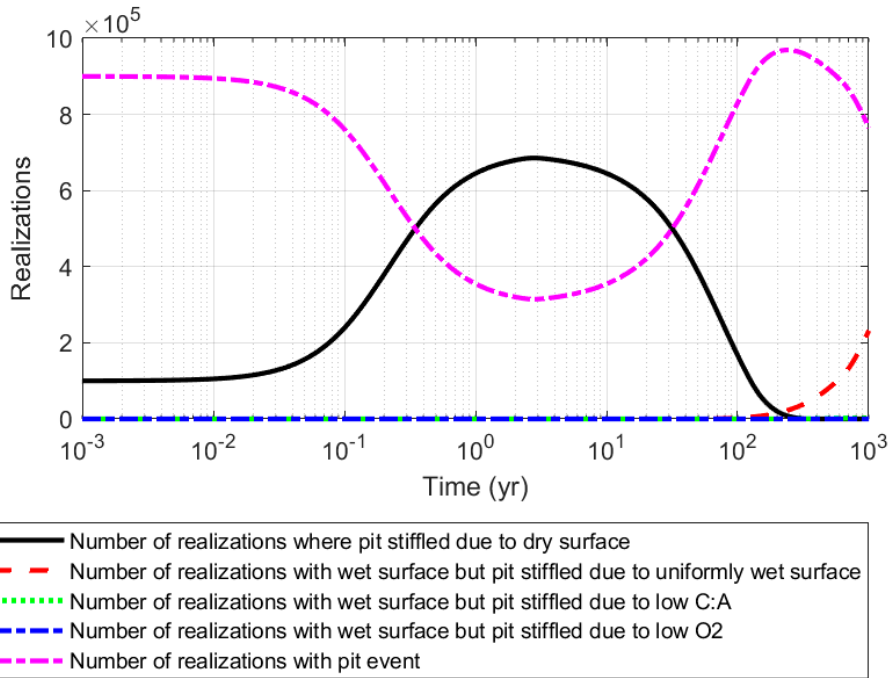

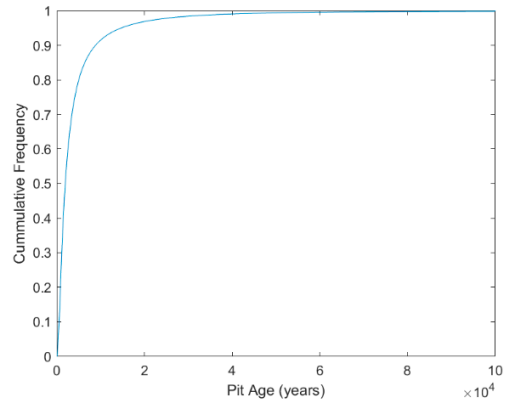(b) Distribution of pit ages.
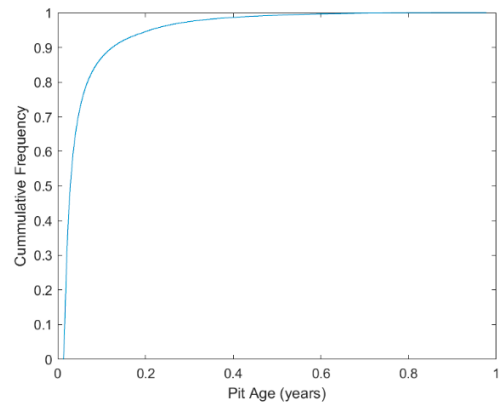
(c) Cumulative distribution of pit ages.
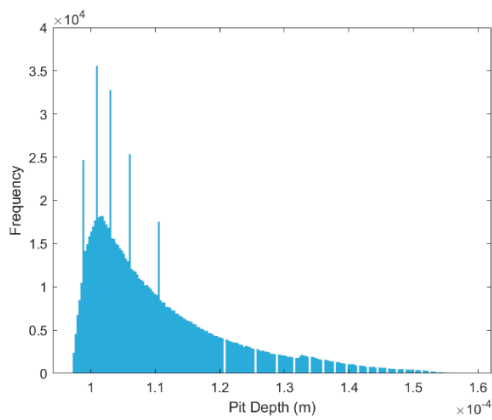
(d) Distribution of pits depths (linear scale).
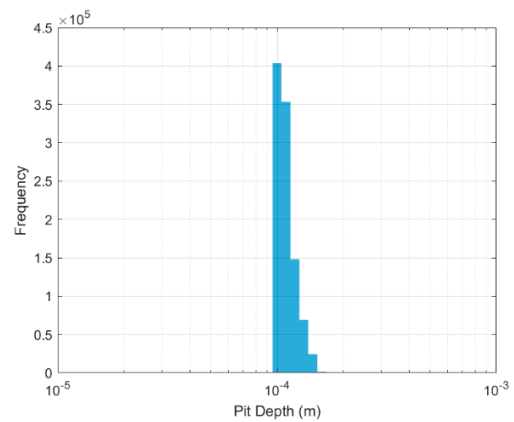
(e) Distribution of pits depths (logarithmic scale).

A2.5 O₂ threshold 0.01–0.1 % of initial concentration
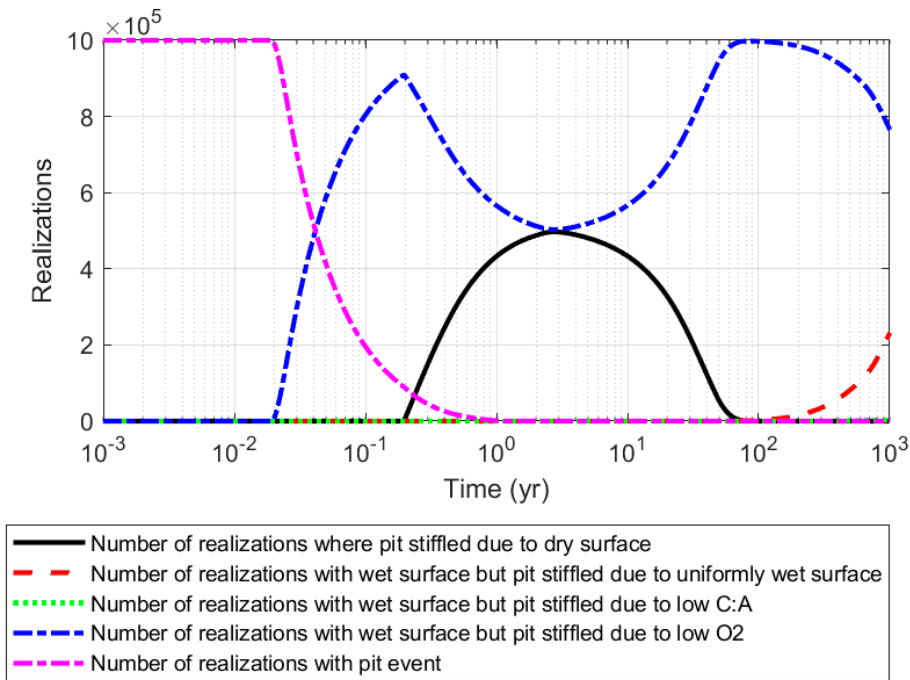
(a) Time dependence of the various stifling mechanisms.
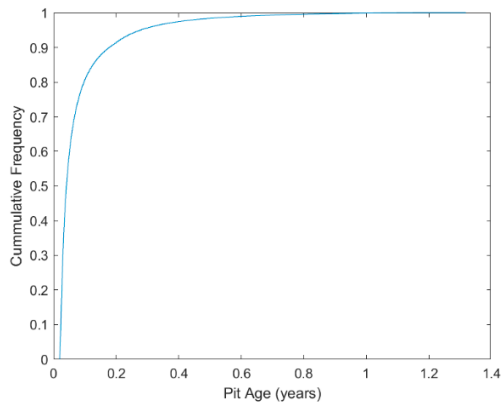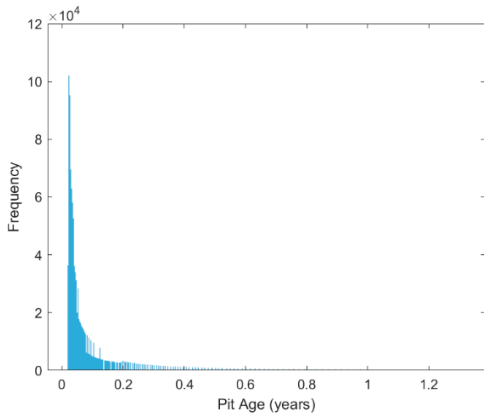
(b) Distribution of pit ages.
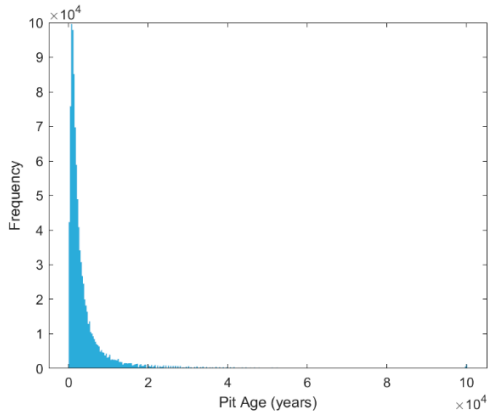

(c) Cumulative distribution of pit ages.
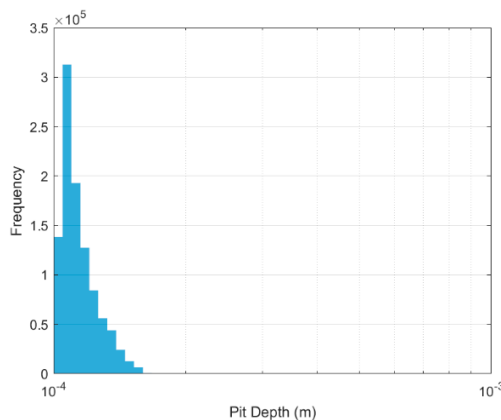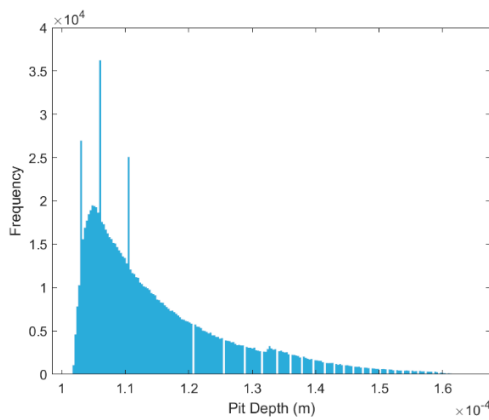
(d) Distribution of pits depths (linear scale).

(e) Distribution of pits depths (logarithmic scale).
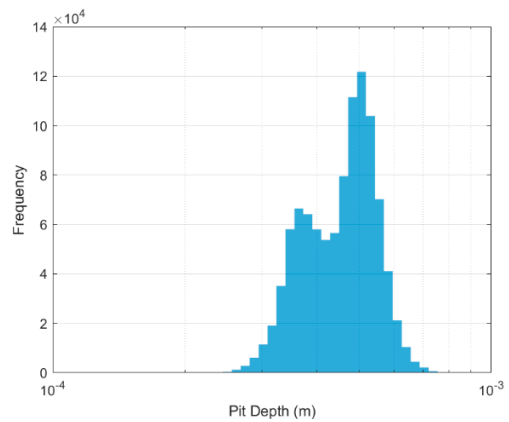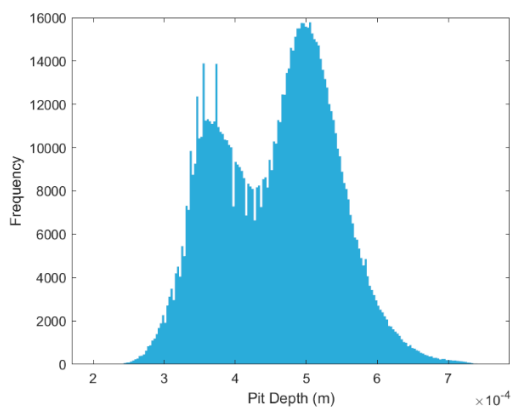
A2.6 O₂ threshold 0 %
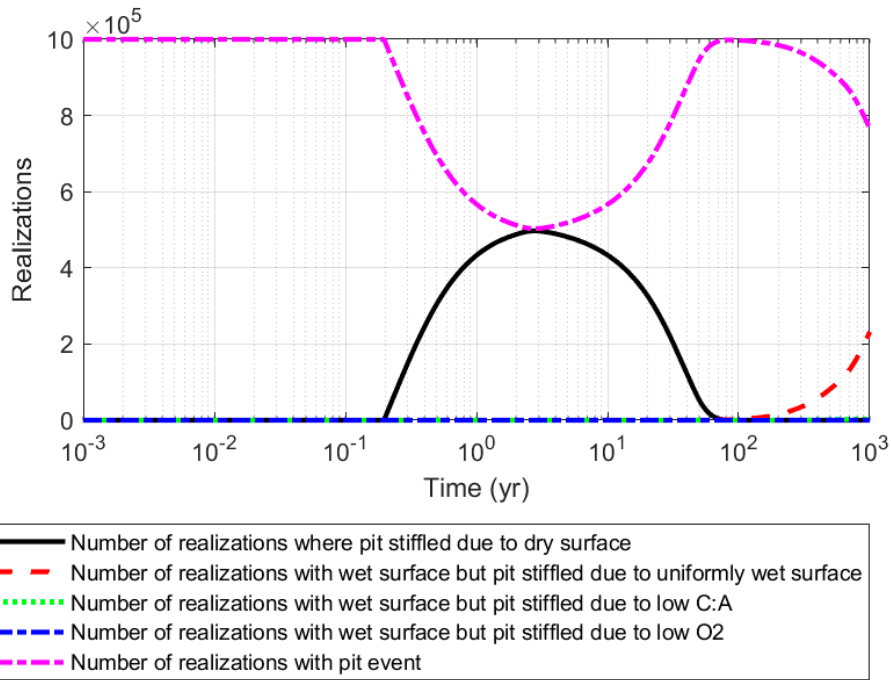
(a) Time dependence of the various stifling mechanisms.
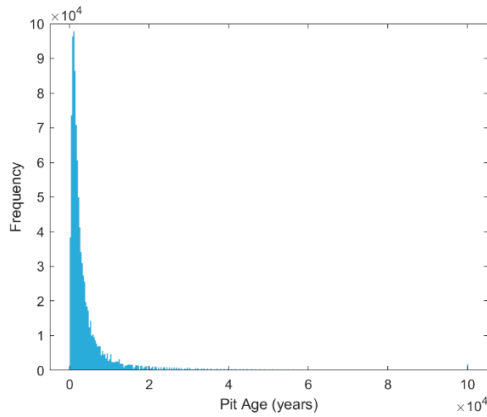
(b) Distribution of pit ages.
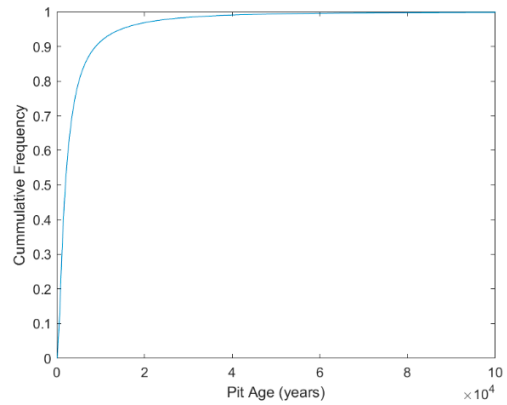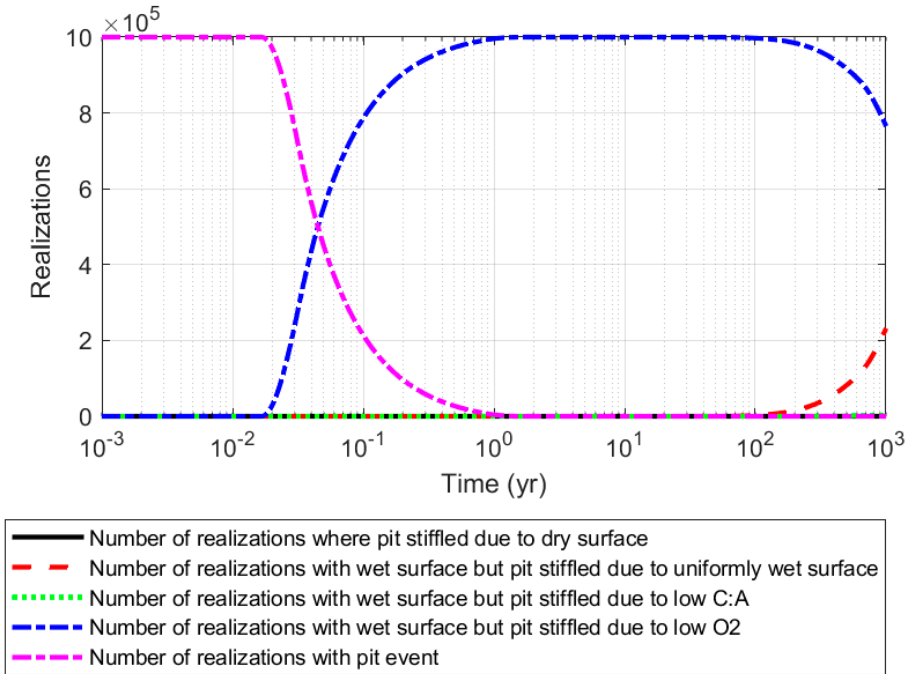

(c) Cumulative distribution of pit ages.
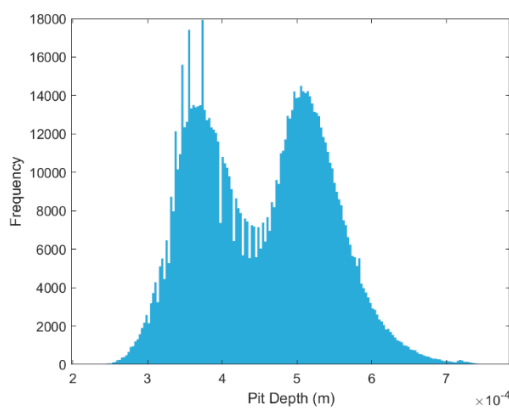
(d) Distribution of pits depths (linear scale).
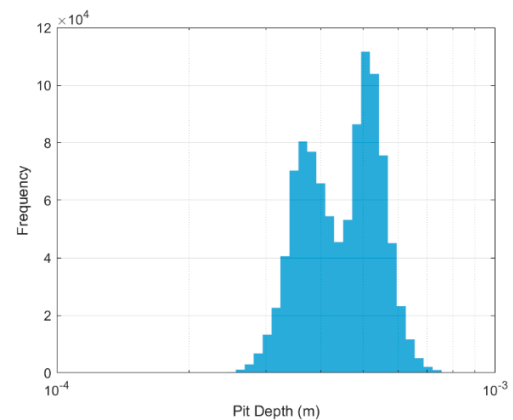
(e) Distribution of pits depths (logarithmic scale).

A3　O₂ consumption time 5 weeks – 5 years, DRH 55–75 % RH

The summary of the results is given in Table 4-4.

A3.1　O₂ threshold 10–30 % of initial concentration
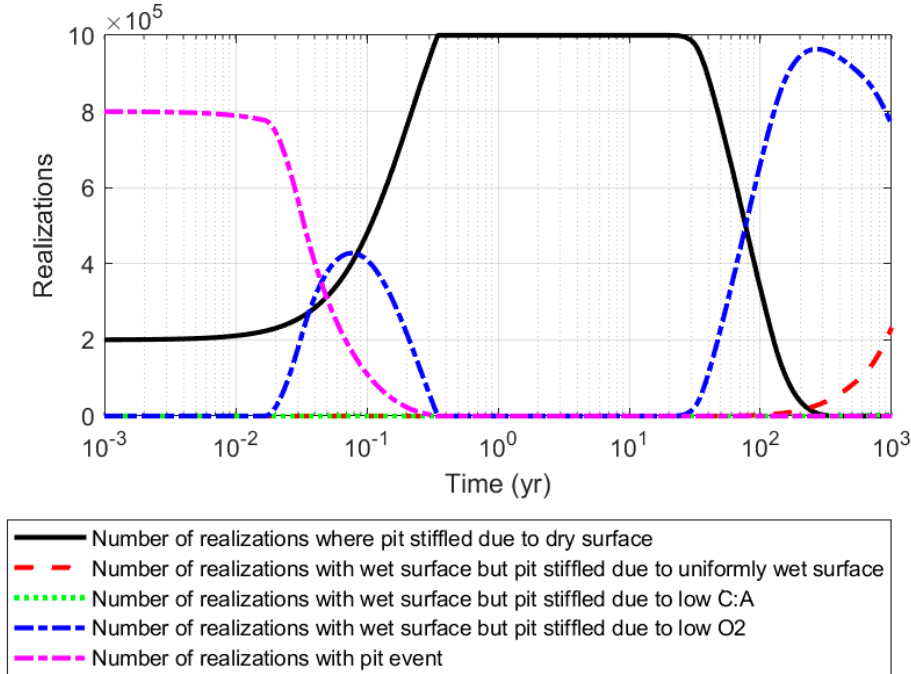
(a) Time dependence of the various stifling mechanisms.
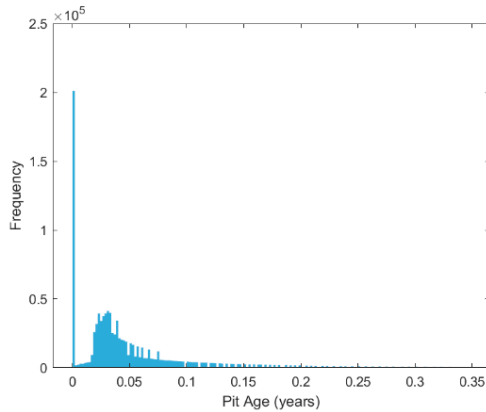
(b) Distribution of pit ages.
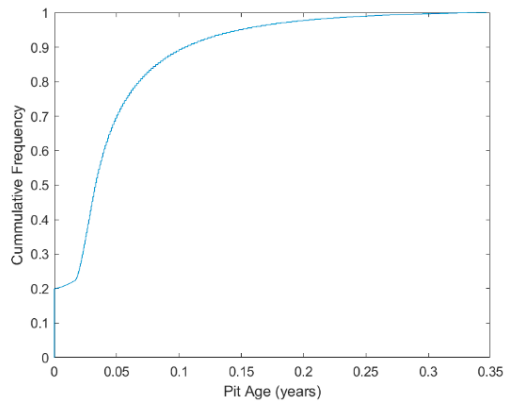
(c) Cumulative distribution of pit ages.
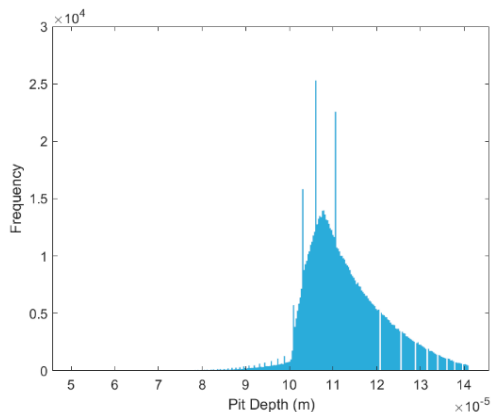
(d) Distribution of pits depths (linear scale).
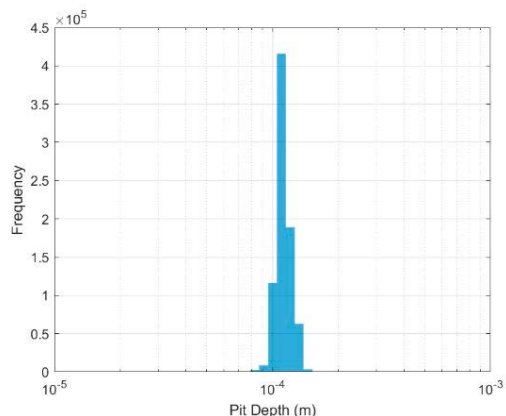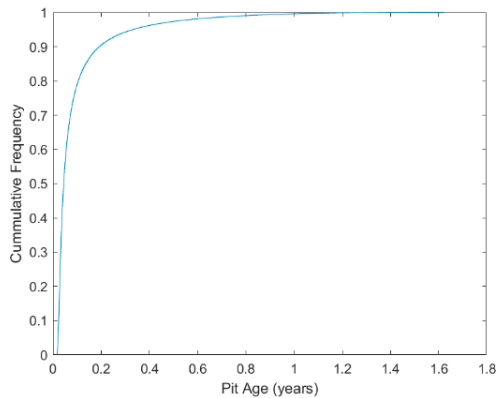
(e) Distribution of pits depths (logarithmic scale).

A3.2   O$_2$ threshold 5–20 % of initial concentration
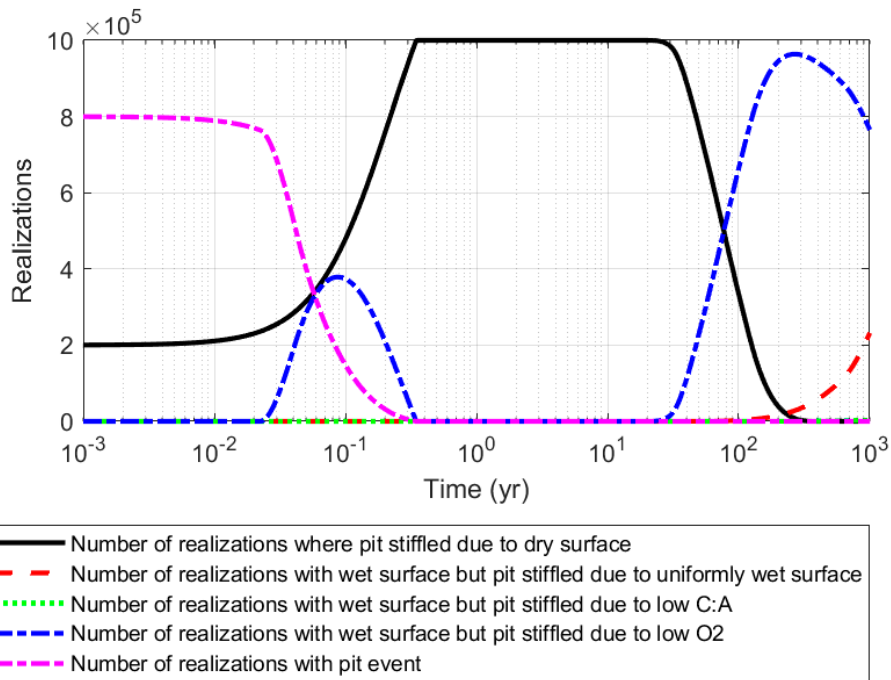
(a) Time dependence of the various stifling mechanisms.
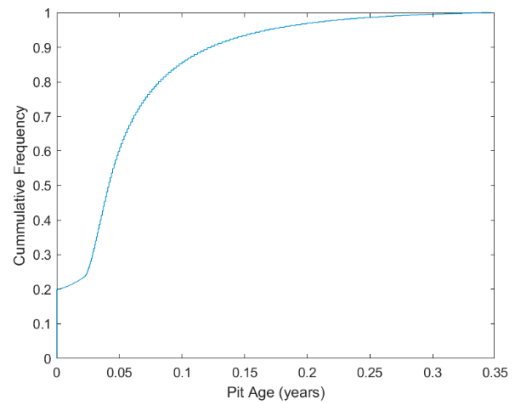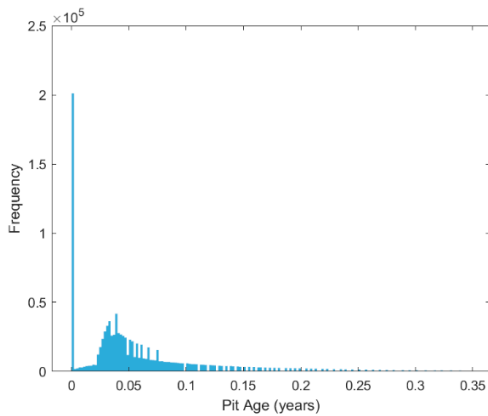
(b) Distribution of pit ages.

(c) Cumulative distribution of pit ages.
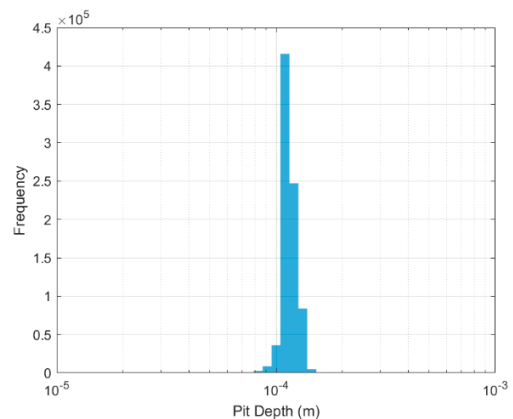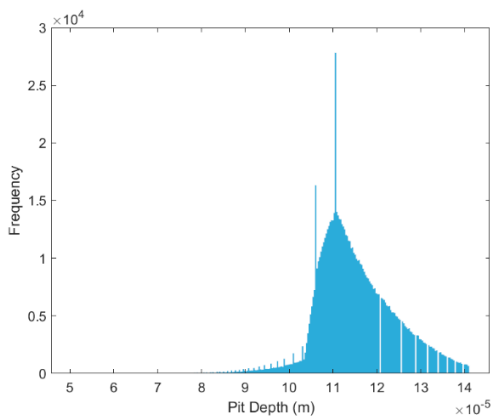
(d) Distribution of pits depths (linear scale).

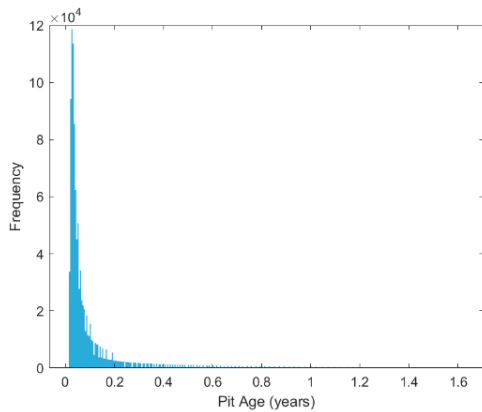(e) Distribution of pits depths (logarithmic scale).

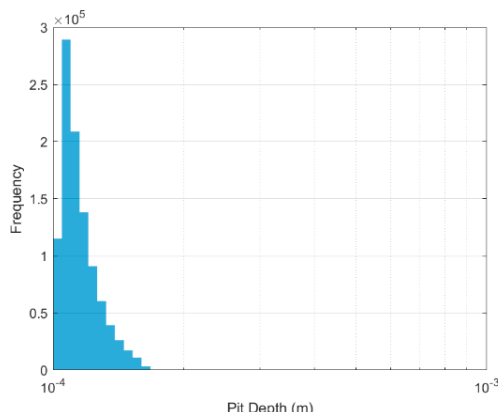## A3.3 O₂ threshold 1–10 % of initial concentration
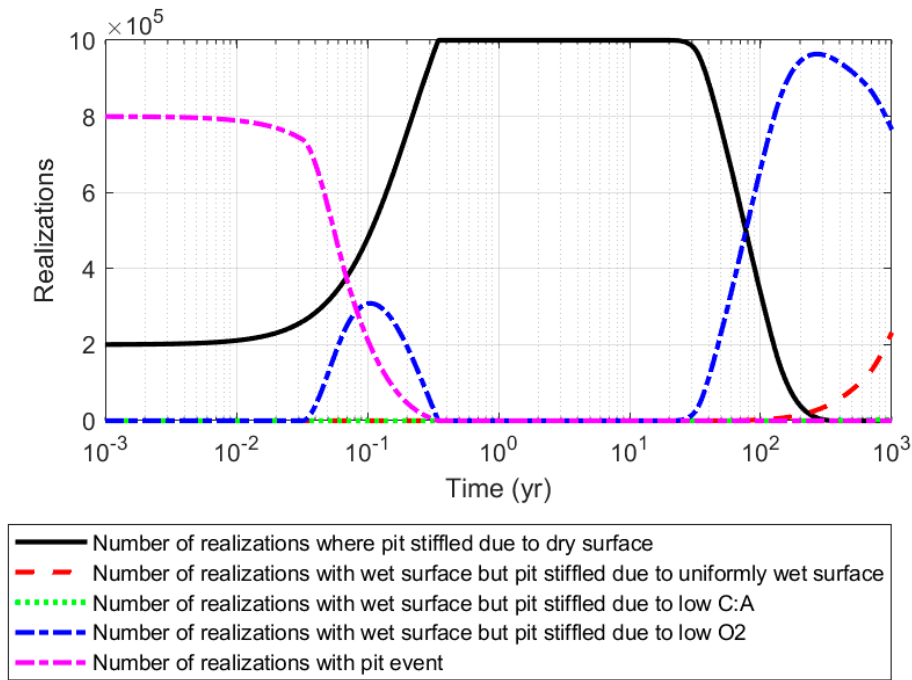
(a) Time dependence of the various stifling mechanisms.
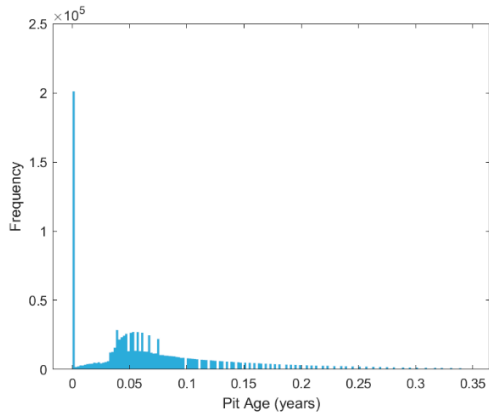
(b) Distribution of pit ages.
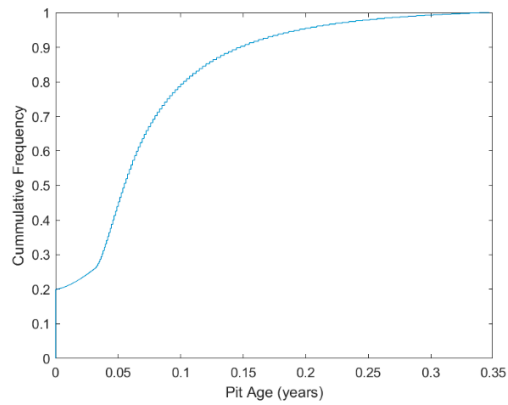
(c) Cumulative distribution of pit ages.
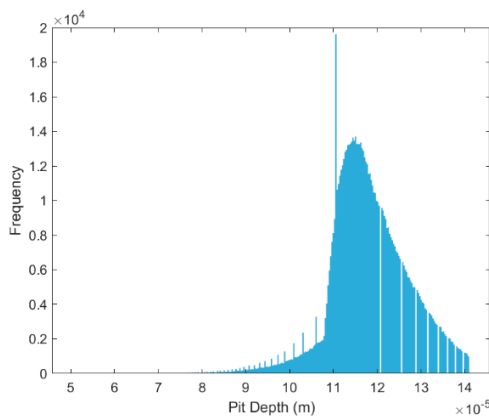
(d) Distribution of pits depths (linear scale).
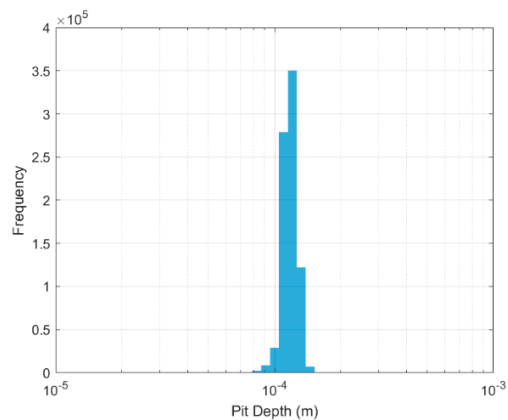
(e) Distribution of pits depths (logarithmic scale).

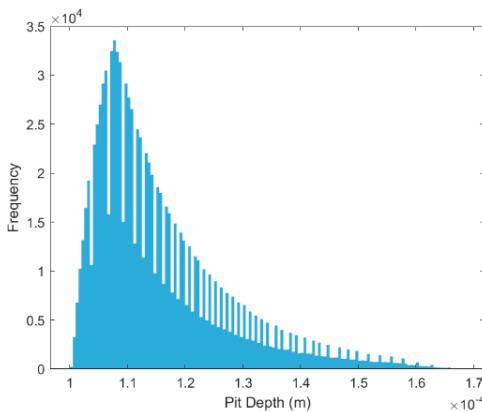## A3.4   O₂ threshold 0.1–1 % of initial concentration
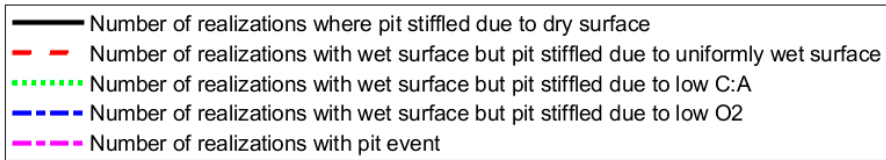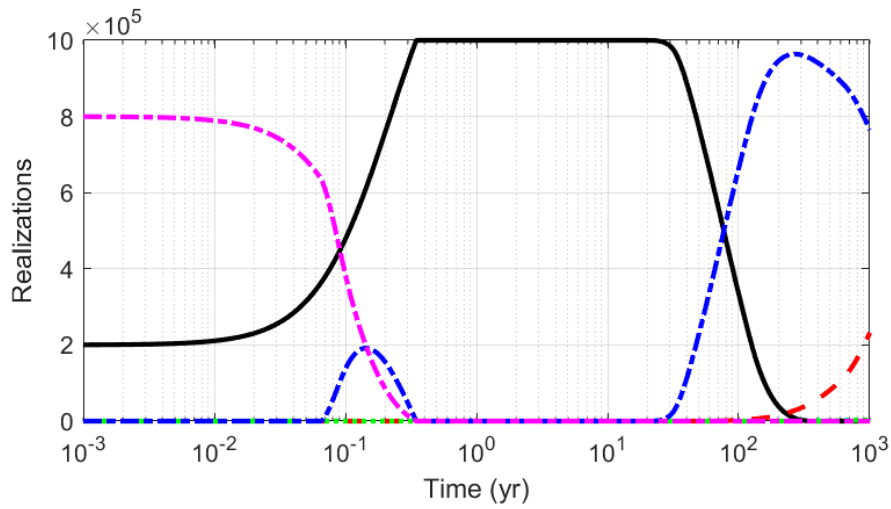
(a) Time dependence of the various stifling mechanisms.
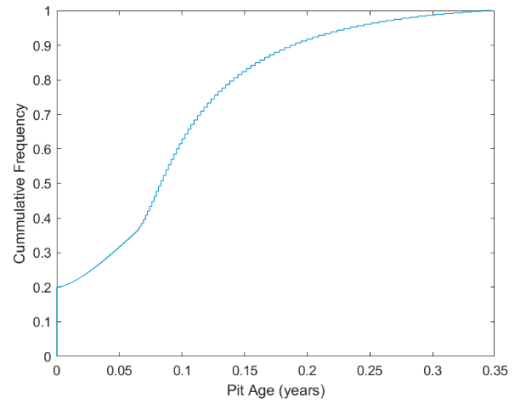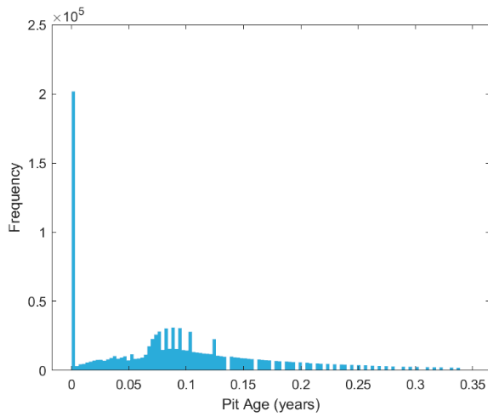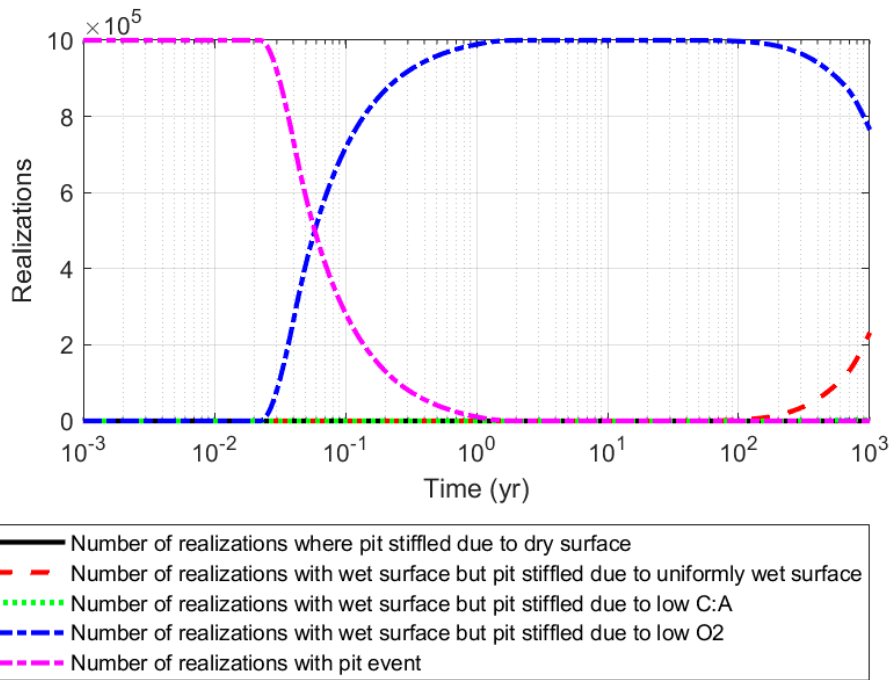

(b) Distribution of pit ages.
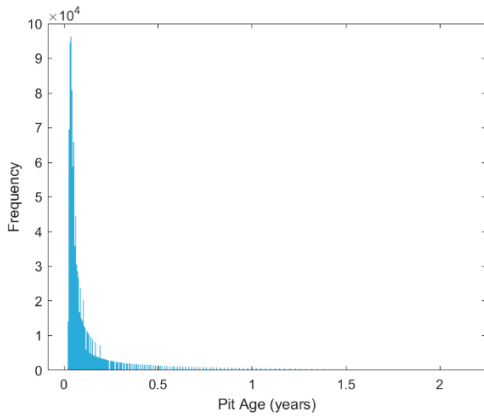

(c) Cumulative distribution of pit ages.
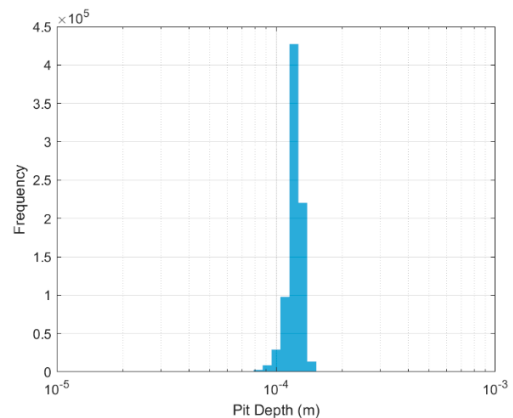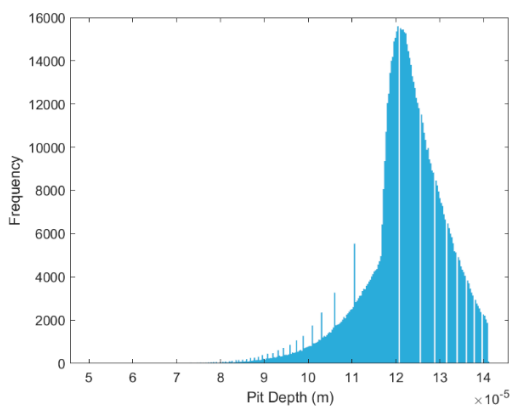
(d) Distribution of pits depths (linear scale).

(e) Distribution of pits depths (logarithmic scale).

A3.5 O₂ threshold 0.01–0.1 % of initial concentration
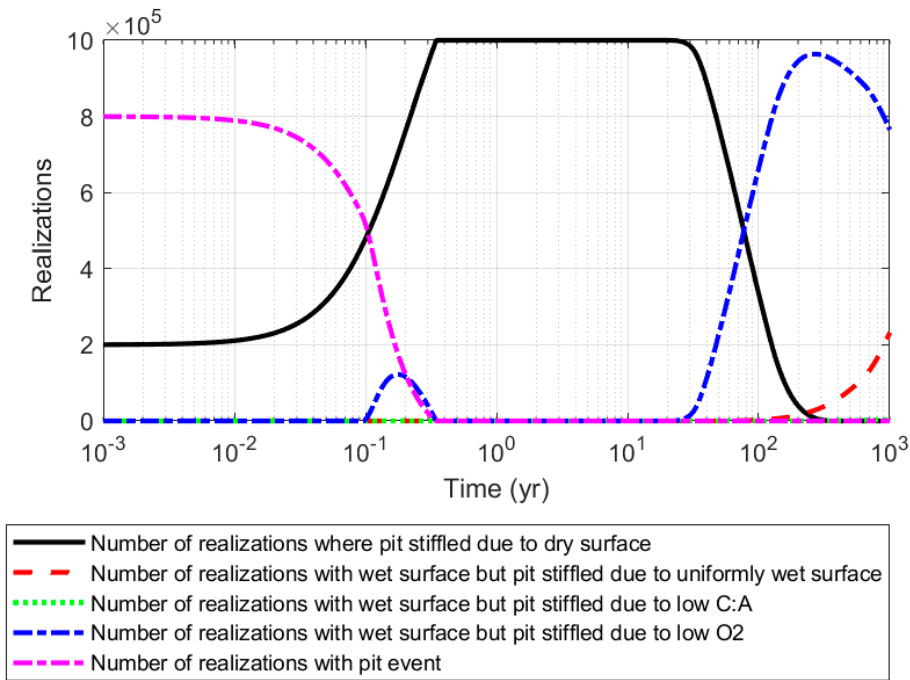
(a) Time dependence of the various stifling mechanisms.
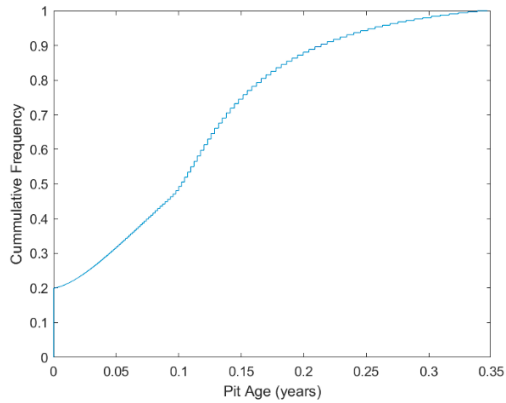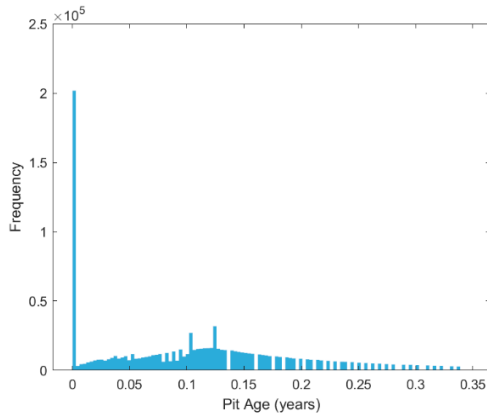
(b) Distribution of pit ages.

(c) Cumulative distribution of pit ages.

(d) Distribution of pits depths (linear scale).

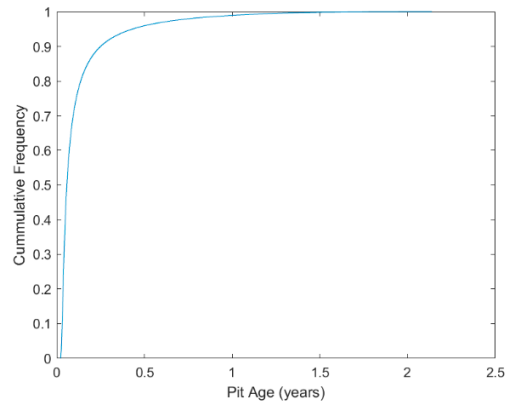(e) Distribution of pits depths (logarithmic scale).
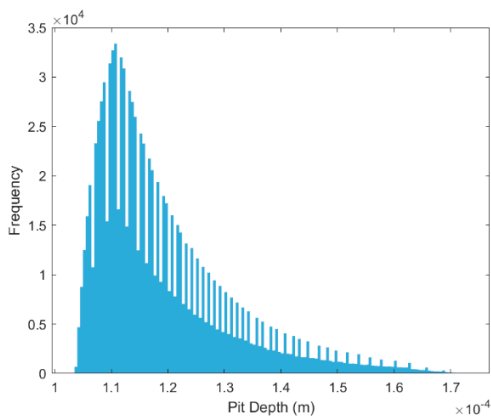
A3.6   O₂ threshold 0 %
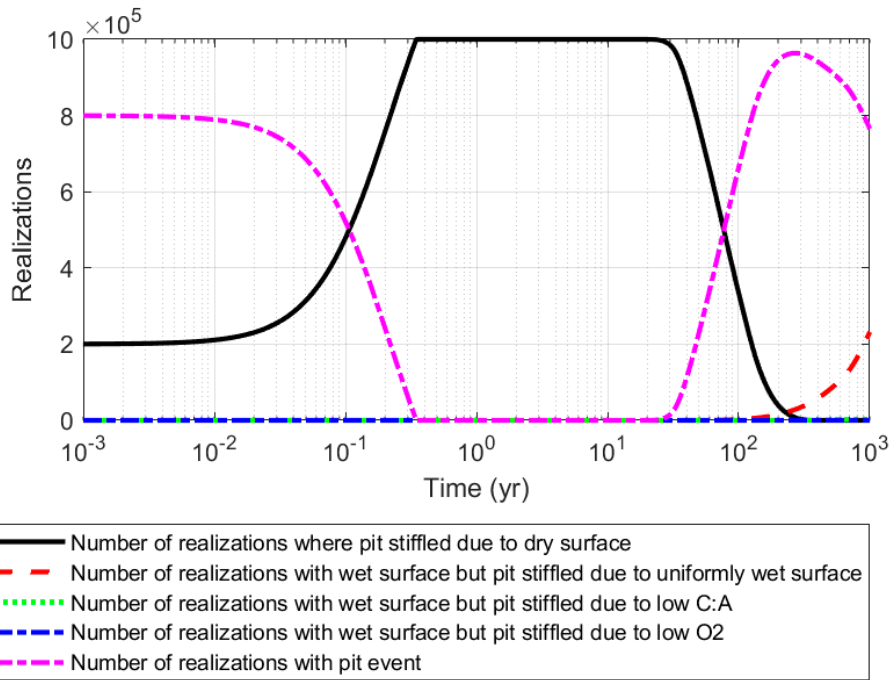
(a) Time dependence of the various stifling mechanisms.
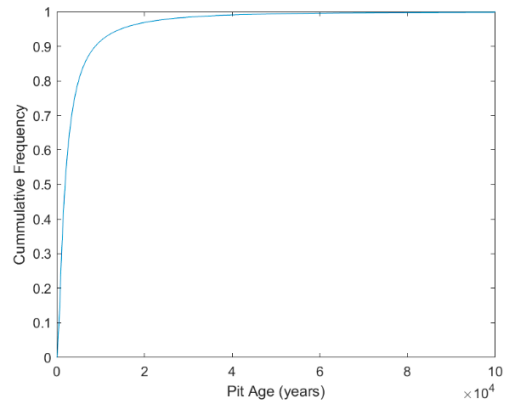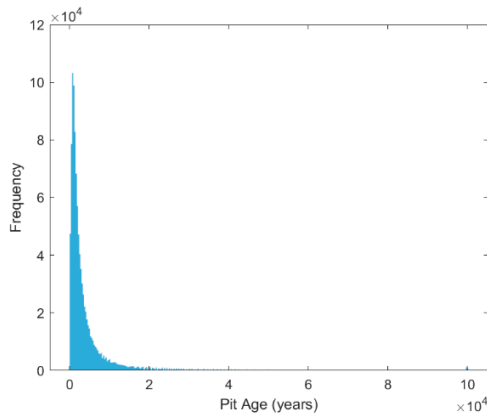
(b) Distribution of pit ages.

(c) Cumulative distribution of pit ages.
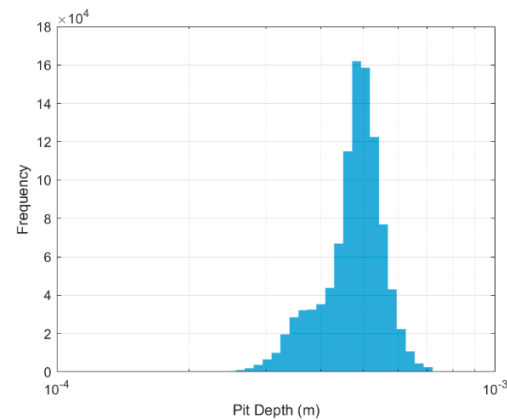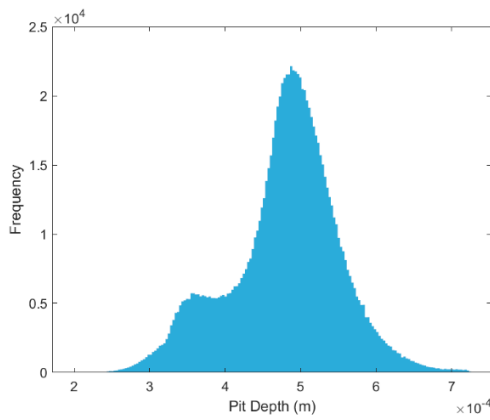
(d) Distribution of pits depths (linear scale).

(e) Distribution of pits depths (logarithmic scale).

A4 O₂ consumption time 5 weeks – 5 years, DRH 35–75 % RH

The summary of the results is given in Table 4-5.

A4.1 O₂ threshold 10–30 % of initial concentration
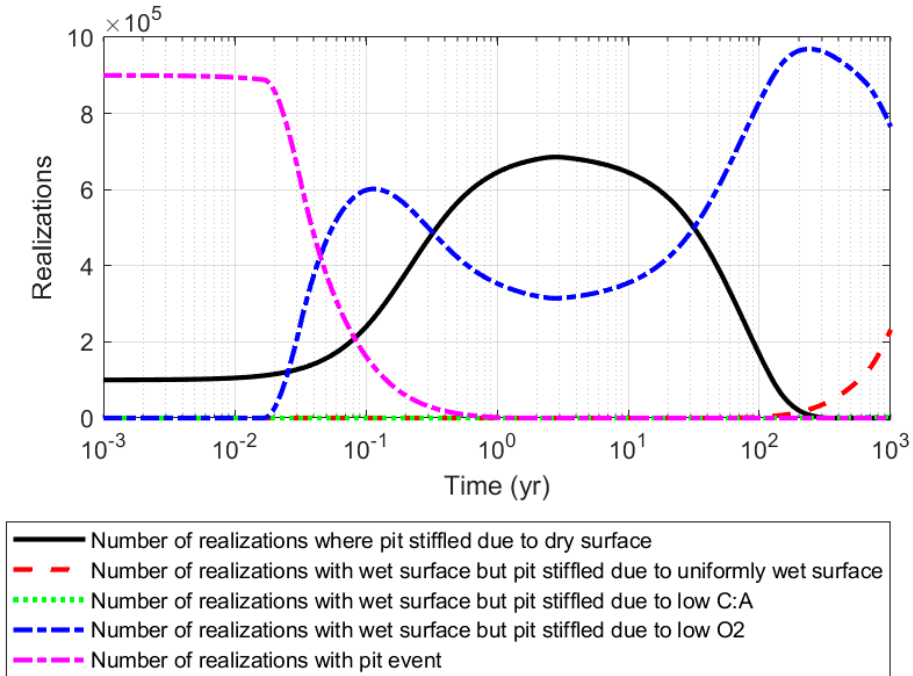
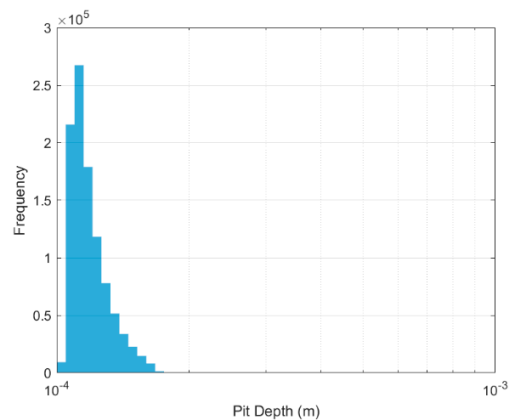(a) Time dependence of the various stifling mechanisms.
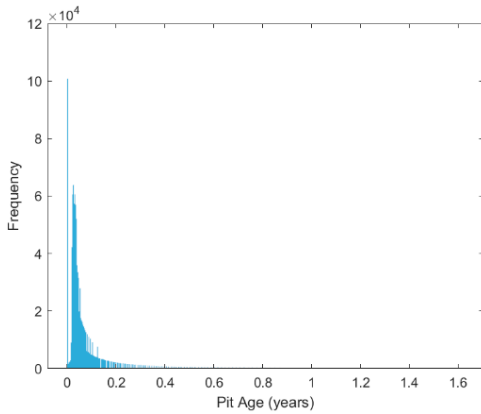
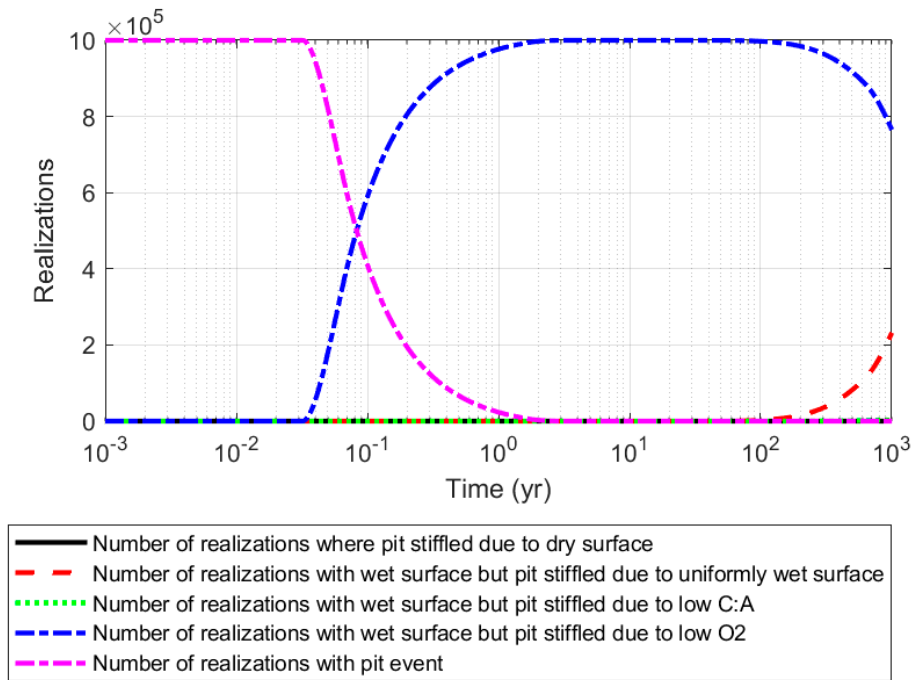(b) Distribution of pit ages.

(c) Cumulative distribution of pit ages.

(d) Distribution of pits depths (linear scale).

(e) Distribution of pits depths (logarithmic scale).

A4.2   O₂ threshold 5–20 % of initial concentration

(a) Time dependence of the various stifling mechanisms.

(b) Distribution of pit ages.

(c) Cumulative distribution of pit ages.
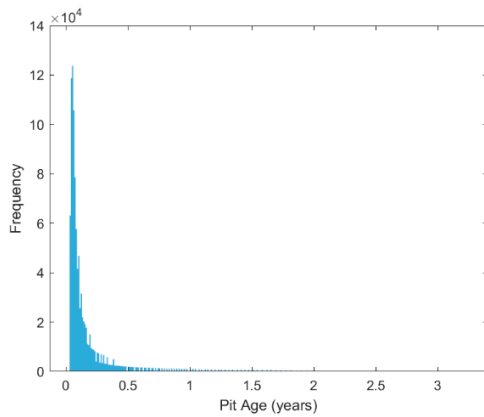

(d) Distribution of pits depths (linear scale).

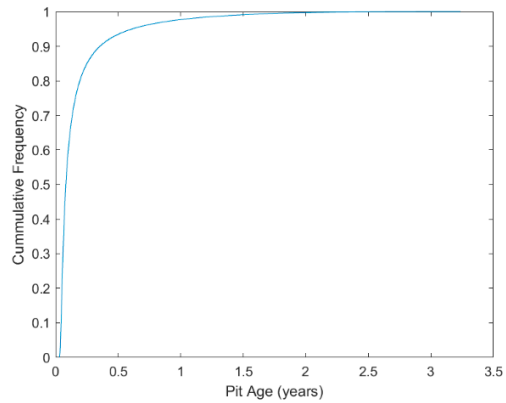(e) Distribution of pits depths (logarithmic scale).

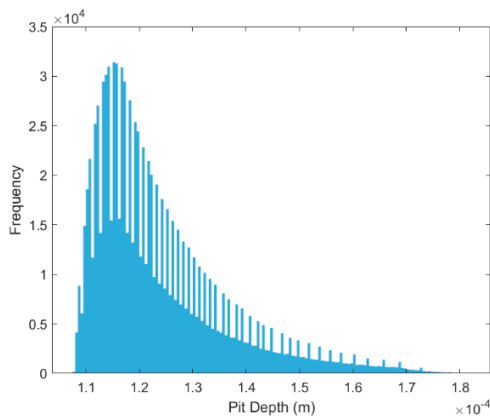## A4.3   O₂ threshold 1–10 % of initial concentration

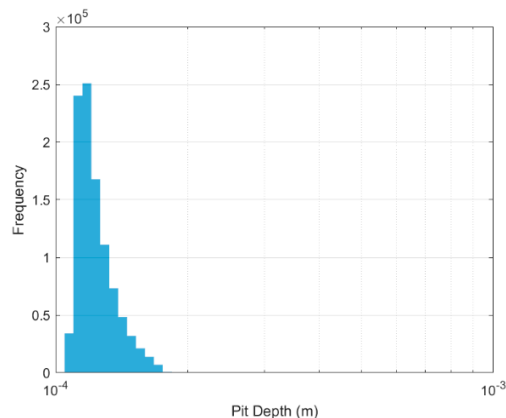(a) Time dependence of the various stifling mechanisms.

(b) Distribution of pit ages.

(c) Cumulative distribution of pit ages.

(d) Distribution of pits depths (linear scale).

(e) Distribution of pits depths (logarithmic scale).

A4.4　O₂ threshold 0.1–1 % of initial concentration

(a) Time dependence of the various stifling mechanisms.

(b) Distribution of pit ages.
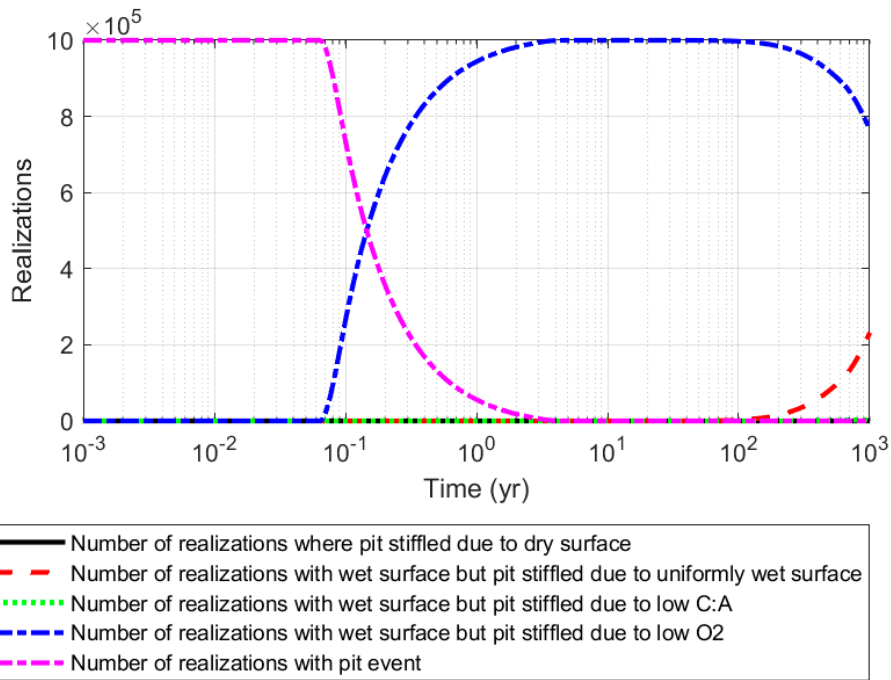

(c) Cumulative distribution of pit ages.

(d) Distribution of pits depths (linear scale).

(e) Distribution of pits depths (logarithmic scale).

A4.5   O₂ threshold 0.01–0.1 % of initial concentration

(a) Time dependence of the various stifling mechanisms.

(b) Distribution of pit ages.

(c) Cumulative distribution of pit ages.

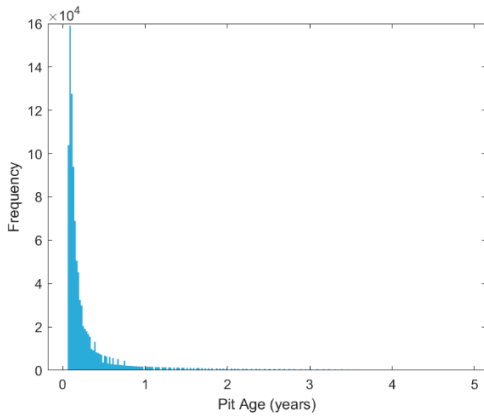(d) Distribution of pits depths (linear scale).

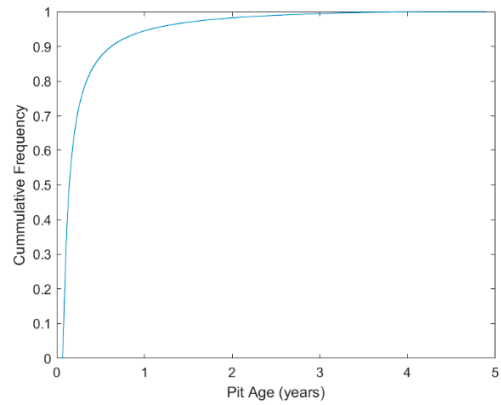(e) Distribution of pits depths (logarithmic scale).
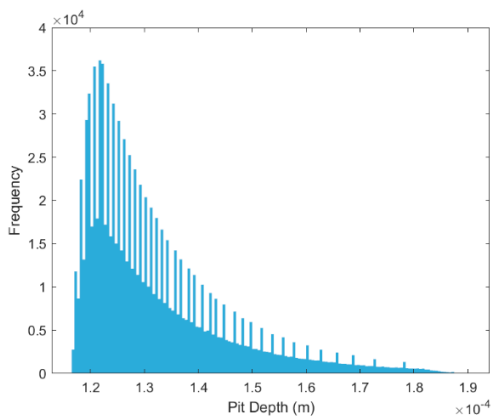
A4.6 O₂ threshold 0 %

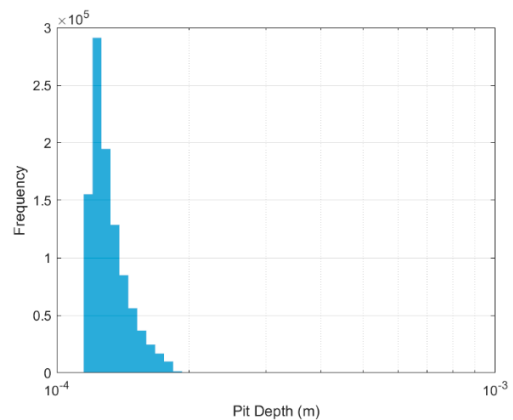(a) Time dependence of the various stifling mechanisms.

(b) Distribution of pit ages.

(c) Cumulative distribution of pit ages.

(d) Distribution of pits depths (linear scale).

(e) Distribution of pits depths (logarithmic scale).

A5   O$_2$ consumption time 5 weeks – 5 years, DRH 35 % RH

The summary of the results is given in Table 4-6.

A5.1   O$_2$ threshold 10–30 % of initial concentration

(a) Time dependence of the various stifling mechanisms.

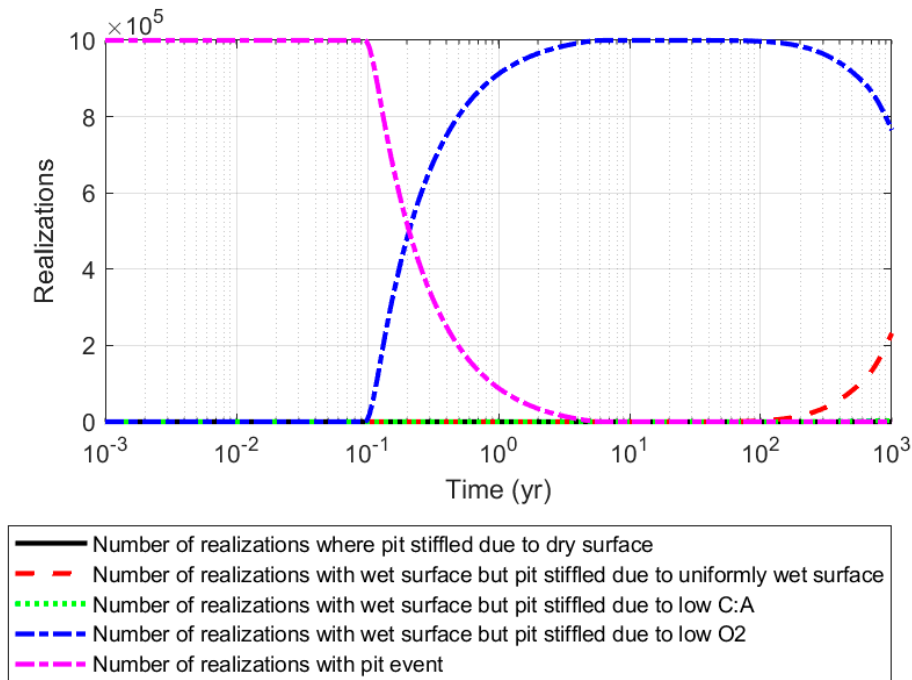(b) Distribution of pit ages.

(c) Cumulative distribution of pit ages.

(d) Distribution of pits depths (linear scale).

(e) Distribution of pits depths (logarithmic scale).

A5.2   O₂ threshold 5–20 % of initial concentration

(a) Time dependence of the various stifling mechanisms.

(b) Distribution of pit ages.

(c) Cumulative distribution of pit ages.

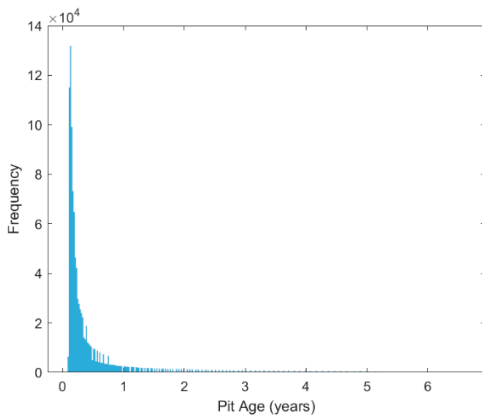(d) Distribution of pits depths (linear scale).

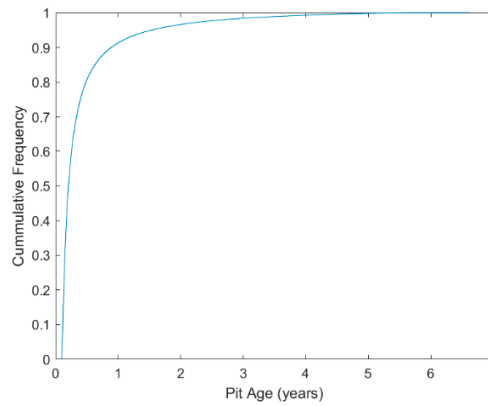(e) Distribution of pits depths (logarithmic scale).

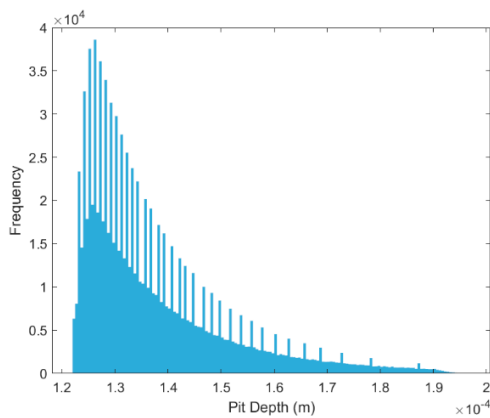## A5.3 O₂ threshold 1–10 % of initial concentration

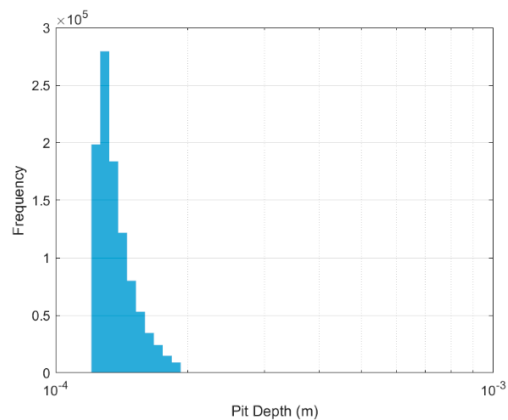(a) Time dependence of the various stifling mechanisms.

(b) Distribution of pit ages.

(c) Cumulative distribution of pit ages.

(d) Distribution of pits depths (linear scale).

(e) Distribution of pits depths (logarithmic scale).

A5.4   O₂ threshold 0.1–1 % of initial concentration

(a) Time dependence of the various stifling mechanisms.

(b) Distribution of pit ages.
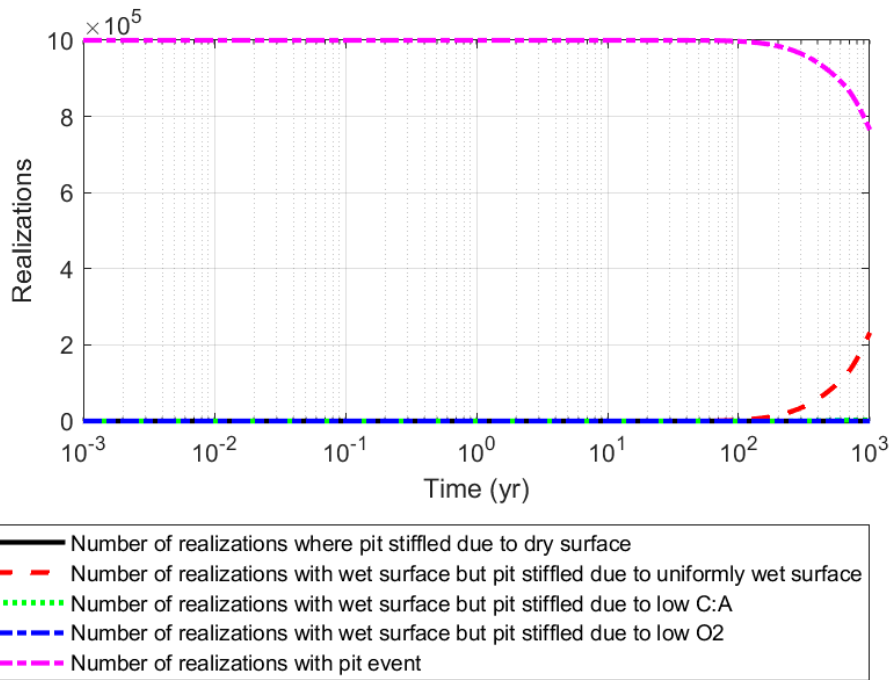
(c) Cumulative distribution of pit ages.

(d) Distribution of pits depths (linear scale).

(e) Distribution of pits depths (logarithmic scale).

A5.5   O$_2$ threshold 0.01–0.1 % of initial concentration

(a) Time dependence of the various stifling mechanisms.

(b) Distribution of pit ages.

(c) Cumulative distribution of pit ages.

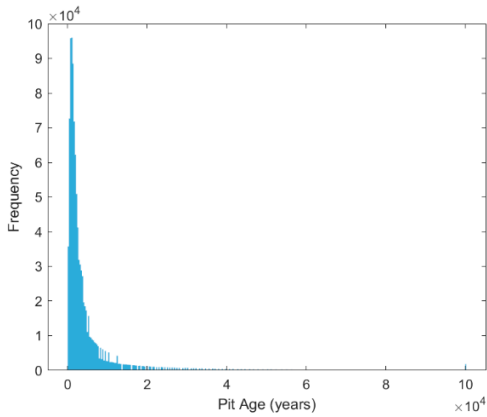(d) Distribution of pits depths (linear scale).

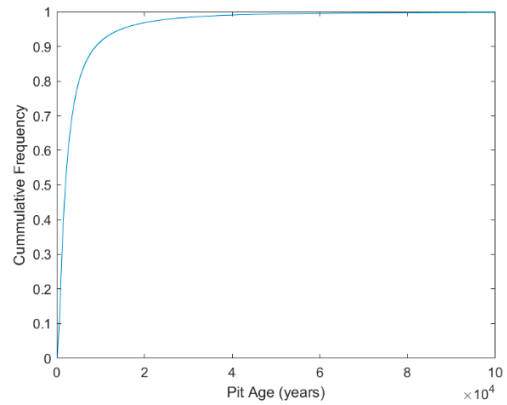(e) Distribution of pits depths (logarithmic scale).
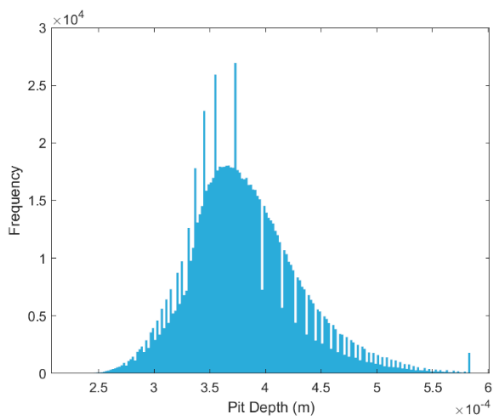
A5.6   O₂ threshold 0 %

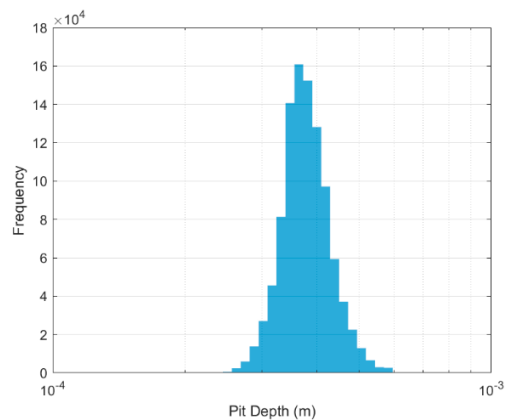(a) Time dependence of the various stifling mechanisms.

(b) Distribution of pit ages.

(c) Cumulative distribution of pit ages.

(d) Distribution of pits depths (linear scale).

(e) Distribution of pits depths (logarithmic scale).

SKB is responsible for managing spent nuclear fuel and radioactive waste produced by the Swedish nuclear power plants such that man and the environment are protected in the near and distant future.

skb.se